Thermoelectric Properties of Low-Dimensional Structures at Low Temperatures

by

Kejia Zhang

A dissertation submitted in partial fulfillment
Of the requirements for the degree of
Doctor of Philosophy
(Mechanical Engineering)
In the University of Michigan
2016

Doctoral Committee:

Associate Professor Kevin P. Pipe, Chair
Professor Katsuo Kurabayashi
Assistant Professor Xiaogan Liang
Professor Ctirad Uher

Table of Contents

List of Figures

List of Tables

Abstract

Thermoelectric energy conversion has a wide range of potential applications but is currently inhibited by low efficiency (as governed in thermoelectric materials by the figure-of-merit *ZT*). Low-dimensional structures such as superlattices (SLs) and nanowires may offer a new approach to achieve high *ZT*, particularly at low temperatures where current thermoelectric materials are not as efficient. In this work, the thermal and thermoelectric properties of HgCdTe (MCT) SLs and doped/coated single-walled carbon nanotube (SWCNT) systems have been designed and measured near and below room temperature.

A modified 3ω method was used to measure both the thermal coductivity and Seebeck coefficient in the cross-plane direction for the SLs. The cross-plane electrical conductivity was determined through a modified transmission line method. The thermal conductivity of long-period SLs was found to be lower than the alloy value, especially at cyrogenic temperatures, and approximately constant over a wide range of temperatures.

A comparative method was used to measure the thermal conductivity, electrical conductivity, and Seebeck coefficient of ultralow density SWCNT networks that were either pristine or coated by graphite, BN, or PEDOT:PSS. The thermal and electrical impedances were found to be dominated by intertube junctions in pristine networks and by tubes in coated networks. The thermal and electrical conductivities were found to be lower in coated networks even though they have higher densities due to strong

scattering introduced by coatings.

The effects of doping on SWCNT thermal conductivity were studied using molecular dynamics simulations. Phonon dispersion curves and phonon lifetimes were further calculated to examine scattering mechanisms. Substitutional and pyridine-like nitrogen doping was found to reduce thermal conductivity effectively even at low dopant concentrations. Since substitutional nitrogen doping has been shown to increase electrical conductivity in SWCNTs, it provides an interesting alternative to coating in improving *ZT* in such systems.

Chapter 1

Thesis Overview and Thermoelectric Background

The world currently faces numerous challenges relating to energy supply and consumption. Thermoelectric (TE) devices deliver electricity to a load using heat as a power source or provide refrigeration in the presence of an electrical current. In the mid-to-high temperature range (near or above room temperature), high efficiency TE materials are an important material system for power generation devices that harvest the waste heat expelled from power plants and vehicles and turn it into electrical energy. [1] TE generators can be easily scaled to satisfy the power requirements of increasingly miniaturized sensors and modules; a recent implantable medical sensor was powered by the difference in temperature between the skin surface and the core body. [2] In the mid-to-low temperature range (near or below room temperature), TE coolers (also called Peltier coolers), which have no moving parts, are important components for laser sources, switching/routing elements, detectors, and sensors because they produce less pollution and noise [3] [4] [5]. Keeping up with Moore's law, semiconductor packing densities have increased so much that the dissipation of heat has become a major challenge, and there is a need for micro cooling with higher cooling densities. The conversion efficiency of TE materials is evaluated by a figure of merit (*ZT*, introduced in Chap. 1.1). In [6] the timeline of *ZT* in important TE materials as a function of temperature is plotted (Fig. 1.1). As can be seen, currently TE materials with decent *ZT* mainly work near and above room temperature. The need

for developing high performance TE materials for Peltier cooling at mid−to−low temperature is urgent. Good TE material candidates which can be modified to both *p*-type and *n*-type are also highly needed to implement both *p*- and *n*- legs in device modules.

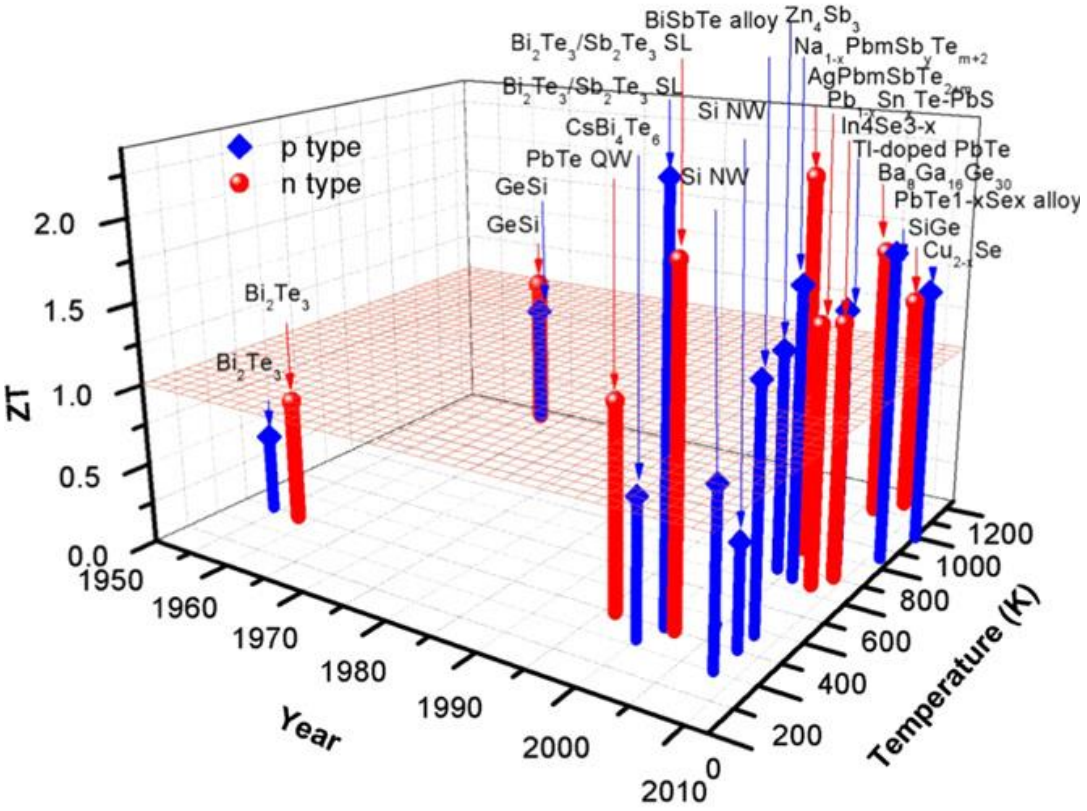

Figure 1.1 *ZT* as a function of temperature and year revealing the important development of TE materials. Reproduced from [6].

1.0 Basic Concepts

This section introduces some basic concepts of thermoelectric theory. A detailed description appears in [7].

Seebeck effect: When two electrical conductors are brought together and the junction between them is heated up, a voltage is induced on the ends of the open circuit. The Seebeck coefficient (*S*) is defined as the ratio between the induced voltage (ΔV) and the temperature difference (ΔT):

$$S = \frac{\Delta V}{\Delta T} \tag{1.0.1}$$

Peltier effect: When an electrical current flows through a thermocouple, a small heating or cooling is produced depending of the direction of the current. The Peltier coefficient (π) is defined as the ratio between the heating/cooling rate at each junction (q) and the current (I) that passes through it:

$$\pi = \frac{q}{I} \tag{1.0.2}$$

Thomson effect: This effect describes the reversible heating or cooling (q) present when there is an electrical current (I) flowing in addition to a gradient of temperature (ΔT), $q = \beta I \Delta T$, where β is the Thomson coefficient.

Thermoelectric generator: Consider a pair of semiconductor legs (*p*-type and *n*-type materials) connected electrically in series and thermally in parallel. If one side of the pair of legs is heated and the other side is kept at a reference temperature, the ΔT between the two legs produces excess carriers which may diffuse from the hot to the cold side. The diffusion determines the Seebeck voltage that delivers a current I when the circuit is connected to a load as shown in Fig. 1.2 (a).

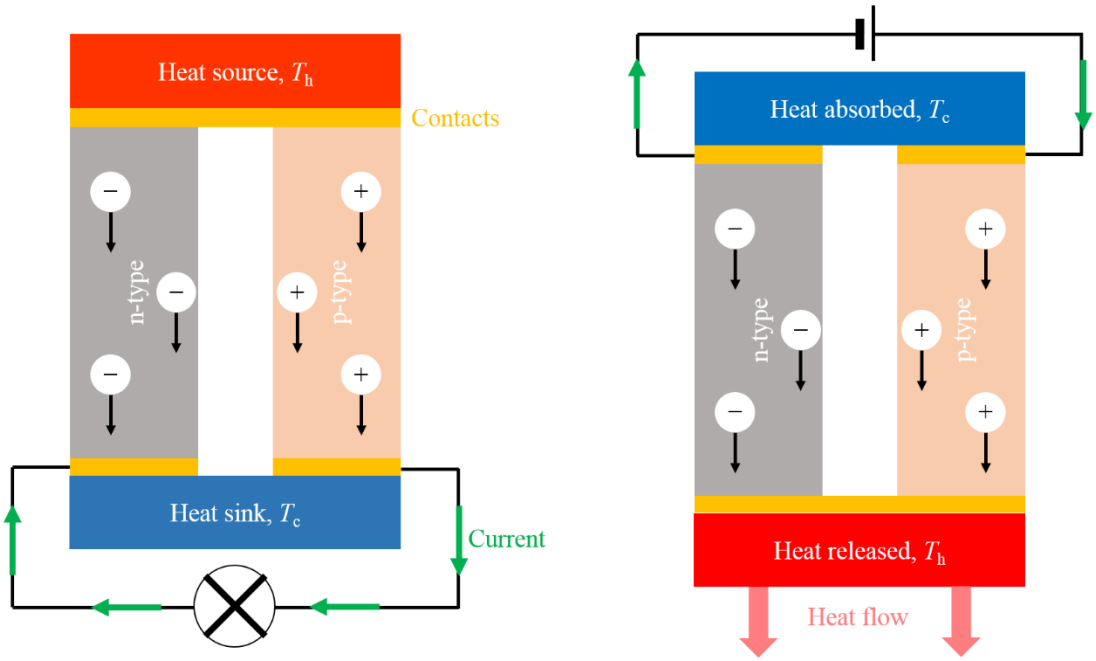

(a) (b)

Figure 1.2 Schematic diagram of a single TE element formed by a pair of legs connected electrically in series and thermally in parallel. T_h represents temperature at the hot end and T_c represents temperature at the cold end. (a) Thermoelectric power generation. (b) Thermoelectric cooling.

The efficiency η of the device is given by the ratio of the output power (W) to the rate of the heat (Q) that is drawn from the source: $\eta = W/Q$. The current flowing through the circuit is given by

$$I = \frac{\left(S_p - S_n\right)\left(T_h - T_c\right)}{R_L + R_p + R_n}, \tag{1.0.3}$$

where R is the electrical resistance, subscripts p, n, and L represent semiconductor materials composing the p-type leg, n-type leg, and the load, respectively, and T_h and T_c are the temperatures of the heat source (hot end) and heat sink (cold end). The power delivered to the load resistor is given by I^2R_L.The heat that is drawn from the source is given by

$$Q = \left(S_p - S_n\right) I T_h + \left(k_p + k_n\right)\left(T_h - T_c\right), \tag{1.0.4}$$

where k_p and k_n are the thermal conductivities of the two legs. The efficiency reaches

its maximum when

$$\frac{R_L}{R_n + R_p} = \sqrt{1+ZT} \quad \& \quad ZT = \frac{S^2\sigma}{k}T \tag{1.0.5}$$

where $\sigma = \sigma_n + \sigma_p$ is the total electrical conductivity, $S = S_p - S_n$ is the total Seebeck coefficient, $k = k_p + k_n$ is the total thermal conductivity of the material, and $T = ½(T_h + T_c)$ is the mean temperature. Using Eq. (1.0.3) to Eq. (1.0.5), the maximum efficiency is given by

$$\eta_{max} = \frac{T_h - T_c}{T_h}\frac{\sqrt{1+ZT}-1}{\sqrt{1+ZT}+\frac{T_c}{T_h}} \tag{1.0.6}$$

when ZT is much larger than 1, the efficiency approaches the Carnot efficiency given by $(T_h - T_c)/ T_h$. Therefore, ZT is known as the figure of merit that defines the efficiency of a TE material.

Thermoelectric cooler: In the pair arrangement similar to that of the TE power generator, when a current flows through the structure, a net cooling occurs at the cold end and a net heating at the hot end. Because their electrical conduction occurs through holes and electrons respectively, materials that are *p*-type and *n*-type have opposite directions of ΔT for the same direction of current flow, as shown in Fig. 1.2 (b).

The energy efficiency of TE cooler is measured by coefficient of performance (COP) of the device and is given by the ratio of the heat absorbed (Q) to the electrical power input (W) drawn from the source. The input power is given by

$$W = S\left(T_h - T_c\right)I + \left(R_p + R_n + R_L\right)I^2, \tag{1.0.7}$$

where the potential difference applied to the module is used in part to overcome the electrical resistance and to balance the Seebeck voltage resulting from the temperature

difference across the legs. The cooling capacity is given by

$$Q = ST_{\mathrm{c}}I - \tfrac{1}{2}\left(R_{\mathrm{p}} + R_{\mathrm{n}}\right)I^2 - k\left(T_{\mathrm{h}} - T_{\mathrm{c}}\right). \tag{1.0.8}$$

the first term represents the Peltier cooling, the second term is the Joule heat that returns to the cold end, and the third term accounts for parasitic heat conduction from the hot end to the cold end. The maximum COP is given by

$$\mathrm{COP}_{\max} = \frac{T_{\mathrm{c}}}{T_{\mathrm{h}} - T_{\mathrm{c}}} \frac{\sqrt{1+ZT} - \frac{T_{\mathrm{h}}}{T_{\mathrm{c}}}}{\sqrt{1+ZT}+1}. \tag{1.0.9}$$

Similar to that of the TE generator, when *ZT* is much larger than 1, the COP approaches Carnot efficiency.

1.1 Materials for Thermoelectric Applications

1.1.1 Bulk Thermoelectric Materials

A good TE material needs to have both high electrical conductivity and low thermal conductivity. In most solids, these two physical properties are positively correlated (e.g., the Wiedemann-Franz relation [8]). Furthermore, the Seebeck coefficient and electrical conductivity are negatively correlated.

The Seebeck coefficient for metals and degenerate semiconductors is given by [9]

$$S = \frac{2k_B^2}{3e\hbar^2} Tm^* \left(\frac{\pi}{3n}\right)^{2/3}, \tag{1.1.1}$$

where k_{B} is the Boltzmann constant, $\hbar$ is the reduced Planck constant, e is the elementary charge, m^* is the effective mass of the carrier, and n is the carrier concentration.

The electrical conductivity as a function of the carrier concentration and mobility (μ) can be defined as [8]

$$\sigma = ne\mu \tag{1.1.2}$$

Eqs. (1.2.1) and (1.2.2) show that a low carrier concentration gives a large *S*, but at the same time decreases σ. A high carrier effective mass provides a higher *S*, but it also creates another conflict with σ, since heavier carriers move with slower velocity and therefore with smaller mobility. Improving one thermoelectric parameter could mean that the other one declines, resulting in a poor value of *ZT*.

Several key studies have surveyed the developments in bulk materials. [9] [10] An ideal TE material which possesses the poor thermal properties of a glass and the excellent electronic properties of a crystal is known as a phonon glass electron crystal (PGEC). Skutterudites [11], clathrates [12], and other open cage structures may possess these features. These compounds have cage-like crystal structures filled with atoms that effectively rattle around. The "rattling" interferes with the conduction of heat but not electricity. Rare-earth compounds and intermetallics are another group of potential TE materials due to their large Seebeck coefficients. [13] *ZT* of the most common bulk TE materials are summarized in Fig. 1.3.

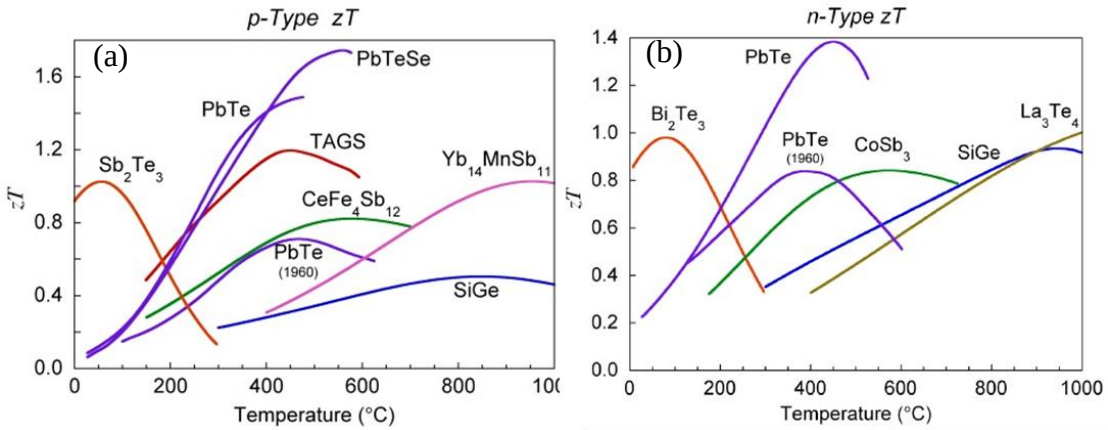

Figure 1.3 *ZT* of state-of-the-art commercial materials and those used or being developed by NASA for thermoelectric power generation. (a) *p*-type. (b) *n*-type. Reproduced from [9].

Note that the peaks of *ZT* for these materials are mostly above room temperature. For TE cooling below room temperature, poor mechanical properties limit the usage

of Bi/Sb-based alloys. [9] The integration of TE devices made from bulk materials with optoelectronic devices is another difficult challenge. [3] Fig. 1.4 illustrates the incompatibilities between vertical-cavity surface-emitting laser (VCSEL) and bulk TE coolers as an example. The feature length of one element inside the VCSEL array is less than 10μm. [14] For a bulk TE module, one element is at the size of 100μm. [15] The heating density of VCSEL is typically above 100W/cm^2 whereas the cooling density of bulk TE cooler is approximately 30W/cm^2. [15] [16] The fabrication difference (VCSEL is fabricated through integrated circuit fabrication technology, while bulk TE cooler is individually fabricated) adds to the cost of production because of packaging; thus, alternative solutions such as thin film TE coolers are needed.

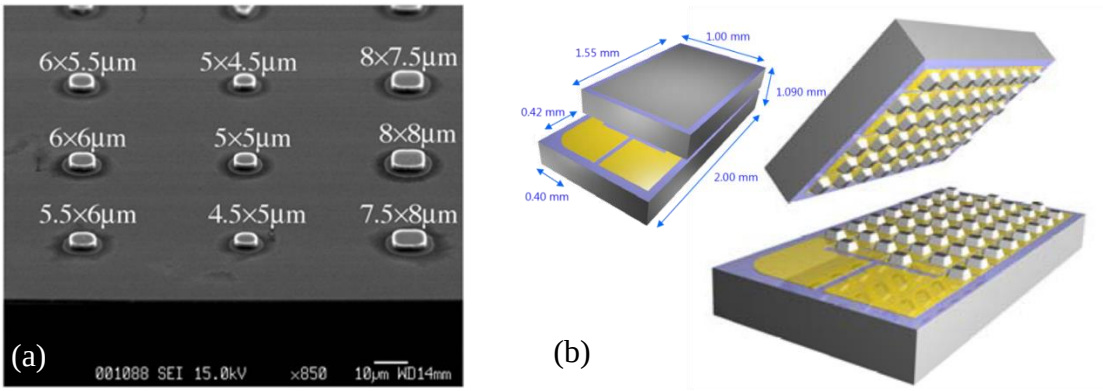

- IC fabrication technology
- High heating density
- Small size

- Individually fabricated
- Small cooling density
- Big size

Figure 1.4 Characteristic incompatibilities between VCSEL and bulk TE cooler. (a) VCSEL SEM [14]. (b) Micro TE cooler [15].

1.1.2 Low-dimensional Thermoelectric Materials

Due to the limitations of bulk materials, researchers have attempted to improve *ZT* using low-dimensional structures. Advanced fabrication techniques for superlattices (SLs), nanowires/nanotubes, and quantum dots have opened the door to new classes of TE materials.

The additional new degree of freedom, such as the length scale of a material, can

contribute to an increase in efficiency and power output by decoupling σ from *S* and *k*. To explain this, we refer to the Seebeck coefficient derivation simplified for metals and degenerate semiconductors by Clutter and Mott [17]:

$$S = \frac{\pi^2 k_B^2}{3e} T \frac{\mathrm{d}\left[\ln\left(\sigma(E)\right)\right]}{\mathrm{d}E}\Big|_{E=E_F} = \frac{\pi^2 k_B^2}{3e} T \left\{ \frac{1}{n}\frac{\mathrm{d}n(E)}{\mathrm{d}E} + \frac{1}{\mu}\frac{\mathrm{d}\mu(E)}{\mathrm{d}E} \right\}_{E=E_F}, \qquad (1.1.3)$$

which shows that the Seebeck coefficient could be enhanced by increasing the energy dependence of electrical conductivity near the Fermi level. Two mechanisms can increase *S*:

i) An increased energy dependence of carrier density, which is a function of the electronic density of states D_g (for instance, by a local increase in D_g).

ii) An increased energy dependence of mobility, for instance, by a scattering mechanism that strongly depends on the energy of the charge carriers.

The first mechanism to enhance density of states potentially could be obtained by working with low-dimensional structures. Fig 1.5 shows the energy dependence of D_g from bulk material to 2D, 1D, and 0D systems. Referring to Eq. (1.1.3), Fig. 1.5 shows that larger asymmetry in low-dimensional systems compared to bulk materials, could enhance the *S* value substantially. In an SL structure, an improvement in *S* over the bulk material has been discovered. [18] In a nanowire system, *S* measured from Bi nanowire composites increased significantly compared to that of bulk Bi by size quantization effects, and also because size quantization opens a bandgap in Bi nanostructures. [18]

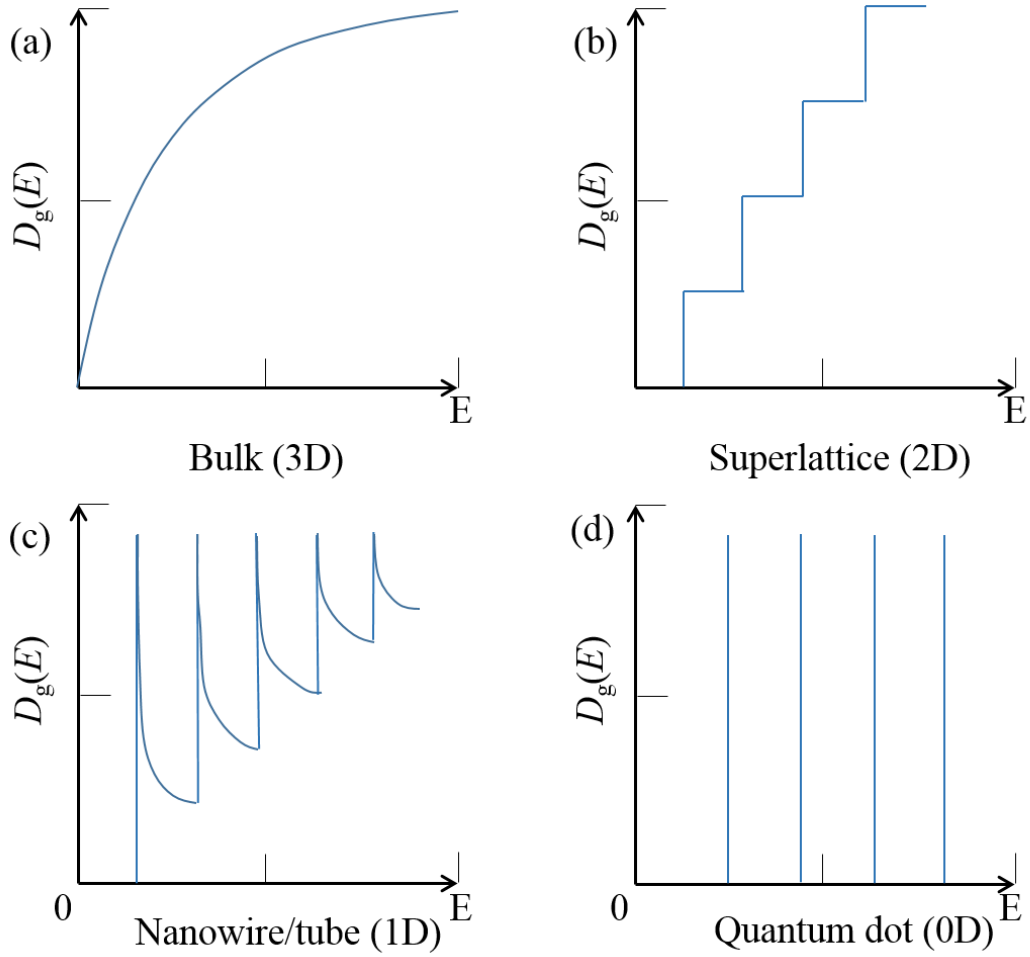

Figure 1.5 Schematic diagram for the energy dependence of the electronic density of states. (a) 3D system. (b) 2D system. (c) 1D system. (d) 0D system.

A second mechanism to increase the carrier mobility at a given carrier concentration is electron energy filtering. [19] In SLs, electron energy filtering consists of using potential energy barriers that filter electrons according to their energy band, thus promoting thermionic current emission. In [20], the room temperature *ZT* is predicted to increase by a factor of 10 in $In_{0.53}Ga_{0.47}As$/ $In_{0.53}Ga_{0.28}Al_{0.19}$ SLs compared to their bulk counterparts, where 65% of the increase is due to electron filtering and the remaining 35% is due to a reduced thermal conductivity. Furthermore, in [20] electron filtering allows higher doping concentration for the increased Seebeck coefficient, thus achieving higher power factors ($S^2\sigma$).

In 1D system, the phonon-drag effect has been known to increase Seebeck coefficient, because the restriction of the interaction between phonons and electrons imposed by energy and momentum conservation along the confinement direction is removed. [21] Silicon nanowires with p-type doping of $7\times10^{19}cm^{-3}$ achieved ZT~1 at 200K, [22] whereas the bulk alloy was only ~0.2 at 300K [9]. The very high Seebeck coefficient (~400μV/K) for the nanowire case is one of the main contributors to the measured ZT.

Reducing thermal conductivity is another major focus of research. The thermal conductivity of a SL can be much lower than that of its bulk material constituents and equivalent composition alloy. Phonons can be strongly scattered at interfaces formed by different layers due to phonon mismatch. [23] A reduction in the phonon group velocity can also be produced. [24] [25] The cross-plane thermal conductivity of Bi_2Te_3/Sb_2Te_3 SL has been found reduced from that of $Bi_{0.5}Sb_{1.5}Te_3$ alloy by a factor of 2.2. [26] The cross-plane thermal conductivity of strained SiGe SLs was 3~10 times lower than the alloy value. [27] Doped nanowires reached ultra-low thermal conductivities similar or lower than the theoretical limit for bulk Si [22] [28] for two reasons. First, the low frequency phonons whose wavelengths are longer than the length of nanowire cannot survive in nanowire, i.e., the low frequency contribution to thermal conductivity, which is substantial and significant, is largely reduced. Second, because of the large surface to volume ratio, the boundary scattering in quasi-1D structures is also significant.

1.1.3 Material systems in this work

This work examines low-dimensional TE materials for applications near and below room temperature. For a 2D structure, HgCdTe (MCT) SL system is chosen. MCT is currently the dominant material for infrared (IR) sensing and imaging, which is often performed at cryogenic temperatures to increase signal-to-noise ratio.

Monolithically integrated cooling could be achieved by growing MCT IR pixel elements above the MCT SL which functions as the TE cooler, analogous to approaches used in GaAs/InGaAsP and Si/Ge systems. [29] [30]

To examine 1D structures, pristine/coated SWNT networks and single doped SWNT are studied. Theoretical simulation predicts high *ZT* (>2) for semiconducting SWNTs, with a very high Seebeck coefficient (> 500 μV/K). [31] Many experimental studies, however, indicate that *S* of CNTs/ CNT networks is low, e.g., 20 – 40μV/K [32] [33] [34], and the *ZT* value is normally in range of 10^{-3} – 10^{-2}. Pristine CNTs purified with standard procedures generally show positive *S*, indicating the major charge carriers are holes. The Seebeck coefficient of CNTs can change sign through *n*-type doping, and the highest negative value achieved is approximately -40 μV/K. [35] Doping CNT networks with polymer molecules and polymeric compounds can increase *S* to 50 – 80 μV/K [35] [36], possibly due to the modification of the electronic density states near the Fermi level of the networks, where *S* increases as suggested by Eq. (1.1.3). This may also because the absorbed molecules increase the inter-tube hopping barriers for charge carriers, since reduced electrical conductivities are observed in these doped CNT networks. Ar-plasma treated CNT sheets cause a significant enhancement in Seebeck coefficient; the maximum Seebeck coefficient (e.g. >300μV/K) as well as a large reduction in the thermal conductivity are found at a high temperature range, and a *ZT* of 0.4 is obtained.

In this work we investigate the nitrogen doped SWNTs, because they are promising candidates for various applications including field effect transistors, biosensors and metal storage. [37]

CNTs are also extensively used as fillers in polymer composites and the electrical conductivity of such composites are orders of magnitude higher than other polymer composites containing different conductive fillers. CNT based organic composites that

could be good TE materials are summarized in Table 1.1. [38] [39] [40] In this work, the thermoelectric properties of pristine/ graphene-/ BN-/ PEDOT:PSS-coated SWNT networks are measured and the coating effects on TE properties are analyzed.

Table 1.1 Thermoelectric properties of CNT based organic polymer composites.

TE materials	σ S/m	*S* μV/K	*k* W/m·K
CNT(60%)+PEDOT:PSS(30%)+PVA(10%) [38]	1.35E5	160	0.2–0.4[1]
CNT(20%)+PEI(10%)+SDBS(60%) [39]	1200	–70	
CNT(20%)+PEI(40%)+SDBS(4%) [39]	600	–100	
FWNT(30%)+Nafion(70%) [40][2]	1400	30	

[1] Thermal conductivity is measured in the out-of-plane direction and electrical conductivity and the Seebeck coefficient are measured along the in-plane direction.
[2] FWNT means few-walled nanotube.

1.2 Thesis Outline

Chapter 2 provides the measurement results of thermal conductivity, electrical conductivity, and Seebeck coefficient of MCT SLs from 100K to 300K. This is the first experimental research of TE properties of MCT SL down to cryogenic temperature. The phonon dispersion of SL is calculated using an elastic continuum model to explain the temperature independent thermal conductivity. It is found that even large period SLs can reduce thermal conductivity effectively due to the folding effect.

Chapter 3 provides the measurement results of TE properties of pristine/ graphene-/ BN-/ PEDOT:PSS-coated SWNT networks from 100K to 300K. Coated networks have smaller conductivities and Seebeck coefficients than pristine networks. Analysis model based on scaling rules of rod-like network is developed and applied to separate the effect of tubes and junctions. The model is also applied to other SWNT

networks. It is found that the coatings outside the SWNT reduce the conductivity within the tube significantly. The reduction of thermal conductivity is consistent of a phonon mean free path analysis. The junction conductance derived from ultralow density networks consists well with the simulation result of a single junction whereas the junction conductance derived from dense networks are much smaller. The results suggest the possible phonon coherence in dense networks.

Chapter 4 describes the use of molecular dynamics to simulate thermal conductivities of nitrogen doped SWNTs as functions of doping type, doping concentration and tube length. Low doping concentration is sufficient to reduce thermal conductivity. Combining their effects on electrical conductivity shows that substitutional nitrogen doped CNT is a potential candidate for TE applications. The typical phonon relaxation time, defect formation energy, and phonon density of states are calculated to explain the thermal conductivity results. We expect the greatly shortened phonon lifetimes account for the reduced thermal conductivities. This expectation is confirmed in Chapter 5.

Chapter 5 describes a computationally efficient simulation method based on dynamic structure factors developed particularly for CNT systems. The phonon dispersion curves and phonon lifetime of the SWNTs in Chapter 4 are calculated. The results in Chapters 4 and 5 are consistent.

Chapter 6 concludes and suggests future research directions.

[1] K. Biswas, J. He, I. D. Blum, C. I. Wu, T. P. Hogan, D. N. Seidman, V. P. Dravid and M. G. Kanatzidis, "High-performance bulk thermoelectrics with all-scale hierarchical architecturs," *Nature*, vol. 489, p. 414, 2012.

[2] C. Watkins, B. Shen and R. Venkatasubramanian, "Low-grade-heat energy harvesting using superlattice thermoelectrics for applications in implantable medical devices and sensors," in *Proc. Int. Conference on thermoelectrics*, 2005.

[3] L. Rushing, A. Shakouri, P. Abraham and J. E. Bowers, "Micro thermoelectric coolers for integrated applications," in *Proceedings of conference on optoelectronic and microelectronic materials and devices*, Perth, Australia, 1997.

[4] T. A. Corser, "Qualification and reliability of thermoelectric coolers for use in laser modules," in *41st Electronic components and technology conference*, Atlanta, USA, 1991.

[5] G. J. Snyder, J. P. Fleurial, T. Caillat, R. Yang and G. Chen, "Supercooling of Peltier cooler using a current pulse," *J. Appl. Phys.*, vol. 92, p. 1564, 2002.

[6] Z. G. Chen, G. Han, L. Yang, L. Cheng and J. Zou, "Nanostructured thermolelctric materials: current reserach and future challenge," *Prog. Nat. Sci: Mater. Inter.*, vol. 22, p. 535, 2012.

[7] D. M. Rowe, CRC handbook of thermoelectrics, New York: CRC, 1995.

[8] C. Kittel, Introduction to solid state physics, New York: Wiley, 1996.

[9] G. J. Snyder and E. S. Toberer, "Complex thermoelectric materials," *Nature Mater.*, vol. 7, p. 105, 2008.

[10] A. J. Minnich, M. S. Dresselhaus, Z. F. Ren and G. Chen, "Bulk nanostructured thermoelectric materials: current research and future prospects," *Energy Environ. Sci.*, vol. 2, p. 466, 2009.

[11] B. C. Sales, D. Mandrus, B. C. Chakoumakos, V. Keppens and J. R. Thompson, "Filled skutterudite antimonides: electron crystals and phonon glasses," *Phys. Rev. B*, vol. 56, p. 15081, 1997.

[12] X. Shi, J. Yang, S. Bai, J. Yang, H. Wang and M. Chi, "On the design of high-efficiency thermoelectric clathrates through a systematic cross-substitution of framework elements," *Adv. Func. Mater.*, vol. 20, p. 755, 2010.

[13] G. D. Mahan, "Rare earth thermoelectrics," in *Proceedings of the 16th international conference on thermoelectrics*, Dresden, Germany, 1997.

[14] H. Kawaguchi, "Polarization bistable VCSELs and its application to optical buffer memory," http://mswebs.naist.jp/LABs/kawaguchi/research-e.html.

[15] M. Inc., "Ultra-small Peltier Coolers (datasheet from MICROPELT)," http://micropelt.com/downloads/datasheet_mpc_d403_d404.pdf, 2006.

[16] H. Monch and G. Derra, "High power VCSEL systems: a tool for digital thermal processing," *Laser Technik J.*, vol. 2, p. 43, 2014.

[17] J. P. Heremans, V. Jovovic, E. S. Toberer, A. Saramat, K. Kurosaki, A. Charoenphakdee, S. Yamanaka and G. J. Snyder, "Enhancement of thermoelectric efficiency in PbTe by distortion of the electronic density of states," *Science*, vol. 321, p. 554, 2008.

[18] J. P. Hermans, C. M. Thrush, D. T. Morelli and M. C. Wu, "Thermoelectric Power of Bismuth Nanocomposites," *Phys. Rev. Lett.,* vol. 88, p. 216801, 2002.

[19] D. Vashaee and A. Shakouri, "Improved thermoelectric power factor in metal-based superlattices," *Phys. Rev. Lett.,* vol. 92, p. 10, 2004.

[20] J. M. O. Zide, D. Vashaee, Z. X. Bian, J. E. Bowers, A. Shakouri and A. C. Gossard, "Demonstration of electron filtering to increase the Seebeck coefficient in $In_{0.53}Ga_{0.47}As/In_{0.53}Ga_{0.28}Al_{0.19}As$ superlattices," *Phys. Rev. B,* vol. 74, p. 205335, 2006.

[21] M. Tsaousidou, "Theory of phonon-drag thermopower of extrinsic semiconducting single-wall carbon nanotubes and comparison with previous experimental data," *Phys. Rev. B,* vol. 81, p. 235425, 2010.

[22] A. I. Boukai, Y. Bunimovich, J. Tahir-Kheli, J. K. Yu, W. A. Goddard III and J. R. Heath, "Silicon nanowires as efficient thermoelectric materials," *Nature,* vol. 451, p. 168, 2008.

[23] E. T. Swartz and R. O. Pohl, "Thermal boundary resistance," *Rev. Mod. Phys.,* vol. 61, p. 605, 1989.

[24] A. Balandin and K. L. Wang, "Effect of phonon confinement on the thermoelectric figure of merit of quantum wells," *J. Appl. Phys.,* vol. 84, p. 6149, 1998.

[25] M. V. Simkin and G. D. Mahan, "Minimum thermal conductivity of superlattices," *Phys. Rev. Lett.,* vol. 84, p. 5, 2000.

[26] R. Venkatasubramanian, E. Siivola, T. Colpitts and B. O'Quinn, "Thin-film thermoelectric devices with high room-temperature figures of merit," *Nature,* vol. 413, p. 597, 2001.

[27] W. L. Liu, T. Borca-Tasciuc, G. Chen, J. L. Liu and K. L. Wang, "Anisotropic thermal conductivity of Ge quantum-dot and symmetrically strained Si/Ge superlattices," *J. Nanosci. Nanotech.,* vol. 1, p. 39, 2001.

[28] N. Yang, G. Zhang and B. Li, "Ultra-low Thermal Conductivity of Isotope Doped Silicon Nanowires," *Nano Lett.,* vol. 8, p. 276, 2008.

[29] C. LaBounty, A. Shakouri, P. Abraham and J. E. Bowers, "Monolithic integration of thin-film coolers with optoelectronic devices," *Opt. Eng.,* vol. 11, p. 2847, 2000.

[30] A. Shakouri and Y. Zhang, "On-chip solid-state cooling for integrated circuits using thin-film microrefrigerators," *IEEE Trans. Comp. Pack. Tech.,* vol. 28, p. 65, 2005.

[31] K. Esfarjani, M. Zebarjadi and Y. Kawazoe, "Thermoelectric properties of a

nanocontact made of two-capped single-wall carbon nanotubes calculated within the tight-binding approximation," *Phys. Rev. B,* vol. 73, p. 085406, 2006.

[32] C. Yu, L. Shi, Z. Yao, D. Li and A. Majumdar, "Thermal conductance and thermopower of an individual single-wall carbon nanotube," *Nano Lett.,* vol. 5, p. 1842, 2005.

[33] L. Grigorian, K. Williams, S. Fang, G. U. Sumanasekera, A. L. Loper, E. C. Dickey, S. J. Pennycook and P. C. Eklund, "Reversible Intercalation of Charged Iodine Chains into Carbon Nanotube Ropes," *Phys. Rev. Lett.,* vol. 80, p. 5560, 1998.

[34] K. J. Zhang, A. Yadav, K. H. Kim, Y. Oh, M. F. Islam, C. Uher and K. P. Pipe, "Thermal and electrical transport in ultralow density single-walled carbon nanotube networks," *Adv. Mater.,* vol. 25, p. 2926, 2013.

[35] M. Piao, M. R. Alam, G. Kim, U. Dettlaff-Weglikowska and S. Roth, "Effect of chemical treatment on the thermoelectric properties of single walled carbon nanotube networks," *Phys. Status Solidi B,* vol. 249, p. 2353, 2012.

[36] G. U. Sumanasekera, B. K. Pradhan, H. E. Romero, K. W. Adu and P. C. Eklund, "Giant thermopower effects from molecular physisorption on carbon nanotubes," *Phys. Rev. Lett.,* vol. 89, p. 166801, 2002.

[37] C. P. Ewels and M. Glerup, "Nitrogen doping in carbon nanotubes," *J. Nanosci. Nanotech.,* vol. 5, p. 1345, 2005.

[38] C. Yu, K. Choi, L. Yin and J. C. Grunlan, "Light-Weight Flexible Carbon Nanotube Based Organic Composites with Large Thermoelectric Power Factors," *ACS Nano,* vol. 5, p. 7885, 2011.

[39] D. D. Freeman, K. Choi and C. Yu, "N-Type thermoelectric performance of functionalized carbon nanotube-filled polymer composites," *PLOS ONE,* vol. 7, p. 1, 2012.

[40] Y. Choi, Y. Kim, S. G. Park, Y. G. Kim, B. J. Sung, S. Y. Jang and W. Kim, "Effect of the carbon nanotube type on the thermoelectric properties of CNT/Nafion nanocomposites," *Org. Electro.,* vol. 12, p. 2120, 2011.

Chapter 2

Thermoelectric Properties of MBE-grown MCT SLs

2.0 Introduction

Mercury cadmium telluride (MCT or Hg_{1-x} Cd_xTe) has shown promise as a thermoelectric (TE) material, particularly at low temperatures. [1] [2] The thermal conductivity of bulk $Hg_{1-x}Cd_xTe$ (MCT) is much lower than that of typical group III-V or II-VI semiconductors due to the large masses of the constituent atoms. And the electron mobility of MCT/ MCT epitaxial films is high (1.6×10^5 cm^2/Vs and 10^5 cm^2/Vs respectively [3]). Simulation models [1] [2] predict that the thermoelectric figure of merit (*ZT*) of MCT superlattices (SLs) can be greater than 2 in both room-temperature and cryogenic temperature, which is more than twice that achieved in the best measured thermoelectric materials [4] at this temperature range (which are based on bulk $Bi_{2-x}Sb_xTe_3$). The high electron mobility of MCT allows it to benefit from electron energy filtering. Since energy filtering introduced by barriers brings additional electron scattering and may thereby reduce electron mobility, materials with high bulk electrical mobility such as MCT are preferred. The energy filtering effect has been found in long-period MCT SL by enabling several subbands to contribute to Seebeck, while the energy filtering effect is negligible in small-period MCT SL. [1]

In this work long-period MCT SLs are studied, which have the potential to be

integrated with MCT IR sensors and provide very precise localized cooling, taking advantage of the supercooling effect [5] [6]. During transient operation, an energy-efficient rastered approach can be carried out in which a large current pulse is applied only to the TE elements beneath the pixel currently being read out. The thermal and electrical properties of MCT SLs at low temperature are also important for MCT SLs based VLWIR detectors, focal plane arrays, and infrared emitters.

SLs present an anisotropic behavior, with different thermal conductivity in the in-plane and cross-plane directions. The in-plane thermal conductivity does not differ much from bulk values. [7] This work focuses on cross-plane properties (along the growth direction), which are more relevant for monolithically integrated TE coolers.

2.1 Fabrication and Characterization Techniques

Molecular beam epitaxy (MBE) is the best available technology for growing high-quality MCTs and it also produces third-generation multi-spectral IR detectors. Compared to other epitaxial methods, MBE has the lowest substrate temperature and the most precise control of thermal evaporation, which limits diffusion at the interfaces. Furthermore MBE allows the growth processes to be monitored by various in-situ technologies such as reflection high-energy electron diffraction (RHEED) to control the deposition of metal seeds and interface formation, and spectroscopic ellipsometry (SE) to characterize the composition and thickness. In summary, MBE creates MCT SLs with sharp interfaces and highly controlled layer thicknesses. [8]

Samples used in this work is grown by EPIR Technologies: $Hg_{0.8}Cd_{0.2}Te$ (252Å)/ $Hg_{0.2}Cd_{0.8}Te$ (376Å) SLs are grown in a Riber 32P MBE system on a silicon substrate with 8mm CdTe and 2.5mm $Hg_{0.5}Cd_{0.5}Te$ buffer layers deposited first. Solid CdTe, Te, and Hg are used as source materials. The Hg flux is controlled by adjusting the corresponding valve and the cell temperature. Two Te effusion cells are mounted for

separate control of HgCdTe layers with different compositions of the SL. The flux of the CdTe and two Te cells are controlled by using different cell temperatures in order to obtain the HgCdTe target composition and growth rate. More details can be found in [8].

2.1.1 Cross-plane Thermal Conductivity and the Seebeck Coefficient

3ω method, the most popular technique used to determine the thermal conductivity of thin films, [9] [10] is based on a metal line with four contacts which work as both a heater and a thermometer, as shown in Fig. 2.1 (a). Driving a sinusoidal current at frequency ω through the metal line heats up the sample and creates a thermal wave at frequency 2ω. Due to the temperature dependent resistance of the heater, the resistance also oscillates at twice the frequency. The oscillation of the resistance at 2ω combined with the current at ω leads to a voltage signal at 3ω. By measuring the voltage signal, the temperature oscillation can be calculated from

$$\Delta T = \frac{2RV_3}{V_1}\frac{dT}{dR}, \tag{2.1.1}$$

where R is the average conductivity of the metal line, V_1 is the voltage across the line at ω, and V_3 is the voltage across the line at 3ω.

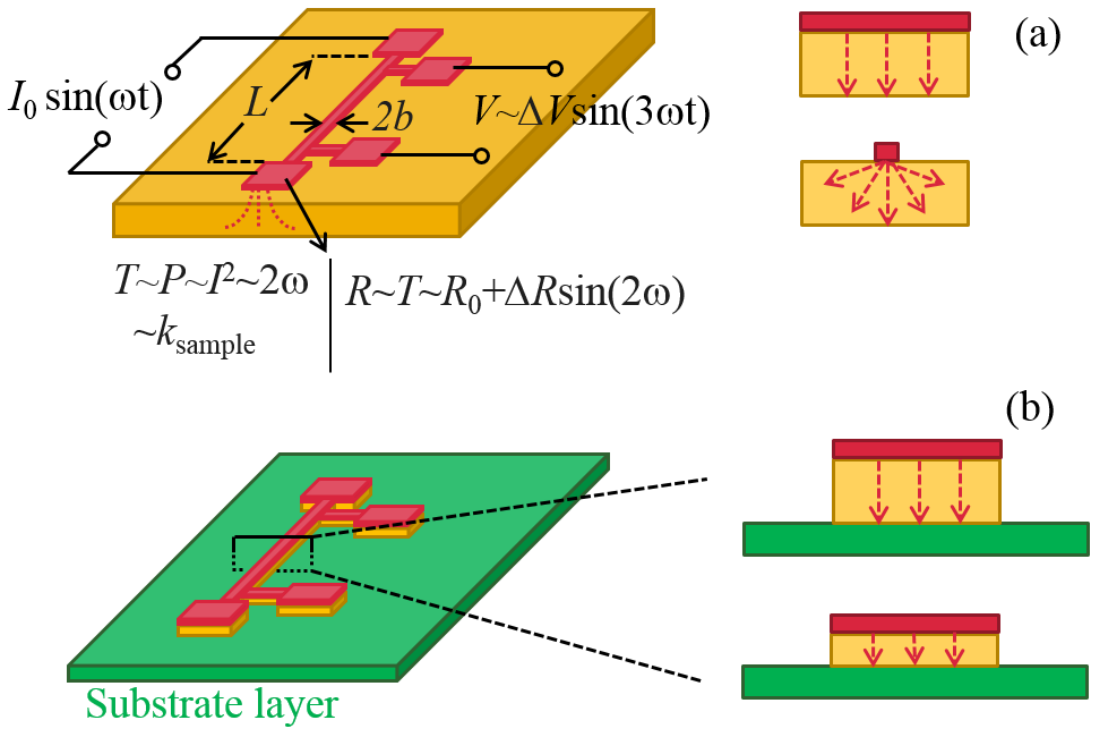

Figure 2.1 Schematic of (a) standard 3ω method with cross-section view, and (b) differential 3ω method with cross-section view.

If the heater is very narrow, it acts almost like an isotropic heat source, and if it is very wide compared to the film thickness, it provides a near one-dimension uniform heat flow as shown in Fig. 2.1 (a). The first option is used for extracting in-plane thermal conductivity and the second one is used for cross-plane measurements.

The thermal penetration depth is defined as $\sqrt{\zeta/2\omega}$, where ζ is the thermal diffusivity of the measured film. Thermal penetration depth characterizes how deep the heat wave penetrates the film at a certain current frequency. [10] Using the thermal conductivity of $Hg_{0.75}Cd_{0.25}Te/Hg_{0.7}Cd_{0.3}Te$ SL at 300K (0.82W/m·K) [8], density and specific heat of $Hg_{0.5}Cd_{0.5}Te$ (6961kg/m^3, 0.194J/g·K) [3], gives an estimated thermal diffusivity of 0.6mm^2/s. A frequency at least 193Hz is needed to get a penetration depth lower than 2μm (the usual thickness of the SLs). We use a differential 3ω technique to lower the frequency limitation, and eliminate the effects of the substrate, the insulating layers, and the interfaces on the voltage and

temperature measurements. [10] To ensure one-dimensionality of the heat conduction, we process the SL layers to yield a mesa structure with a geometry similar to that of the heating line. We obtain reference samples by performing inductively coupled plasma (ICP) etching on full height SLs to remove half of the materials, which have the same structure except for a thinner SL, as shown in Fig. 2.1(b). The cross-plane SL thermal conductivity is given by

$$k = \frac{t_{\mathrm{F}} - t_{\mathrm{Ref}}}{2b}\left[\frac{P/l}{\Delta T_{\mathrm{F}}} - \frac{P/l}{\Delta T_{\mathrm{Ref}}}\right], \tag{2.1.2}$$

where b is the half-width of the heating line, t is the sample thickness, P/l is the applied heater power per unit length, and subscriptions *F* and *Ref* represent the full height and reference samples, respectively.

To measure cross-plane thermal conductivity and Seebeck coefficient simultaneously, we use a modified differential 3ω method. [11] A microprobe between the SL and top heater together with a contact probe away from the SL mesa, are used to measure the 2ω Seebeck voltage. The fabrication process as shown in Fig. 2.2 begins with depositing 0.3μm thick ZnS on the sample. Then a small window is opened in this ZnS layer and an Au microprobe is deposited right above it as electrical contact. After that another 0.15μm thick ZnS layer is deposited to insulate the microprobe from the top heater. The contact window length is equal to that of heating line, and its width is slightly smaller than heating line so that the insulation is secure. Then, etching away SL except for the area beneath the heating line to yield the mesa structure.

Since the Seebeck coefficient of the Au leads is much smaller than that of the semiconductor SL, and we used a differential method, the contributions of the Au leads to the measured Seebeck coefficient is negligible. The magnitude of the

cross-plane Seebeck coefficient of the SL can be given as

$$|S_{SL}| = \left|\frac{\Delta V_{2\omega}}{\Delta T_{2\omega}}\right| = \left|\frac{V_{2\omega,F} - V_{2\omega,SL}}{T_{2\omega,F} - T_{2\omega,SL}}\right| \tag{2.1.3}$$

Our experiment shows that $\Delta V_{2\omega}$ varies linearly with $\Delta T_{2\omega}$, but does not go to 0 whereas $\Delta T_{2\omega}$ reaches 0. Therefore, Seebeck coefficient is determined by $d(\Delta V_{2\omega})/d(\Delta T_{2\omega})$ instead of Eq. (2.1.3) by using several heater powers.

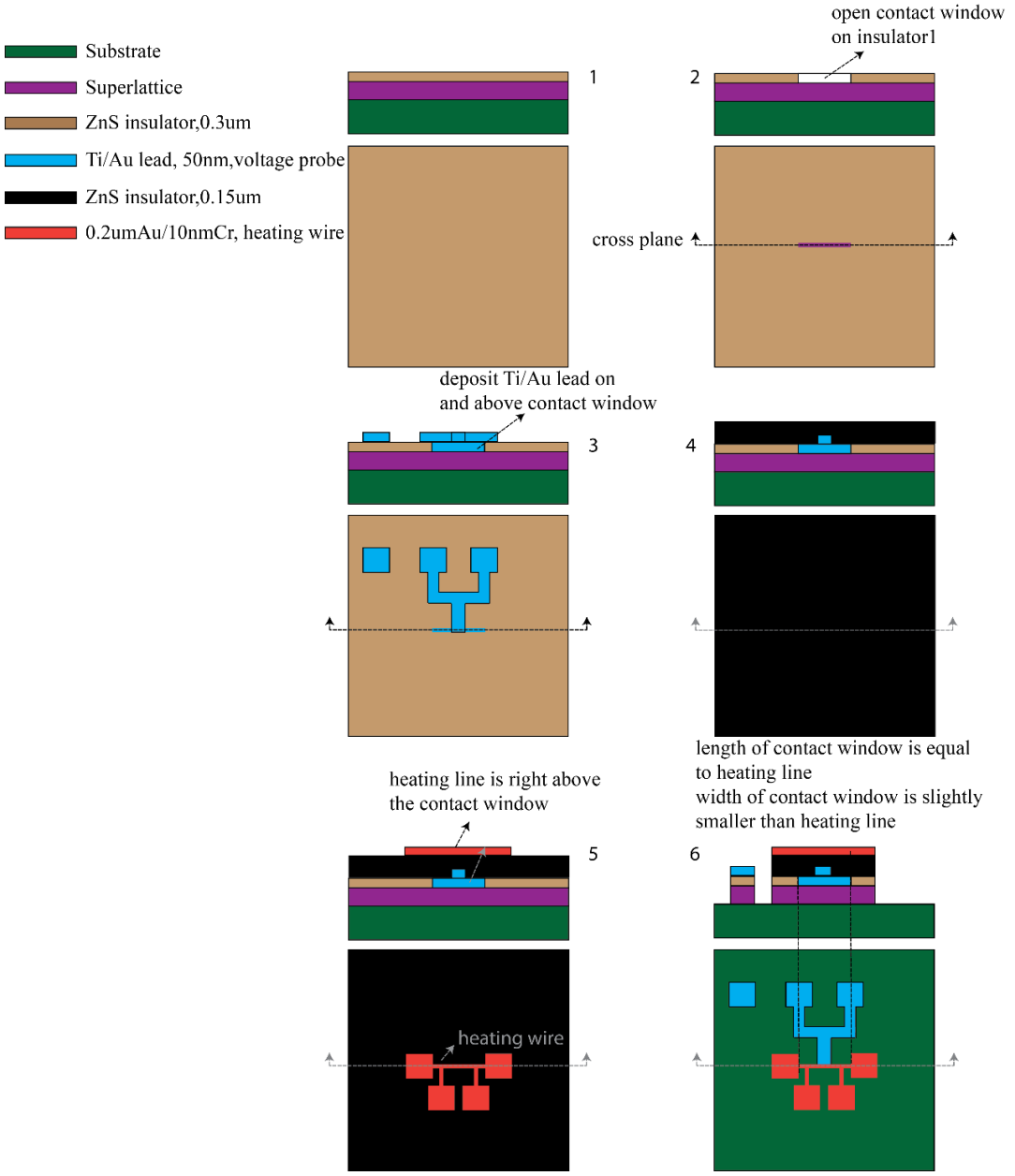

Figure 2.2 Sample fabrication process for modified differential 3ω method. The number just above each subplot represents the procedure sequence.

We mount the samples on the cold finger of a cryostat using a removable copper block. The contact pads of the heating line are wire bonded to external BeO chips with separate heatsinks to remove parasite heat. The BeO chips are in turn connected to a 10-pin vacuum feedthrough using copper wires. The cryostat is pumped to vacuum ($<1\times10^{-5}$ Torr) and a copper cylinder is used as a radiation shield to remove parasite temperature gradients caused by radiative heat transfer between the cold finger and surroundings. The electronic measurement setup includes a harmonic oscillator used to drive a bidirectional current source consisting of a Howland current pump circuit and a buffer amplifier to increase the current output. The current source provides a current input (30 – 1500Hz) to the heating wire. We measure the 1ω and 3ω voltages with a Stanford Research SR830 dual phase lock-in amplifier. In detail, we determine the current by connecting heating line and a precise heat sink resistor in series and measuring the 1ω voltage drop across the resistor using the lock-in amplifier. We slowly heat the wire from 77K to 295 K to determine the temperature coefficient of resistance and measure the resistance of the wire using a four-probe method while simultaneously measuring the sample temperature. A photograph of our experimental setup is shown in Fig. 2.3.

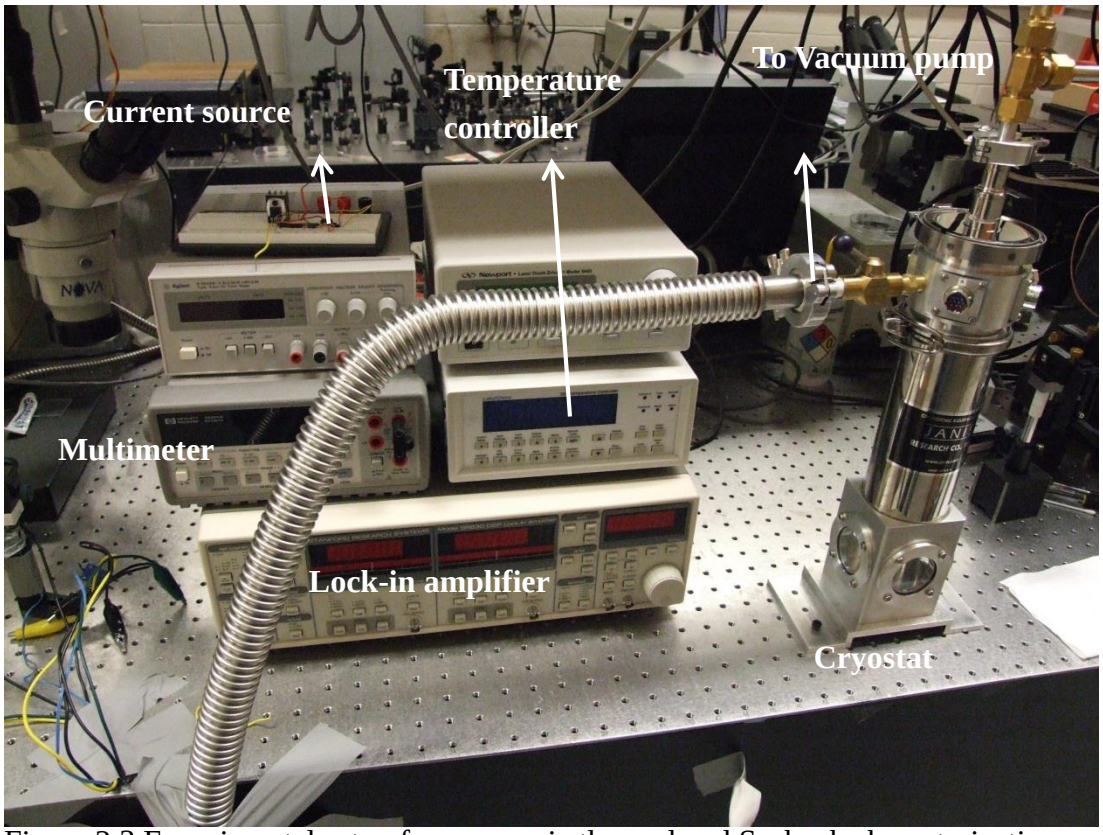

Figure 2.3 Experimental setup for cryogenic thermal and Seebeck characterization.

2.1.2 Cross-plane electrical conductivity

We find the cross-plane electrical conductivity of the SLs by using a modified transmission-line method (TLM). [7] TLM was first proposed to determine the contact resistance for planer ohmic contacts. The structure consists of identical contacts of length L and width W spaced by different distance di. We etch a mesa structure of width Z on the thin film under characterization and pattern the TLM structure on top of the mesa as shown in Fig. 2.4 (a). The mesa structure gives a homogenous distribution of the current density under the contacts. Assuming the contact resistance R_C is the same for all the contact, the measured total electrical resistance R_T between two contacts is given by

$$R_T = \frac{R_{sh}}{W} d_i + 2R_C , \qquad (2.1.4)$$

where R_{sh} is the sheet resistance.

The linear relation given by Eq. (2.1.4) is shown in Fig. 2.4 (b). Note that R_{sh} can be calculated by the slope of the curve times the contact width W. The intercept resistance R_0 is 2 times the contact resistance. The length of current transfer at the contact, L_C, can be extracted when $R_T = 0$.

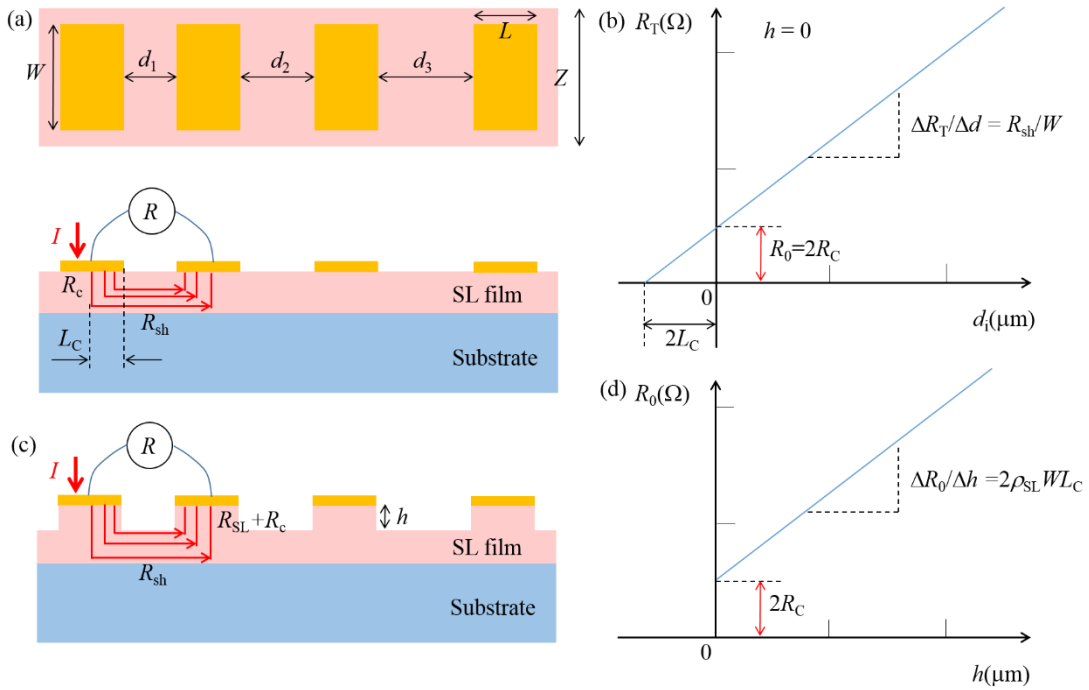

Figure 2.4 (a) Schematic diagram of TLM structure patterned on top of a mesa structure of width Z. Top view and side view. (b) Representative total resistance measured from the TLM structure shown in (a) as a function of spacing between contacts. (c) Schematic diagram of modified TLM structure after etching down the SL layer to create the mesa structure. (d) Representative intercept resistance measured from TLM structure in (c) as a function of mesa height.

Here, the modification is to etch down the SL except for the area underneath the metal contacts so that we create a mesa structure with height of h as shown in Fig. 2.4 (c). The R_T now becomes

$$R_T = \frac{R_{sh}}{W} d_i + 2\left(R_C + \rho_{SL} h L_C W\right), \tag{2.1.5}$$

where ρ_{SL} is the cross-plane electrical resistivity of SL. We use mesa structures with different heights to extract ρ_{SL}, which can be sensitively measured from R_0 as a

function of *h* as shown in Fig. 2.4 (d).

2.2 Results and discussion

As shown in Fig. 2.5, the MCT SL shows an almost constant thermal conductivity of 1 W/m·K over the entire temperature range studied, which is 25% less than the model predictions for the $Hg_{0.8}Cd_{0.2}Te$ bulk alloy at 295K and 66% less than the bulk alloy value at 80K. [3] The measured MCT SL thermal conductivity is below the predicted bulk alloy limit for $Hg_{1-x}Cd_xTe$ over the range x = 0 to 0.4, which occurs for $Hg_{0.7}Cd_{0.3}Te$ [3] It is comparable to the lowest thermal conductivities reached in other leading SL-based TE systems such as $IrSb_3/CoSb_3$ (0.8–1.2 W/m·K over the range of 100 – 300 K) [12], Bi_2Te_3/Sb_2Te_3 (0.25W/m·K at 300 K) [13], and Si/Ge (2.5W/m·K at 280 –320K), [11] even though the interface density of the MCT SL is ~1/10 that of these SLs.

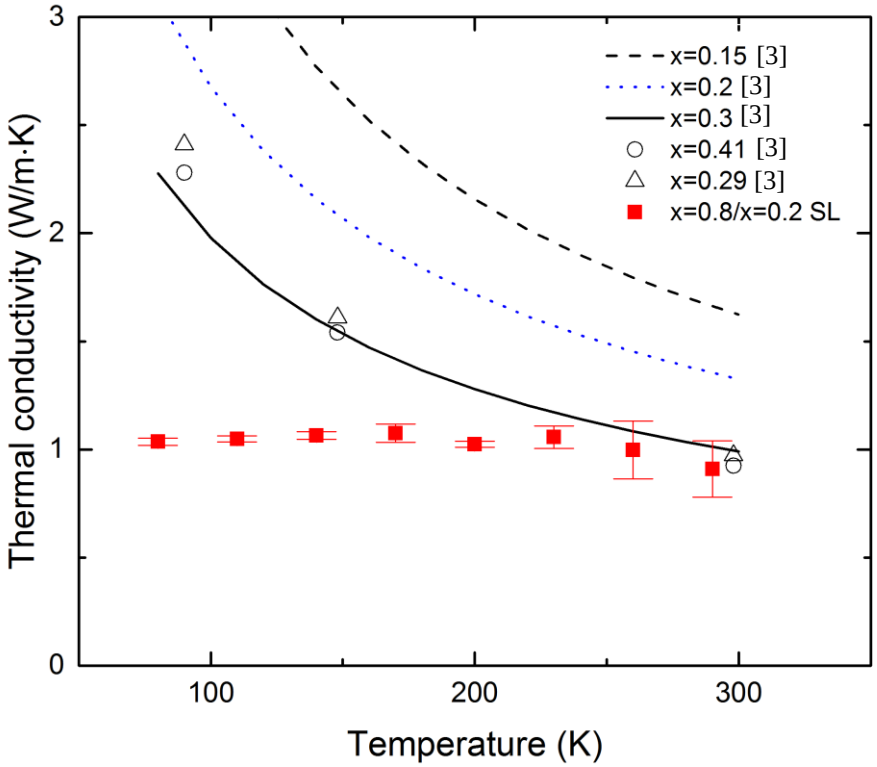

Figure 2.5 Measured temperature-dependent cross-plane thermal conductivities (■) of HgCdTe SL and literature values for bulk alloys [3]. Lines are from models and points are measured data.

Note that the flat temperature profile is not indicative of a spurious contribution of thermal boundary resistance (TBR) between the SL layer and the substrate, since the differential technique removes the common contributions of TBR for the two samples. Furthermore, the temperature-dependent change in TBR need to be approximately 4×10^{-7} ~ 8×10^{-7} m^2K/W to account for the flat temperature profile whereas typical TBRs of silicon substrate based-interfaces are on the order of 10^{-9} m^2K/W for both weak and strong coupling cases. [14] [15] [16] Because the MCT SL has a large period length and very little lattice mismatch, its low measured thermal conductivity is not likely due to phonon localization [13], or the presence of a high dislocation density. [12] [17] A high dislocation density would be expected to lead to a reduced electrical conductivity, which is not observed, also suggests the samples are in good condition.

Both diffusive mismatch model (DMM) and acoustic mismatch model (AMM) are extensively used in determining TBR. [18] [19] Here, we use the simple expressions of the TBR limits given by these models to estimate the thermal resistance of a single interface within the SL along the growth direction. For interfacial phonon scattering that is completely diffuse, DMM [19] predicts a boundary resistance per unit area of

$$R_{\mathrm{BD}} = 2\frac{(1+r_{12})(1+r_{21})-t_{12}t_{21}}{C_{\mathrm{v1}}v_1 t_{12}}, \qquad (2.2.1)$$

where subscripts 1 and 2 are the material properties on either side of the interface, C_{v} is the volumetric specific heat, and v is the sound velocity. We calculate the reflectivity and transmissivity at the interface from $t_{12} = C_{\mathrm{v1}}v_2/[C_{\mathrm{v1}}v_1+C_{\mathrm{v2}}v_2]$ and $r_{12} = 1 - t_{12}$.

For interfacial phonon scattering that is completely specular, AMM [18] predicts a boundary resistance per unit area of

$$R_{\mathrm{BD}} = \left[\frac{\pi^2 k_B^4}{15\hbar^3} \left(v^{-2} \Gamma \right) \right]^{-1} T^{-3}, \tag{2.2.2}$$

where the energy transmission probability Γ is given by $2Z_2Z_1/(Z_1+Z_2)^2$ and the thermal impedance Z_i is given by density times sound velocity $\rho_i v_i$.

The total thermal resistance is then the sum of the resistances of each layer and the boundary resistances. Using $C_{v\_Hg0.75Cd0.25Te}$ = 29 J/mol·K, $C_{v\_Hg0.2Cd0.8Te}$= 27 J/mol·K, and $v = (C_{11}/\rho)^{1/2}$ (where the elastic stiffness constant C_{11} is 56GPa) [3], the calculated diffuse and acoustic mismatch limits are 1.28 W/mK and 1.42 W/m·K, respectively, at room temperature. The fact that both are higher than the value derived from the measurement above, which is 0.91 W/m·K, suggests the possibility that other mechanisms are responsible for the measured low thermal conductivity.

The literature has found reduced velocity in SLs due to folding of the phonon branches in the first Brillouin zone. [20] [21] Since the times that the phonon branches fold are proportional to the period length, we expect that the folding effect has an important role in long-period MCT SLs, compensating the low interface resistance. Therefore, we use the elastic continuum model developed by Rytov to calculate the dispersion curves of the acoustic phonons. The method has been well applied for folded acoustic phonons in quantum well SLs [22], also explains the acoustic phonon features in Ge/Si quantum dot SLs [23] and InAs/GaAs quantum dot SLs [24].

The equation of motion for a crystal with cubic symmetry is given by [25]

$$\rho \frac{\partial^2 u_i}{\partial t^2} = C_{11} \frac{\partial^2 u_i}{\partial x_i^2} + C_{44} \left(\frac{\partial^2 u_i}{\partial x_j^2} + \frac{\partial^2 u_i}{\partial x_k^2} \right) + \left(C_{44} + C_{12} \right) \left(\frac{\partial^2 u_j}{\partial x_i \partial x_j} + \frac{\partial^2 u_k}{\partial x_i \partial x_k} \right), \tag{2.2.3}$$

where x_i is the i-th component of Cartesian coordinates, u_i is the i-th Cartesian component of the displacement, and C_{11}, C_{44}, and C_{12} are the three non-zero elements

of the stiffness tensor.

We are interested in longitudinal waves propagating in the cross-plane direction (*z* direction). In this geometry, the right side of Eq (2.2.3) contains only the first term. Moreover, since the material properties are constant in each layer, the motion is described by the piece-wise constant wave equation

$$\rho_j \frac{\partial^2 u_j}{\partial t^2} = C_j \frac{\partial^2 u_j}{\partial z^2}, \tag{2.2.4}$$

where the index j = 1, 2 refers to the quantities in layer 1 or 2, respectively. Eq. (2.2.4) is a homogeneous wave equation with constant coefficients, i.e., for a given frequency ω, the waves in each layer are combinations of plane waves with wavevectors $\pm q_{1,2} = \pm\omega/v_{1,2}$, where v is the corresponding speed of sound. We match the solutions at the interfaces between layers by requiring the continuity of the stress and the displacement

$$\begin{aligned} C_1 \frac{\partial u_1}{\partial z}\Big|_{\text{interface}} &= C_2 \frac{\partial u_2}{\partial z}\Big|_{\text{interface}} \\ u_1\big|_{\text{interface}} &= u_2\big|_{\text{interface}} \end{aligned}. \tag{2.2.5}$$

By these two equations together with Bloch's theorem to relate the waves in adjacent layers, Rytov's model [22] gives the dispersion relations

$$\begin{aligned} &\cos\left[q\left(t_1+t_2\right)\right] = \\ &\cos\left(\frac{\omega t_1}{v_1}\right)\cos\left(\frac{\omega t_2}{v_2}\right) - \frac{1}{2}\left(\frac{\rho_2 v_2}{\rho_1 v_1} + \frac{\rho_1 v_1}{\rho_2 v_2}\right)\sin\left(\frac{\omega t_1}{v_1}\right)\sin\left(\frac{\omega t_2}{v_2}\right), \end{aligned} \tag{2.2.6}$$

where t is the layer thickness. We numerically solve Eq. (2.2.6) and the dispersion relation for longitudinal phonons is shown in Fig. 2.6 (a). We derive the phonon group velocity $v_g = \partial\omega/\partial q$ from the dispersion relation and plot as shown in Fig. 2.6 (b). Note that the phonon group velocity in the MCT SL is significantly reduced with respect to that of bulk CdTe or HgTe [26] and is only approximately half of its bulk

value over a wide range of frequencies. Previous work has correlated reductions in SL thermal conductivity with reductions in phonon group velocity due to phonon folding. [20] The phonon group velocity of a 10×10 GaAs/AlAs SL is only 20% of its bulk value and account for a reduction of thermal conductivity by a factor 3. [20]

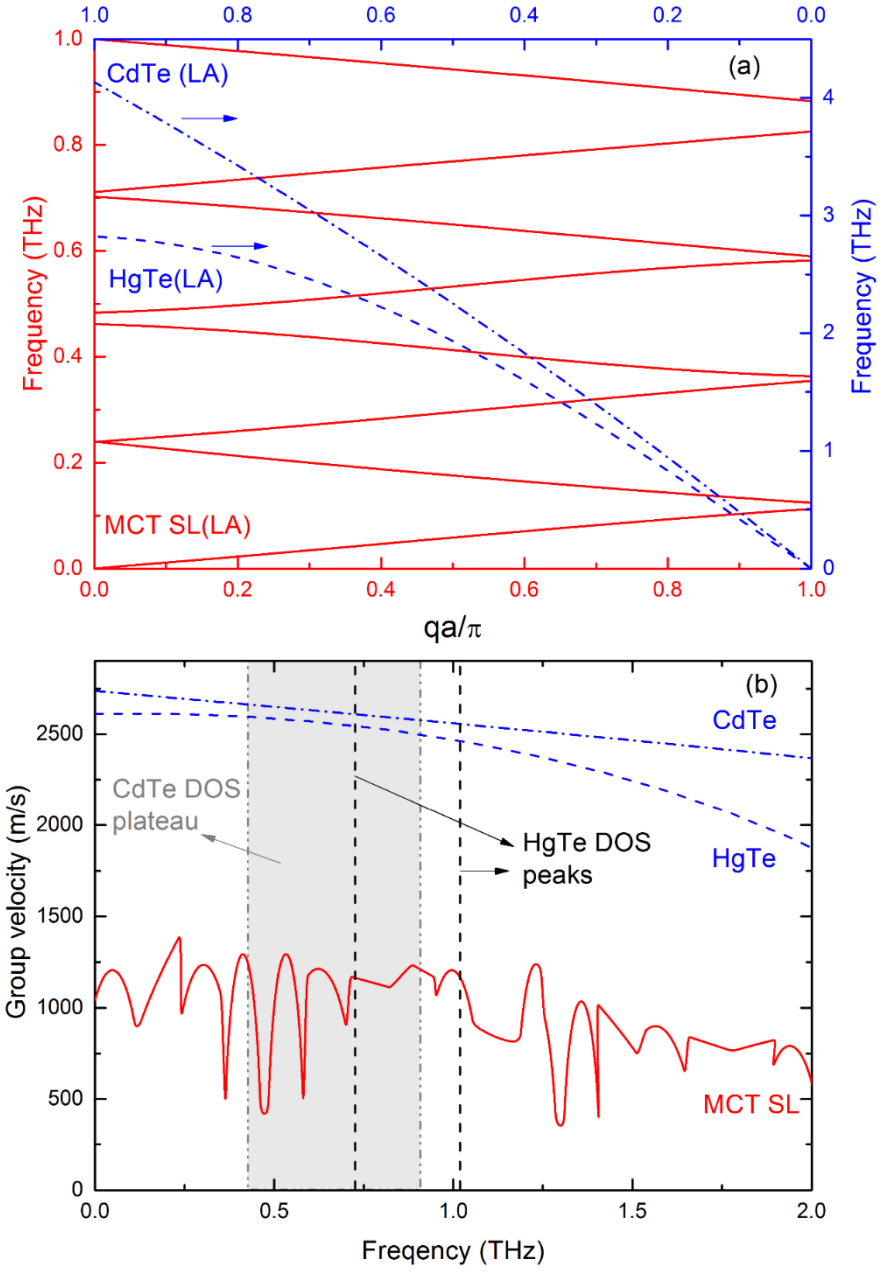

Figure 2.6 (a) Phonon dispersion curves of bulk CdTe [26], HgTe [26], and MCT SL. For CdTe and HgTe, "a" is the lattice constant, and for MCT SL, "a" is the period length. (b) Phonon group velocity versus frequency derived from the dispersion curves; the region where phonon density of states (DOS) of bulk MCT is high [26] are also indicated.

The reduced temperature dependence in the measured SL thermal conductivity versus bulk MCTis consistent with previous studies of other SL and bulk materials as summarized in Fig. 2.7. [27] [28] [29] The phonon mean free path (l_{mfp}) of bulk MCT is estimated to be 33nm at 300K and 85nm at 100K, through $l_{mfp} = \beta l_{Debye}$, where l_{Debye} is the mean free path based on the sound velocity and total specific heat (Debye model) and $\beta = 6$ is a factor that accounts for the contributions of optical phonons. [30] For the long-period SL studied here, the period length is comparable to the bulk l_{mfp} at room temperature and it is much smaller at low temperatures. We suggest that interface scattering may significantly reduce l_{mfp} (and hence thermal conductivity) at low temperatures and reduce the overall dependence of thermal conductivity on temperature.

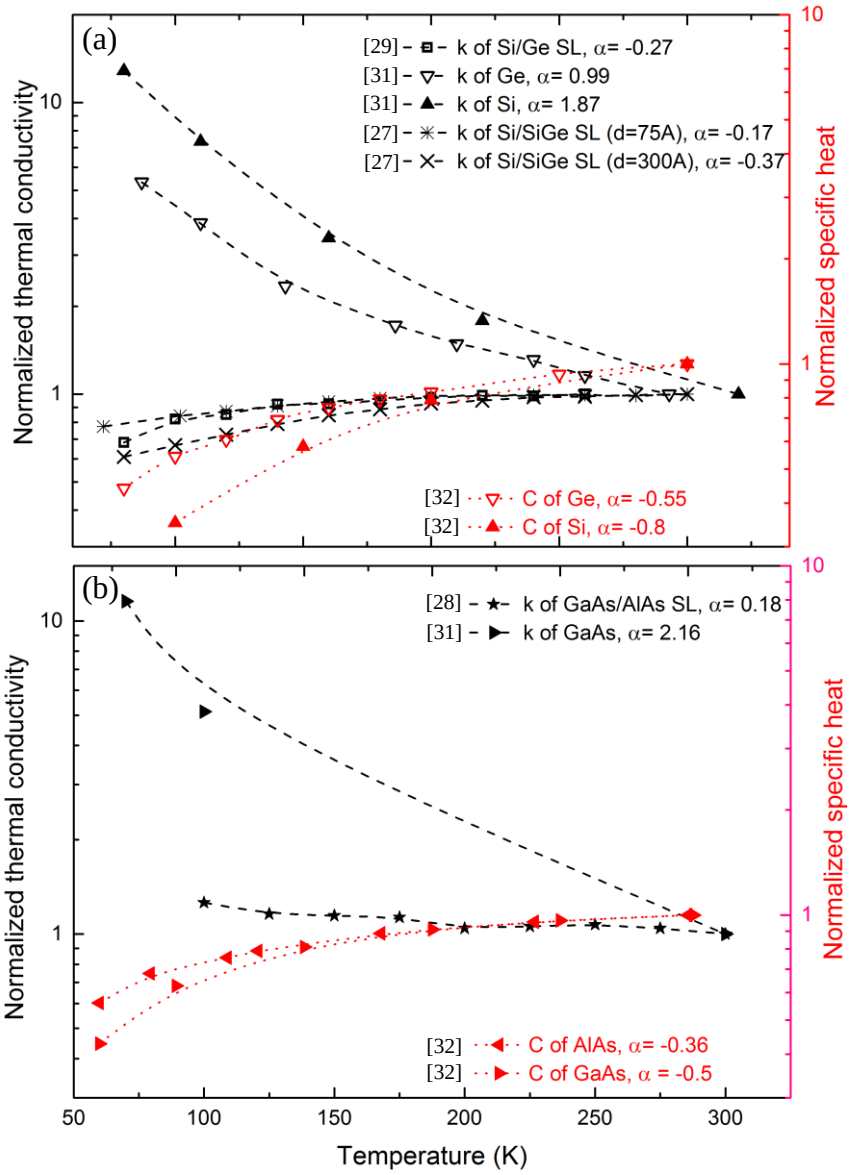

Figure 2.7 Normalized thermal conductivities ($k' = k/k_{300K}$) and specific heats ($C' = C/C_{300K}$) of SLs and corresponding bulk materials. [27] [28] [29] [31] [32] α is the exponential factor (from a $1/T^{\alpha}$ relationship) and d is the SL period length.

Furthermore, diffusive phonon transport resulting from scattering at SL interfaces has been proposed as a reason for the reduced temperature dependence of thermal conductivity observed in SLs. [33] [30] Diffuse contributions to thermal transport were modeled using a Kubo-Greenwood-type formula that included both a propagating contribution ($C \times v^2 \times \tau$, where C is the phonon specific heat, v is the phonon group velocity, and τ is the phonon relaxation time) and a diffuse contribution ($C \times \Xi$, where Ξ is the mode diffusivity). [34] [35] Typically, Ξ is a

temperature-independent intrinsic property of the mode. As suggested in Fig. 2.7, the temperature dependences of the propagating and diffuse terms (the first related to bulk thermal conductivity and the second related to specific heat) usually have opposite trends over our temperature range of interest, and the exponential factor α for the SL thermal conductivity ($\kappa \sim 1/T^{\alpha}$) lies between the α of bulk thermal conductivity and the α of specific heat. For the MCT SL components ($Hg_{0.8}Cd_{0.2}Te$ and $Hg_{0.2}Cd_{0.8}Te$), however, the specific heat is nearly constant across the temperature range of interest. Therefore, we expect that the contributions of diffusive phonon transport to thermal conductivity in the MCT SLs are relative temperature-independent. We plot the fitting curves of the specific heat of MCT based on the experimental data as shown in Fig. 2.8. [3]

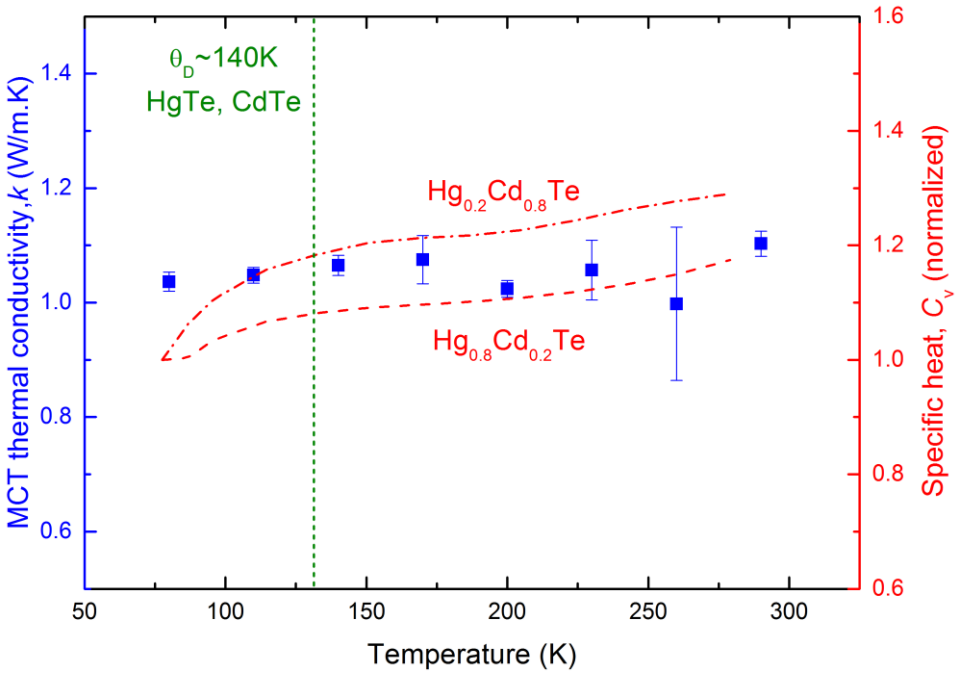

Figure 2.8 Specific heats of bulk forms of MCT SL components versus temperature, [3] Debye temperature of HgTe and CdTe, [3] and measured MCT SL thermal conductivity.

The measured Seebeck coefficient for the MCT SL in the cross-plane direction is shown in Fig. 2.9. Note that the observed gradual rise in the Seebeck coefficient with increasing temperature is typical for SLs in this temperature range and agrees with

simulations of the MCT SLs. [2] The magnitude of the Seebeck coefficient is also similar to other SL systems, e.g., InGaAs/ InAlAs SLs. [36] The measured electrical resistivity of the MCT SL is shown in Fig. 2.9. Due to the contact resistance between measuring probe and contact pads, the relative error is large. The temperature dependence of the cross-plane electrical conductivity in the SL follows the trend for a lightly doped semiconductor over this temperature range, i.e., the electrical conductivity declines with decreasing temperature. The cross-plane electrical resistance, which is similar to that of the corresponding alloy value ($Hg_{0.78}Cd_{0.22}Te$, 0.016~0.1 ohm·cm), [37] and to the in-plane electrical conductivity in other MCT SLs and thin films as shown in Fig. 2.10 [8] [38] [39] [40], suggests that the SLs do not have significantly increased defect density relative to other MCT SLs and thin films.

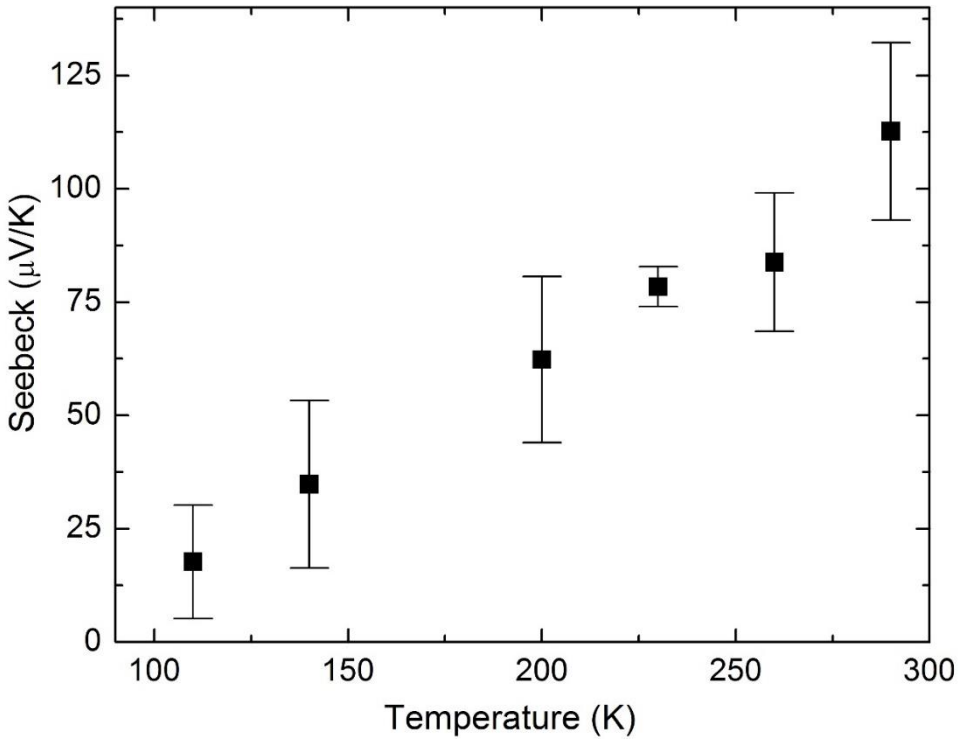

Figure 2.9 Measured Seebeck coefficient of MCT SLs versus temperature.

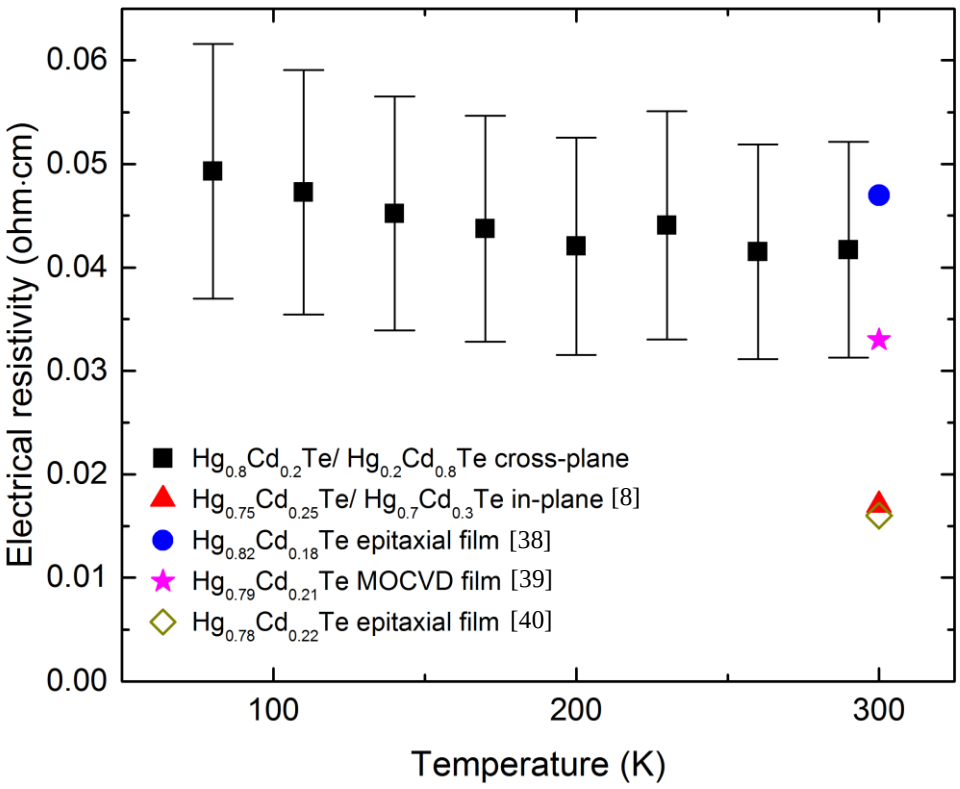

Figure 2.10. Electrical resistivity of MCT SLs and films versus temperature. [8] [38] [39] [40]

2.3 Summary

The cross-plane thermal conductivity, electrical conductivity, and Seebeck coefficient of long-period MCT SLs from 100K to 300K were measured. The thermal conductivity was lower than the alloy limit and exhibited little temperature dependence. In contrast to small-period SLs, the thermal conductivity was mostly reduced by decreased phonon group velocity due to the folding effect. The Seebeck coefficient and the electrical conductivity were reasonable, given the doping concentration.

[1] R. J. Radtke, H. Ehrenreich and C. H. Grein, "Multilayer thermoelectric refrigeration in $Hg_{1-x}Cd_xTe/Hg_{1-x}Cd_xTe$ superlattices," *J. Appl. Phys.*, vol. 86, p. 3195, 1999.

[2] D. Vashaee and A. Shakouri, "HgCdTe superlattices for solid-state cryogenic refrigeration," *Appl. Phys. Lett.,* vol. 88, p. 132110, 2006.

[3] P. Capper and J. W. Garland, Mercury Cadmium Telluride: growth, properties and applications, Wiley, 2011.

[4] R. Venkatasubramanian, E. Siivola, T. Colpitts and B. O'Quinn, "Thin-film thermoelectric devices with high room-temperature figures of merit," *Nature,* vol. 413, p. 597, 2001.

[5] G. J. Snyder, J. P. Fleurial, T. Caillat, R. Yang and G. Chen, "Supercooling of Peltier cooler using a current pulse," *J. Appl. Phys.*, vol. 92, p. 1564, 2002.

[6] G. J. Snyder, M. Soto, R. Alley, D. Koester and B. Conner, "Hot spot cooling using embedded thermoelectric coolers," in *IEEE 26nd Annual, Semiconductor thermal measurement and management symposium*, 2006.

[7] T. M. Tritt, Recent trends in thermoelectric materials research III, Academic Press, 2001.

[8] S. Velicu, C. H. Grein, J. Zhao, Y. Chang, S. Y. An, A. Yadav, K. Pipe and W. Clark, "Thermoelectric characteristics in MBE-grown HgCdTe-based superlattices," *J. Electro. Mater.,* vol. 37, p. 1504, 2008.

[9] D. G. Cahill, "Thermal conductivity measurement from 30 to 750K: the 3w method," *Rev. Sci. Instrum.,* vol. 61, p. 802, 1990.

[10] T. Borca-Tasciuc, A. R. Kumar and G. Chen, "Data reduction in 3w method for thin-film thermal conductivity determination," *Rev. Sci. Instrum.,* vol. 72, p. 2139, 2001.

[11] B. Yang, J. L. Liu, K. L. Wang and G. Chen, "Simultaneous measurements of Seebeck coefficient and thermal conductivity across superlattice," *Appl. Phys. Lett.,* vol. 80, p. 1758, 2002.

[12] D. W. Song, W. L. Liu, T. Zeng, T. Borca-Tasciuc, G. Chen, J. C. Caylor and T. D. Sands, "Thermal conductivity of skutterudite thin films and superlattices," *Appl. Phys. Lett.,* vol. 77, p. 3854, 2000.

[13] R. Venkatasubramanian, "Lattice thermal conductivity reduction and phonon localizationlike behavior in superlattice structures," *Phys. Rev. B,* vol. 61, p. 3091, 2000.

[14] J. Chen, G. Zhang and B. Li, "Thermal contact resistance across nanoscale silicon dioxide and silicon interface," *J. Appl. Phys.*, vol. 112, p. 064319, 2012.

[15] E. S. Landry and A. J. H. McGaughey, "Thermal boundary resistance predictions from molecular dynamics simulations and theoretical calculations," *Phys. Rev. B,* vol. 80, p. 165304, 2009.

[16] R. Cheaito, J. T. Gaskins, M. E. Caplan, B. R. Donovan, B. M. Foley, A. Giri, J. C. Duda, C. J. Szwejkowski, C. Constantin, H. J. Brown-Shaklee, J. F. Ihlefeld and P. E. Hopkins, "Thermal boundary conductance accumulation and interfacial phonon transmission: Measurements and theory," *Phys. Rev. B,* vol. 91, p. 035432, 2015.

[17] S. M. Lee, D. G. Cahill and R. Venkatasubramanian, "Thermal conductivity of Si–Ge superlattices," *App. Phys. Lett.*, vol. 70, p. 2957, 1997.

[18] E. T. Swartz and R. O. Pohl, "Thermal boundary resistance," *Rev. Modern Phys.*, vol. 61, p. 605, 1989.

[19] G. Chen and M. Neagu, "Thermal conductivity and heat transfer in superlattices," *Appl. Phys. Lett.*, vol. 71, p. 2761, 1997.

[20] S. Tamura, Y. Tanaka and H. J. Maris, "Phonon group velocity and thermal conduction in superlattices," *Phys. Rev. B,* vol. 60, p. 2627, 1999.

[21] C. Colvard, T. A. Gant and M. V. Klein, "Folded acoustic and quantized optic phonons in (GaAl)As superlattices," *Phys. Rev. B,* vol. 31, p. 2080, 1985.

[22] B. Jusserand, D. Paquet, F. Mollot, F. Alexandre and G. Le Roux, "Influence of the supercell structure on the folded acoustical Raman line intensities in superlattices," *Phys. Rev. B,* vol. 35, p. 2808, 1987.

[23] A. Milekhin, A. I. Nikiforov, O. P. Pchelyakov, S. Schulze and D. R. T. Zahn, "Self-selective Raman scattering in self-assembled Ge/Si quantum dot superlattices," *Nanotechnology,* vol. 13, p. 55, 2002.

[24] D. A. Tenne, V. A. Haisler, A. K. Bakarov, A. K. Gutakovsky, D. R. T. Zahn and A. P. Shebanin, "Raman study of self-assembled Gaas and AlAs ilands embedded in InAs," *Phys. Rev. B,* vol. 61, p. 13785, 2000.

[25] C. Kittel, Introduction to solid state physics, New York: Wiley, 1996.

[26] D. Strauch, Landolt-Bornstein-Group III condensed matter Matter Vol. 44E, Springer, 2012.

[27] S. T. Huxtable, A. R. Abramson, C. L. Tien, A. Majumdar, C. LaBounty, X. F. Fan, G. Zeng, J. E. Bowers, A. Shakour and E. T. Croke, "Thermal conductivity of Si/SiGe and SiGe/SiGe superlattices," *Appl. Phys. Lett.*, vol. 80, p. 1737, 2002.

[28] W. S. Capinski, H. J. Maris, T. Rurf, T. Cardona, K. Ploog and D. S. Katzer, "Thermal-conductivity measurements of GaAs/AlAs superlattices using a picosecond optical pump-and-probe technique," *Phys. Rev. B,* vol. 59, p. 8105, 1999.

[29] W. L. Liu, T. Borca-Tasciuc, G. Chen, J. L. Liu and K. L. Wang, "Anisotropic

thermal conductivity of Ge quantum-dot and symmetrically strained Si/Ge superlattices," *J. Nanosci. Nanotech.,* vol. 1, p. 39, 2001.

[30] G. Chen, "Thermal conductivity and ballistic-phonon transport in the cross-plane direction of superlattices," *Phys. Rev. B,* vol. 57, p. 14958, 1998.

[31] I. Institute, "New semiconductor materials archive," [Online]. Available: http://www.ioffe.rssi.ru/SVA/NSM/.

[32] Palankovski, Simulation of heterojunction bipolar transistors, PhD thesis, 2001.

[33] P. Hyldgaard and G. D. Mahan, "Phonon superlattice transport," *Phys. Rev. B,* vol. 56, p. 10754, 1997.

[34] P. B. Allen and J. L. Feldman, "Thermal conductivity of disordered harmonic solids," *Phys. Rev. B,* vol. 48, p. 12581, 1993.

[35] D. Donadio and G. Galli, "Temperature Dependence of the Thermal Conductivity of Thin Silicon Nanowires," *Nano Lett.,* vol. 10, p. 847, 2010.

[36] D. Vashaee, Y. Zhang, A. Shakouri, G. Zeng and Y. J. Chiu, "Cross-plane Seebeck coefficient in superlattice structures in the miniband conduction regime," *Phys. Rev. B,* vol. 74, p. 195315, 2006.

[37] P. Moravec, R. Grill, J. Franc, R. Varghová, P. Hoschl and E. Belas, "Galvanomagnetic and thermoelectric properties of p-Hg1-xCdxTe," *Semicond. Sci. Technol.,* vol. 16, p. 7, 2001.

[38] V. V. Bogoboyashchyy, I. I. Izhnin, K. D. Mynbaev, M. Pociask and A. P. Vlasov, "Relaxation of electrical properties of n-type layers formed by ion milling in epitaxial HgCdTe doped with V-group acceptors," *Semicond. Sci. Technol.,* vol. 21, p. 1144, 2006.

[39] I. I. Izhnin, H. V. Savytskyy, O. I. Fitsych, J. Piotrowski and K. D. Mynbaev, "Electrical properties of HgCdTe films grown by MOCVD and doped with As," *Opto-Electron. Rev.,* vol. 21, p. 220, 2013.

[40] I. I. Izhnin, V. V. Bogoboyashchyy and F. F. Sizov, "Electrical characterisitics relaxation of ion milled MCT layers," in *Proceedings of SPIE Infrared and Photoelectronic imagers and detector devices*, Bellingham, WA, 2005.

Chapter 3

Thermoelectric Properties of SWNT-based Networks

3.0 Introduction

Carbon nanotube networks offer significant technological promise as a means to realize on a macroscopic size scale the excellent thermal, electrical, mechanical, and functionalization properties of nanotubes in general and single-walled carbon nanotubes (SWCNTs) in particular. In such networks, the properties of the junctions between nanotubes can critically determine the performance of the entire network. For thermal and electrical applications of uncoated SWCNT networks, nanotube junctions are the primary bottleneck for heat and charge transfer, since thermal and electrical conductivities are high within the SWCNTs themselves. [1] [2] [3] In addition to the intrinsic impedances of the individual junctions, collective effects (e.g., phonon interference) can arise due to the interconnected nature of the network and contribute to the total impedance; Green's functions calculations that include such effects have been used to study the large increases observed in junction impedance for SWCNT networks relative to that measured at the junction of two isolated (i.e., not within a network) SWCNTs. [1]

In this chapter, we present the temperature-dependent (100 K – 300 K) thermal, electrical, and thermoelectric properties of SWCNT aerogels with ultralow density ($\rho \approx 6.6$ kg m^{-3}). The aerogels are three-dimensional, isotropic networks of SWCNTs

held together by van der Waals interactions at the junctions between nanotubes. [4] [5] Their ultralow density leads to an interjunction spacing (mesh size) of 20 nm [6] which is much larger than previous SWCNT networks (mesh size ~2 nm) [1] in which these transport properties have been studied. This enables the transport properties of the junctions to be distinguished from those of the nanotubes themselves.

3.1 Measurement and Error Analysis

The four types of network are: pristine SWNT networks (ρ = 6.2, 6.6kg/m^3); graphitic- (Gr-) coated SWNT networks (ρ = 13.8, 15.4, 16.1kg/m^3); BN-coated SWNT networks (ρ = 17.2kg/m^3 with a weight percentage ratio of BN/SWNT = 0.5/0.53, ρ = 11.82kg/m^3 with a weight percentage ratio of BN/SWNT = 1.7/0.3, ρ = 529.1kg/m^3 with a weight percentage ratio of BN/SWNT = 24.6/1); and PEDOT:PSS-coated SWNT networks with a volume percentage ratio of PEDOT:PSS/SWNT = 62.7/7.7, 44.4/5.5, 26.7/3.3). The first three networks are ultralow density aerogels.

All the samples are synthesized by Islam Research Group in Carnegie Mellon University. Pristine samples are synthesized from SWNTs provided by SouthWest NanoTech with length $l \approx 1\mu$m and diameter $d \approx 0.93$nm using a critical point drying technique. The graphitic-coated SWNT networks are synthesized from the pristine ones by soaking the pristine gels in 0.5wt% PAN, and transfer the PAN coating to multilayered graphenes on SWNTs. High resolution transmission electron microscopy (HRTEM), Raman spectroscopy, and electron energy loss spectroscopy (EELS) confirm that the coated graphitic layers are highly crystalline. The BN-coated samples are synthesized by soaking the pristine gels into H_3BO_3 solution, and then heat it in a nitrogen atmosphere. HRTEM and Raman spectroscopy confirm the continuous highly crystalline BN at tube junctions. Note that both graphitic coating and BN

coating are known to improve the mechanical properties of SWNT networks. [4] [7] Details of the sample fabrication can be found in [4] [5] [7].

3.1.1 Measurement Setup

We use a comparative method to measure thermal conductivity which is standard for materials with low thermal conductivity. [8] A disc-shaped sample of radius R_S and thickness t_S is sandwiched between two stainless-steel discs (SS304), each having the same radius as the sample, and temperature dependent thermal conductivity that is previously measured (geometry of each type of sample is summarized in Table 3.1). Silver paste (DuPont 4929N) is applied to reduce the contact resistance between the networks and steel plates without permeating the samples. A heater is mounted on top of one steel plate and used to generate a heat current while the other plate is placed with cold finger of a cryostat, thereby realizing a standard heat flux measurement geometry. Measurements are conducted in vacuum ($<1\times10^{-7}$ Torr) to prevent parasitic convection. Two copper cylinders are mounted outside the cold finger as radiation shields. The temperature of the sample holder is controlled by a Lakeshore 340 temperature controller. Six thermocouples (TC1-TC6) are inserted into small-bore holes in the steel plates and affixed to the top and bottom of the samples and are used in separate measurements to determine: 1) the heat flux through the steel plates (TC5, TC6) and the temperature drop across the sample (TC3, TC4) when the heater is turned on, to derive the samples' thermal conductivity; 2) the temperature drop and induced thermal voltage (T3, T4) across the samples when the heater is turned on, to derive the Seebeck coefficients; and 3) the voltage drop across the samples (T3, T4) when the current source (I) is turned on, to derive the electrical conductivity. The experimental setup is shown in Fig. 3.1.

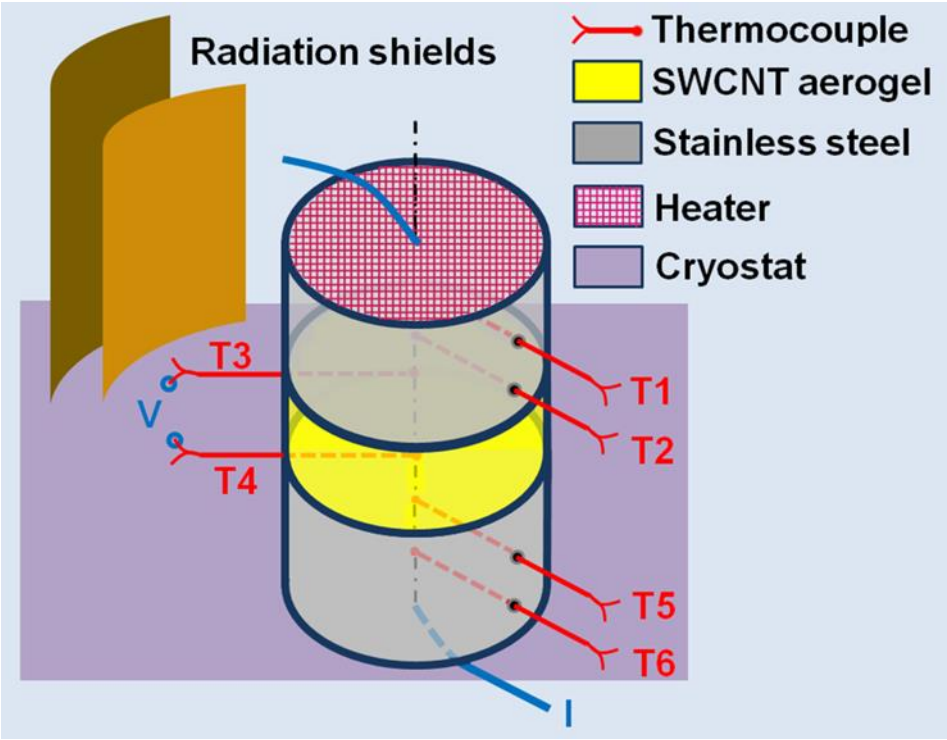

Figure 3.1 Experimental setup. The aerogel sample is sandwiched between two stainless steel plates so the heat flux can be measured. All measurements are performed in a vacuum to prevent parasitic convection. Two radiation shields are used to reduce parasitic radiation loss.

We derive the sample thermal conductivity (k) using the 1D Fourier law $k = Qt_s/(A_s(T_3-T_4))$, where t_s and A_s are the sample thickness and cross-sectional area, respectively, and Q is the heat flux through the sample. We estimate Q using the heat flux $A_b k_b(T_5-T_6)/t_b$ transferred through the bottom steel plate, where k_b is the steel plate thermal conductivity, and t_b is the distance between TC 5 and 6. There are three major sources of error (discussed in the chapter subsection) associated with Q: 1) uncertainty due to the sample's parasitic blackbody radiation losses to the environment (calculated to be less than 9.3%); 2) uncertainty due to the parasitic conduction losses through the thermocouples (calculated to be less than 0.1%); and 3) uncertainty in t_b due to the nonzero thermocouple diameter (calculated to be less than 10%). Direct calculation of the heat loss by comparison of the heat fluxes in the top and bottom steel plates, while having a larger uncertainty than the component

analysis above due to the collective uncertainties associated with a larger number of thermocouples, likewise suggested that the heat loss was small compared to Q. The uncertainty in t_s due to surface roughness is approximately 5%, and the uncertainties in both the temperature and voltage measurements are less than 0.01%. We estimate that the interfacial temperature drops at each end of the sample are less than 0.3% of the temperature drop across the pristine and Gr-coated samples. We calculate the fraction of Q carried by radiative heat transfer within the aerogel to be between 0.3% and 2.3% for the pristine sample and between 0.3% and 2.7% for the Gr-coated sample over the range of 100-300K. Accounting for these sources of uncertainty, we find a maximum error in the thermal conductivity of 19.1%. By using the same bottom steel plate for all measurements of pristine and Gr-coated samples, thus fixing t_b, the relative uncertainty in thermal conductivity between these two types of samples is less than 9.5%, and the relative uncertainty between the BN-coated and PEDOT:PSS-oated samples is similar.

Table 3.1 Geometry of samples and corresponding stainless steel discs

Samples	Sample radius (mm)	Sample thickness (mm)	Distance between TC5 and TC6 (mm)
Pristine	10	3	5
Gr-coated	10	3	Same SS disks as pristine case are used
BN coated	5	1~1.5	10
PEDOT:PSS coated	5	1	Same SS disks as BN-coated case are used

3.1.2 Blackbody Radiation Losses

While the samples are indeed relatively thin, the measured temperature drop across them is still large (up to 35K) due to the networks' ultralow density. We use a

custom MATLAB script to numerically calculate the radiation loss from sample to environment. For the sidewall radiation companied 1D conduction along *z* direction, the heat balance equation is given by

$$\frac{d^2T}{dz^2} = \frac{P_S t_S}{A_S k}\sigma_b \varepsilon \left(T^4 - T_e^4\right), \tag{3.1.1}$$

where P_S is the sample perimeter, T_e is the environment temperature (in our case, the cryogenic setting temperature), σ_b is the Stefan-Boltzmann constant, and $\varepsilon \approx 1$ is the sample emissivity (estimated from the data for the CNT array [9]). Three boundary conditions, two temperatures measured at the hot/cold ends of the sample, and the heat flux transferred through the sample at the cold end are given by

$$\begin{aligned} &T\big|_{z=0} = T_3, T\big|_{z=t_S} = T_4 \\ &\frac{dT}{dz}\Big|_{z=t_S} = A_b k_b \frac{T_5 - T_6}{t_b} \cdot \end{aligned} \tag{3.1.2}$$

For our initial inputs, we use *k* calculated from the 1D Fourier. Note that we can numerically calculate the temperature distribution backwards from the cold end temperature. Then, we compare the deduced hot end temperature T_3' to the measured value and adjust the thermal conductivity accordingly. The iteration continues until $|T_3' - T_3|/ T_3 < 10^{-4}$. Obtaining the correct temperature distribution allows us to calculate the radiation loss. Note that *k* calculated from the 1D Fourier law is a little smaller than *k* calculated by this method. The difference is less than 7.1% for the pristine and Gr-coated samples and less than 8.8% for the BN-and PEDOT:PSS-coated samples. Using the 1D Fourier law, however, is preferred for simplicity with acceptable accuracy.

3.1.3 Parasitic Conduction from Thermocouples to Environment

We find the parasitic conduction from the thermal couples to the environment by

calculating $Q_{conduction\_loss} = (k_{copper} + k_{cons})A_{TC}\Delta T/l_{TC}$ for thermal couples TC3, TC4, TC5, and TC6, where k_{copper} and k_{cons} are the thermal conductivity of copper and constantan, respectively, A_{TC} is the cross-section area of the thermal couple wires (diameter ~ 10μm), $l_{TC} \approx 14$cm is the length of thermocouple wires, and ΔT is the change in temperature from the sample to the environment.

3.1.4 Interface Thermal Resistance

Letting ΔT_{int} be the temperature drop at the sample/silver paste interface and ΔT_S be the temperature drop across the sample, the measured temperature drop is given by $2\Delta T_{int} + \Delta T_S$. The value range is 30-35K. For a SWNT/metal interface, the highest reported thermal boundary resistance (TBR) is 9.2mm^{2}K/W. [10] To account for the difference in volume fraction (ϕ) for the SWCNT array in [10] and that for our networks, we use the relation $R_{int,i} = R_{int} \times \phi$, where $R_{int,i}$ is the TBR of an interface between a metal and an individual SWCNT. This yields 36.5mm^{2}K/W for an aligned SWCNT array with the same volume concentration as the concentration pristine/Gr-coated samples. Using the measured thermal conductivity, we find $2\Delta T_S/(2\Delta T_{int} + \Delta T_S) = 1.2\times10^{-3}$ and 4.8×10^{-4} for an aligned SWNT array with the volume concentration of the pristine/ Gr-coated samples, respectively.

Next, we consider the effect of the SWNT alignment on TBR. For an isotropic 3D network of rods (here, SWNTs), the average number of SWNTs crossing a plane can be calculated as [11]:

$$\langle N_S \rangle = \frac{A_S}{lr}\frac{\bar{n}_V}{2}\left(1+4\frac{r}{l}\right); \bar{n}_V = n_V l^2 r \,, \qquad (3.1.3)$$

where r is the tube radius, $n_V = \phi/(\delta dl)$ is the volume number density of the SWNTs, $\overline{n_V}$ is its dimensionless parameter, and $\delta = 3.4$ Å is the graphite intersheet spacing. For an aligned SWCNT array, we calculate the average number of SWNTs at the top surface as $N_A = A_S\phi/(\pi\delta d)$. The ratio N_S/N_A is $(1 + 4dl)/2$, which is very close to 0.5

for our SWNT networks. Based on the results of the aligned arrays above, we find $2\Delta T_S/ (2\Delta T_{int} + \Delta T_S) = 2.4\times10^{-3}$ and 9.6×10^{-4} for an isotropic SWNT array corresponding to the pristine/ Gr-coated samples, respectively.

There is little information about TBRs of BN-metal and PEDOT:PSS-metal interfaces. Thus, we omit discussion of the errors caused by TBR in BN-coated and PEDOT:PSS-coated systems.

3.1.5 Radiation within SWNT Networks

SWNT networks have optical properties similar to carbon aerogels, including optical thickness. [12] [13] Hence, phonon diffusive theory is appropriate for calculating radiation transfer within SWCNT networks. [13] We express the effective radiative conductivity of the pristine and Gr-coated samples by $k_r = 16n^2\sigma_b T_S^3/ 3\rho_b e_{temp}$, [13] [14] where the refractive index n can be calculated using the Clausius-Mossotti formula, $(n^2 - 1)/ (n^2 - 2) = \phi(n_{carbon}^2 - 1)/ (n_{carbon}^2 + 2) + (1-\phi)(n_{vacuum}^2 - 1)/ (n_{vacuum}^2 + 2)$, for which $n_{carbon} = 2$ is the solid backbone refractive index, [15] and $n_{vacuum} = 1$ is the pore refractive index. We derive the temperature dependent specific extinction coefficient e_{temp} from the frequency dependent specific extinction coefficient using the Rosseland weighting function [13]; the range is between 550m^2/kg and 800m^2/kg over the temperature range of 100-300K. Again, we omit discussion within the BN coated and PEDOT:PSS coated networks, due to the absence of information about optical properties

3.2 Pristine and Gr-coated SWNT Networks

The thermal conductivities measured for the pristine and graphitic SWCNT aerogels at room temperature are shown in Fig. 3.2. Both aerogels have thermal conductivities similar to conventional carbon aerogels (CAs) of much higher density. [14] [16] [17] At room temperature, the average k/ρ is 85.9 W cm^2 kg^{-1} K^{-1} for the

as-grown aerogels and 14.6 W cm^2 kg^{-1} K^{-1} for the Gr-coated aerogels are much higher than in CAs (typically, ~5 W cm^2 kg^{-1} K^{-1}). The temperature dependence of the thermal conductivity measured for the SWCNT aerogels primarily in the range of 100-300K is shown in fig. 3.3. The thermal conductivities of the as-grown aerogels strictly increase with temperature, similar to a single isolated (non-network) SWCNT-SWCNT junction over the same temperature range. [2] While the Gr-coated aerogels are more than twice as dense, their thermal conductivities are approximately half that of the as-grown sample, and exhibit a plateau region. Similar plateaus in thermal conductivity observed in amorphous materials (including aerogels) due to a strong Rayleigh scattering of phonons from local variations of density or bond length, typically occur in such materials at lower temperatures of ~30K. [18] [19]

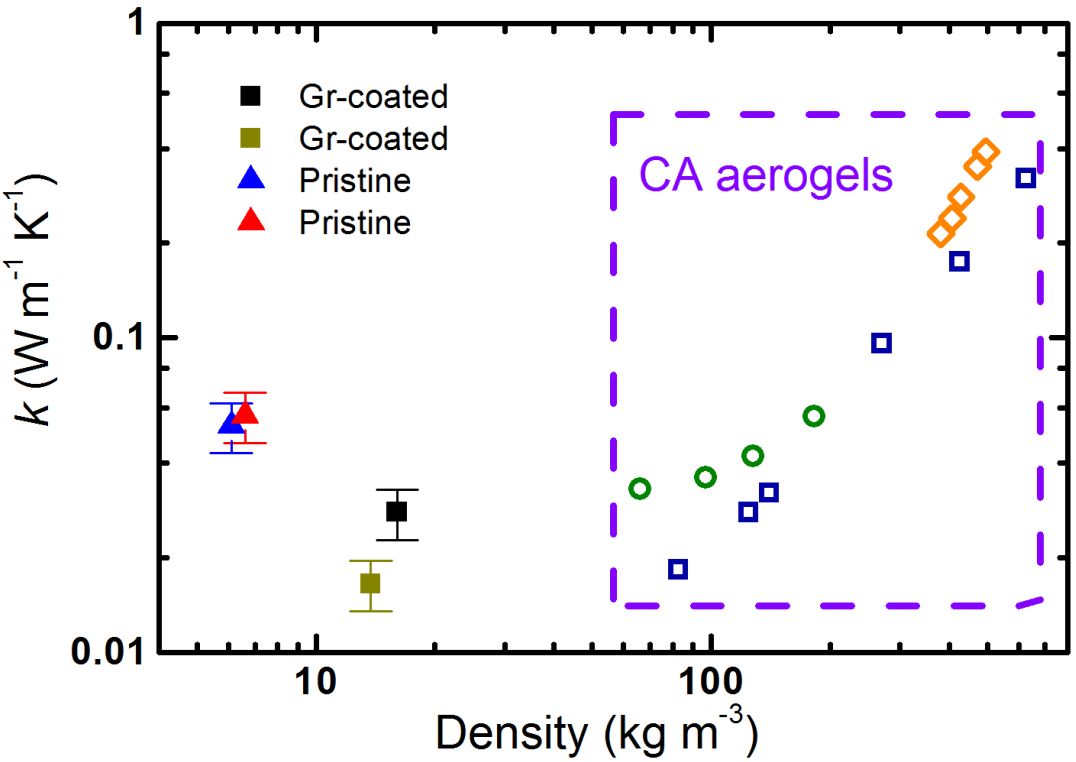

Figure 3.2 Thermal conductivities of SWCNT aerogels and carbon aerogels (CAs) with various densities at room temperature. ▲(red and blue): as-grown, ■(black and brown): Gr-coated, □,○,◇: CAs. [14] [16] [17]

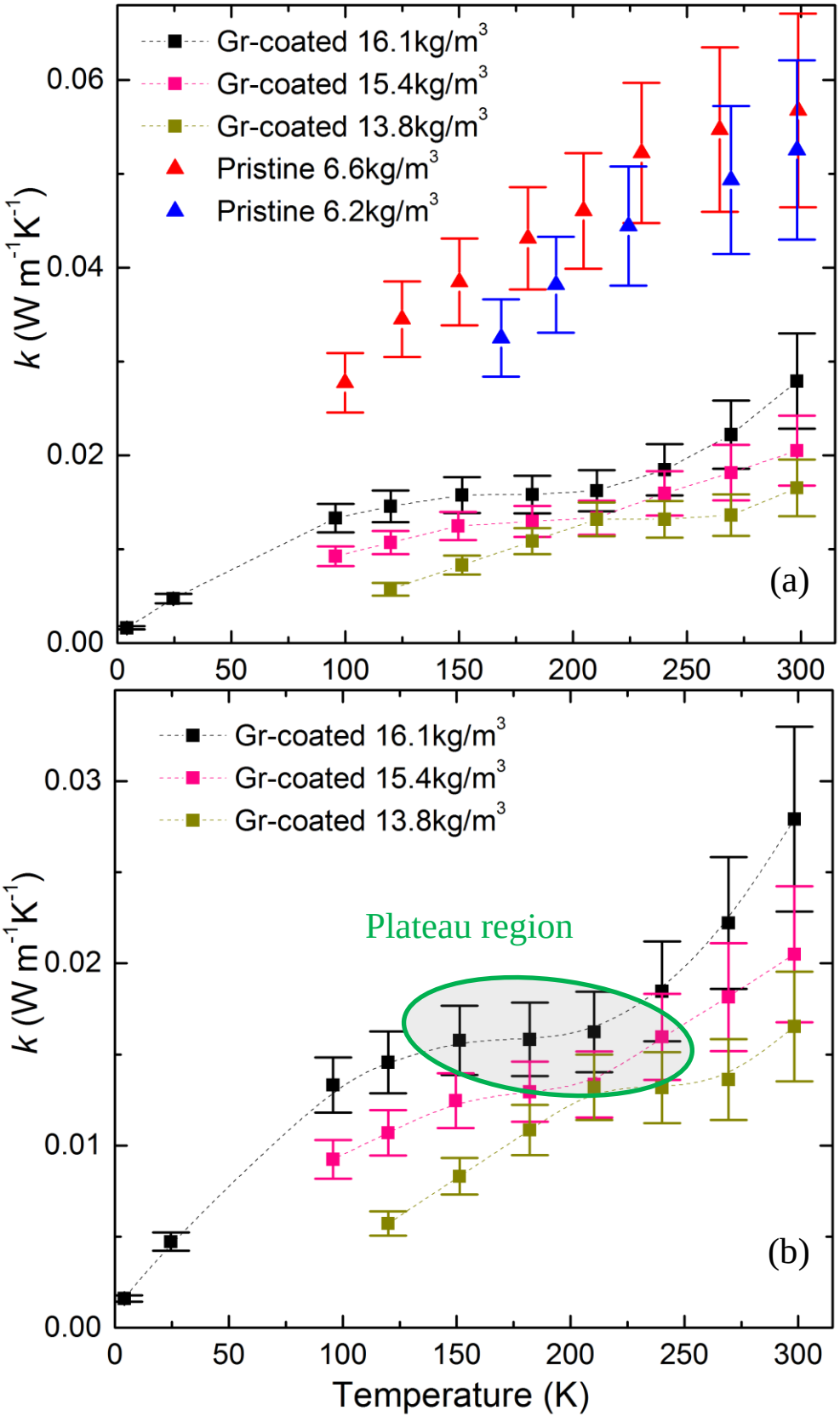

Figure 3.3 Thermal conductivity of pristine and Gr-coated SWNT networks as a function of temperature. (b), which is an enlargement of (a) shows the size of the plateau region.

To analyze the thermal performance of the two types of aerogels, we first express the aerogel thermal resistance as $R = R_{NT} + R_{junc}$, where R_{NT} is due to transport within the SWCNTs, and R_{junc} is due to transport at the junctions between the SWCNTs. We calculate R_{NT} by considering a structure having the same radius, thickness, and density as the aerogel sample and containing n_2 layers of SWCNTs (each having n_1 SWCNTs all of diameter d and length l) that perfectly align in the direction of the temperature gradient. R_{NT} is then given by $R_{SWCNT} \times n_2/n_1$, where R_{SWCNT} is the thermal resistance of a single SWCNT as shown in Fig. 3.4 (b). Because the phonon mean free path (l_{mfp}) of an as-grown 1-nm-diameter SWCNT is larger than 750 nm for temperatures below 300K, [20] we assume ballistic heat transfer within the SWCNTs in the as-grown aerogel and set $l_{mfp} = l$. Applying the thermal conductivity relation $k = Cvl_{mfp}/3$, [21] we express R_{SWCNT} of the as-grown aerogels as $3/\pi d\delta C v_B$, where C is the SWCNT specific heat (taken to vary from 153 to 641 J kg^{-1} K^{-1} over the range of 100-300K based on the data for an isolated uncoated (10, 10) SWCNT), [22] and v_B is the ballistic phonon group velocity independent of nanotube length and calculated as ~1.5×10^7 m s^{-1} based on $v_B = 3k/Cl_{mfp}$ and the measurement data for an as-grown 1-nm-diameter SWCNT.[20] The above calculations predict a contribution of R_{NT} to the total measured SWCNT aerogel thermal resistance of around 0.3~0.8%, Similar to the other SWCNT networks, junction resistances dominate the resistance of the as-grown sample . [1] [23]

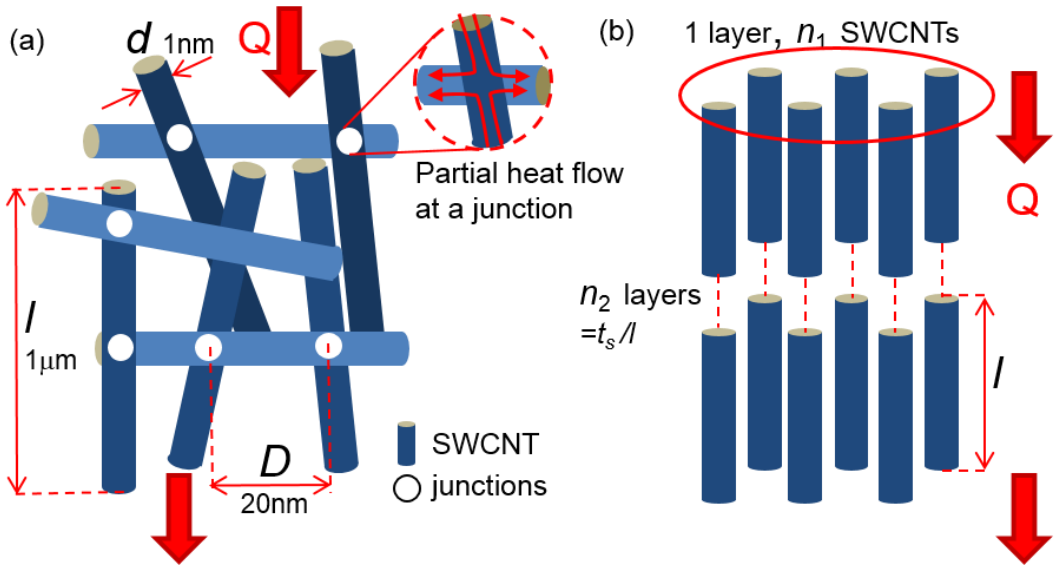

Figure 3.4 (a) Length parameters defining SWNT networks: l = nanotube length, d = nanotube diameter, D ~ mesh size. Heat current flows through the connected nanotubes need to overcome the thermal resistance of the tubes and junctions. (b) Equivalent SWNT arrays to characterize the contribution of the nanotube resistances.

Using an excluded volume approach, we derive the total contribution of the junctions to the aerogel thermal conductivity for a network of junctions each having thermal conductance G. [11] Assuming nanotube has infinitely large thermal conductivity, as a sequence, every tube in the sample is characterized by a single value of temperature T_i and the heat flux at contact between tube i and j is equal to $Q_{ij} = G(T_i - T_j)$, where the inter-tube junction conductance, G, is assumed to be the same for all junctions. The heat flux through a cross section of the systems (asssumed at the plane $z = 0$, and the heat flux follows the positive z direction) as $Q_z = -\Sigma\Sigma\delta_{ij(+)}Q_{ij}$, where $\delta_{ij(+)}=1$ if tube i intersects axis $z = 0$ and the point of contact between tube i and j is above crosssection, otherwise $\delta_{ij(+)}=0$. The ensmeble averaged heat flux is given by

$$\langle Q_z \rangle = G\left\langle \Sigma\Sigma\delta_{ij(+)}\left(T_i - T_j\right)\right\rangle = -G\langle N_z\rangle\langle N_J\rangle\left\langle \Delta T_{(+)}\right\rangle/2\,, \qquad (3.2.1)$$

where is $\langle N_z \rangle$ is the average number of tubes crossing the plane $z = 0$, $\langle N_J \rangle$ is the

average number of junctions for tube, $\langle \Delta T_{(+)} \rangle = \nabla T_z \langle \Delta z_{(+)} \rangle$ is the averaged temperature difference in junctions between tubes *i* and *j* with $\delta_{ij(+)}=1$, and $\langle \Delta z_{(+)} \rangle$ is the averaged difference between the *z* coordinates of the centers of the interacting tubes, which satisfy the condition $\delta_{ij(+)}=1$. For a 3D system, the parameters are given by [11]

$$\begin{aligned}
\langle N_z \rangle &= \frac{L^2}{lr}\frac{\bar{n}_V}{2}\left(1+4\bar{r}\right) \\
\langle N_J \rangle &= \pi \bar{n}_V \left(1+8\bar{r}+\left(32/3\right)\bar{r}^2\right) \\
\left\langle \Delta z_{(+)} \right\rangle &= \frac{l}{9}\frac{1+16\bar{r}+80\bar{r}^2+192\bar{r}^3+153.6\bar{r}^4}{\left(1+4\bar{r}\right)\left(1+8\bar{r}+\left(32/3\right)\bar{r}^2\right)}
\end{aligned} \quad , \tag{3.2.2}$$

where *L* is the system size, *r* is the tube radius, $\bar{r} = r/l$ is the tube aspect ratio, n_V is the volume number density of SWNTs, and $\overline{n_V} = n_V l^2 r$ is the system's dimensionless parameter. The junction thermal conductivity derived from Eq. (3.2.1) and (3.2.2) is given by

$$k_{\text{junc}} = \frac{G}{r}\frac{\pi \bar{n}_V^2}{36}\left(1+16\bar{r}+80\bar{r}^2+192\bar{r}^3+153.6\bar{r}^4\right). \tag{3.2.3}$$

Since the tube aspect ratio in our aerogels is very small, we only need the first term on the right side of Eq. (3.2.3). Realizing $n_v = \rho/(\pi \rho_{\text{graphene}} l d)$, where $\rho_{\text{graphene}} = 7.6\times10^{-7}\text{kg/m}^2$ is the surface mass density of graphene, the thermal conductivity determined by junctions is given by Eq. (3.2.4). Note that Eq. (3.2.4) yields electrical and thermal conductivities proportional to ρ^2 [11] [3], rather than ρ [1] [2] [24]

$$k = G\frac{l^2}{72\pi d}\left(\frac{\rho}{\rho_{\text{graphene}}}\right)^2 \tag{3.2.4}$$

For a cubic cell with side length equals to mesh size *D* (Figure 3.5), the cell density is given by $\rho_{\text{cell}} = 6\pi d\rho_{\text{graphene}}/D^2$. Considering geometry factor $\langle \cos\theta^2 \rangle = 1/3$ in a random SWCNT network, we have $\rho \cong \rho_{\text{cell}}/3$. Thus, mesh size and density have this approximation relation $\rho \cong 2\pi d\rho_{\text{graphene}}/D^2$. Eq. (3.2.4) can be rewritten as

$$k_{\text{junc}} = \frac{\pi G d l^2}{18 D^4} \tag{3.2.5}$$

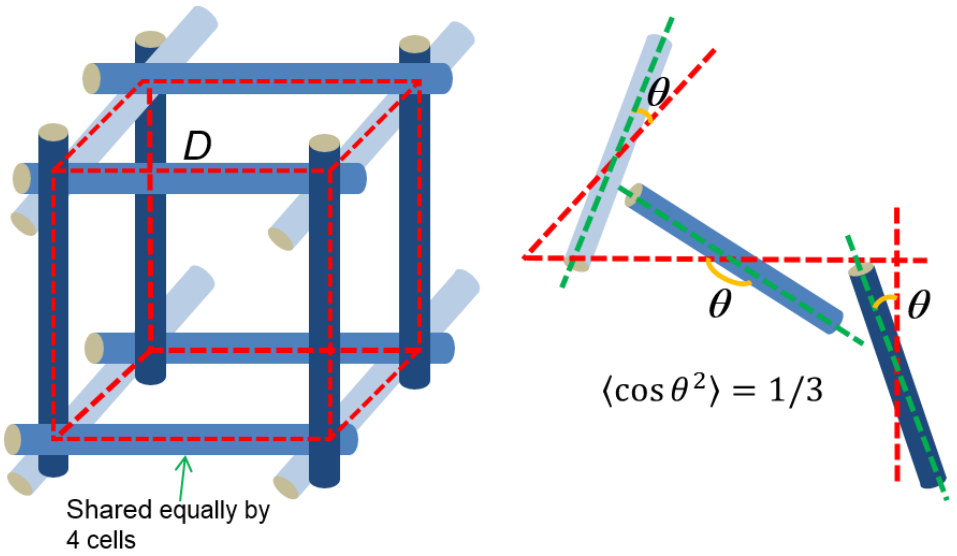

Figure 3.5 Schematic representation of the relation between mesh size and density in a random SWCNT network.

We choose an average mesh size of D = 20 nm for the as-grown samples (which have volume fractions of ~0.52% and ~0.49%) based on small-angle neutron scattering measurements of pristine SWNT networks with 0.5% volume fraction. [6] As shown in Fig. 3.6 (a) and (b), the average individual junction conductances of the pristine SWNT networks derived from their measured thermal conductivities are very close to the value of 60 pW K^{-1} predicted by a Green's function model for a single isolated (non-network) van der Waals bonded SWCNT junction. [2] To compare these average individual junction conductances to those of dense SWCNT networks, we re-apply the SWCNT network density relation and derive values of G for dense SWCNT networks [23] [25] [26] [27] [28] using $G=G_P(\rho_P/\rho)^2 k/k_P$, where P refers to the pristine samples. Note that the thermal conductance of a single junction is proportional to k/ρ^2. The results plotted in Fig. 3.6, show that the thermal conductances of junctions in dense SWCNT networks have a typical magnitude of 2 pW K^{-1}, or 30 times less than that of the as-grown aerogel.

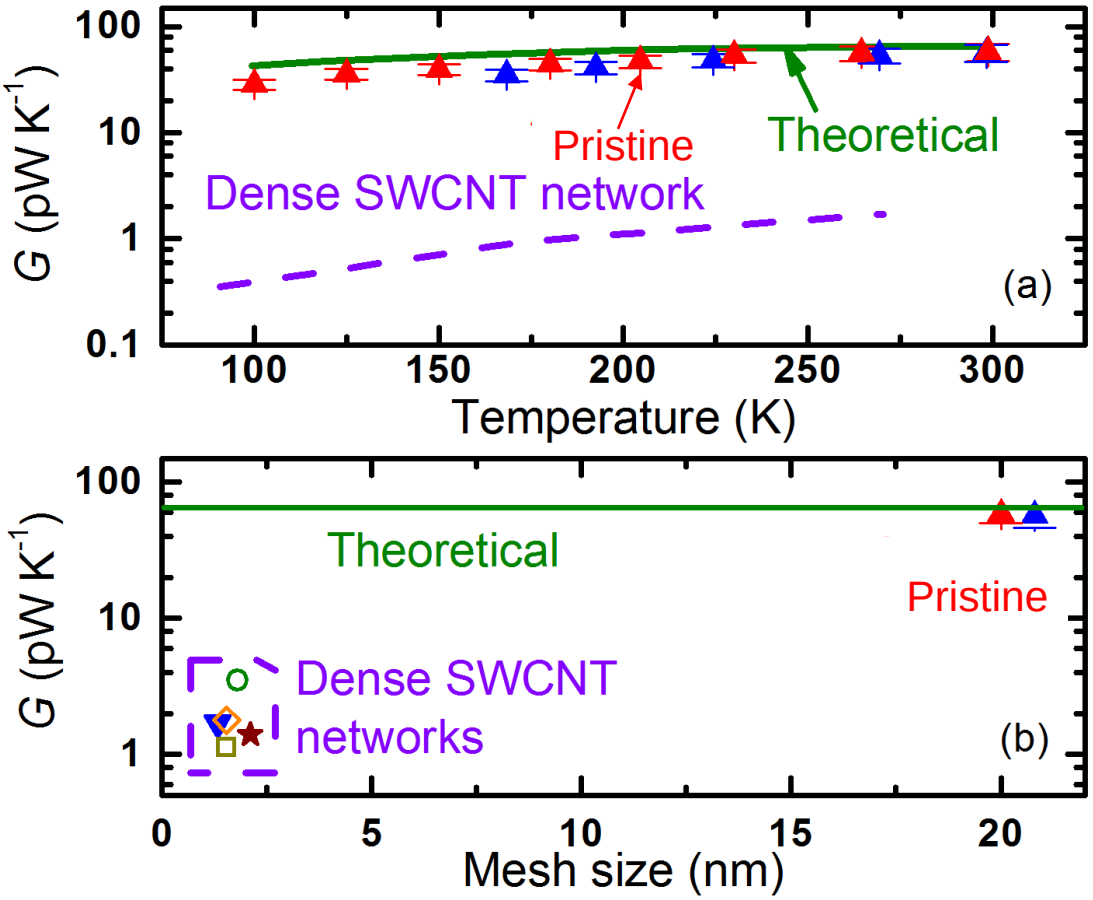

Figure 3.6 (a) Derived average junction thermal conductances for two pristine SWCNT aerogels (data points) and for a dense SWCNT network (dashed line), [23] and a theoretical junction thermal conductance of two isolated (non-network) van der Waals bonded (10,0) SWCNTs (solid line). [2] (b) Average junction thermal conductances of SWCNT networks with various mesh sizes: dense networks (▼,◇, □,★) [23] [25] [26] [27] and as-grown SWCNT aerogels (▲ red and blue). For ◇ and □, an isotropic SWCNT network of volume fraction 70% (typical of buckypaper) [28] is used to estimate the mesh size. Also shown is the theoretical junction thermal conductance of two isolated (non-network) van der Waals bonded (10,0) SWCNTs (dashed line) [2] and three crossed SWCNTs (○) from a Green's function calculation. [1]

Reduced junction thermal conductance due to phonon interference based on atomistic Green's function simulations [1] has been considered as the reason for the very small thermal conductivities of dense SWCNT networks. Based on a simple dominant phonon model [29] and a longitudinal acoustic phonon velocity of 24 km/s, [22] we predict dominant phonon wavelengths of 1.5 nm at 300K and 4.5 nm at 100K.

Dense SWCNT networks previously studied had a typical mesh size of 2.5 nm, [23] [25] [26] [27] [28] making the space between adjacent SWCNTs less than 1 nm, comparable to phonon wavelength. Because of their relatively wide junction spacing, our expectation that the interference effects will be less pronounced in aerogel networks is supported by the similarity of the derived average as-grown junction conductance to the predicted value for a single isolated (non-network) SWCNT junction. Furthermore, since ultralow density SWCNT networks exhibit the intrinsic properties of SWCNT-SWCNT junctions, they provide an accurate means to characterize single-junction thermal properties that are simpler and less prone to significant experimental uncertainties than measuring a single-junction resistance directly. [30]

The graphitic layers (composed of ~3nm long flakes between 1 and 5 atomic layers thick) [4] [5] accumulated at the junctions of the Gr-coated samples are expected to increase the contact area of each junction and hence its conductance G. [30] [31] Using the average number of layers (2.5) to scale [30] the junction conductance of the Gr-coated sample relative to that of the as-grown sample through $G_{Gr} = G_{AG} \times (d_{Gr}/d_{AG})^2$, and accounting for its same average mesh size D = 20 nm (since the graphitic coating is applied to the as-grown sample and therefore does not affect the mesh size[4]), we plot both the calculated total junction resistance R_{junc} and the total measured thermal resistance R as shown in Fig. 3.7 (a).

Since the small (less than 8%) contribution in our samples made by the junction resistance is not large enough to account for the measured thermal conductivity plateau, we use the difference $R - R_{junc}$ as the resistance of the Gr-coated SWCNTs themselves (R_{NT}) and study the effect of the graphitic layers on phonon boundary scattering. Using the same ballistic phonon velocity derived for the as-grown aerogel, we find that l_{mfp} for the Gr-coated SWCNT aerogel is on the same order as the

nanotube diameter, consistent with the Casimir limit ($l_{mfp} \approx d$) [31] and other 1D nanostructures such as Si nanowires coated with germanium. [32] Previous models for coated 1D systems predict a frequency-dependent l_{mfp} that falls to a minimum at a particular frequency due to strong phonon coupling at that frequency between the 1D system and the coating. [33] Using a dominant phonon model [1]and the Debye temperature T_D = 960 K for (10, 10) SWCNTs, [22] we translate this frequency dependence into a temperature dependence and find qualitative agreement with the trend in $l_{mfp}(T)$ derived for the Gr-coated samples (Fig. 3.7 (b)) as well as quantitative agreement in the temperature of the minimum. Our analysis suggests that the thermal conductivity plateau occurs because the dominant phonon mean free path reaches a minimum at that temperature.

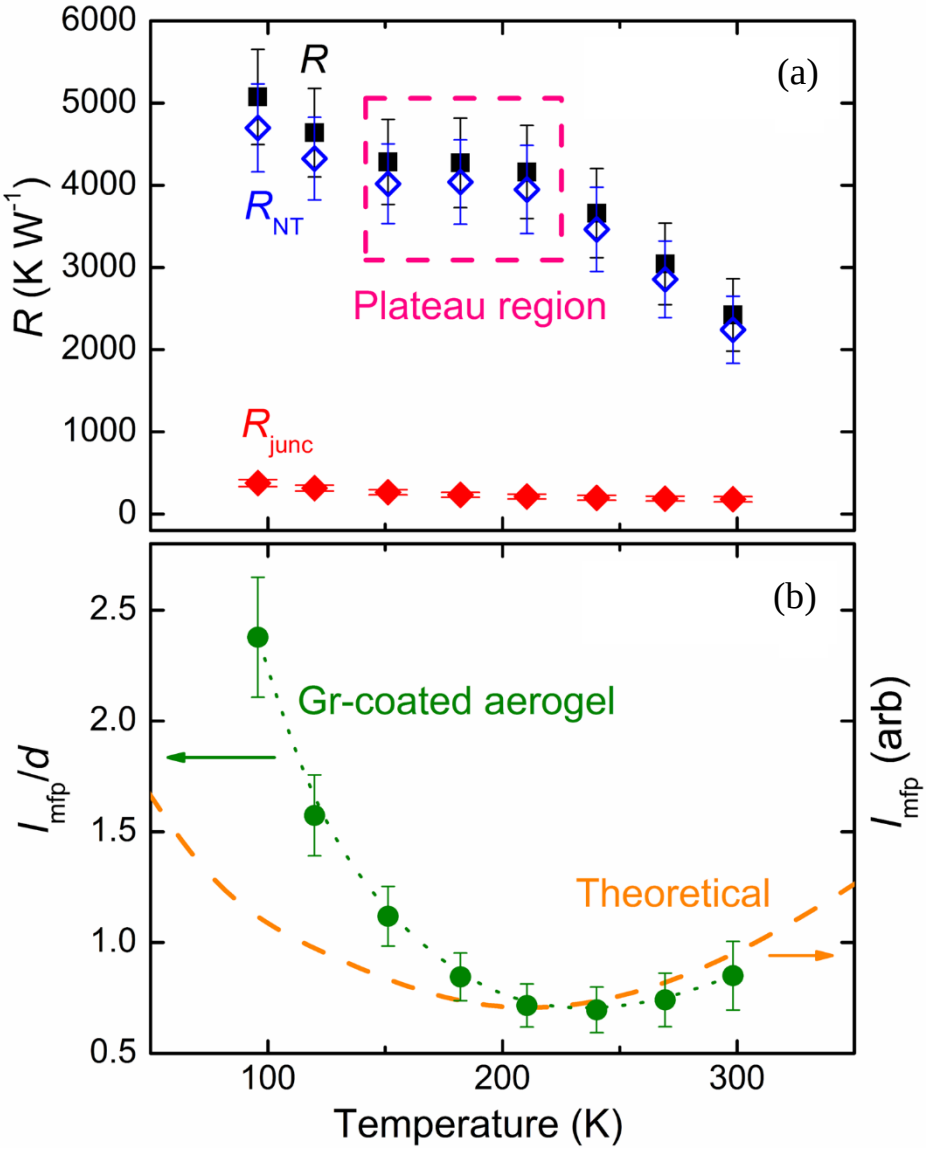

Figure 3.7 Analysis of observed thermal conductivity plateau. (a) Temperature-dependent components of thermal resistance for Gr-coated samples. ■: R from measurement (radiation excluded), ◇ : R_{NT}, ◆ : R_{junc}. (b) Temperature-dependent phonon mean free path l_{mfp}: predicted for a coated nanowire (orange dashed line),[7] derived for Gr-coated SWCNT aerogel (●).

The measured electrical conductivities of the SWCNT aerogels (derived from $\sigma = I \times t_s/(V \times A_s)$) are shown in Fig. 3.8. As observed in other SWCNT networks, the electrical conductivities of all samples increase with temperature due to tunneling at the junctions. [23] Similar to the thermal conductivity measurements, the electrical conductivities of the Gr-coated samples are much lower than those of the as-grown sample.

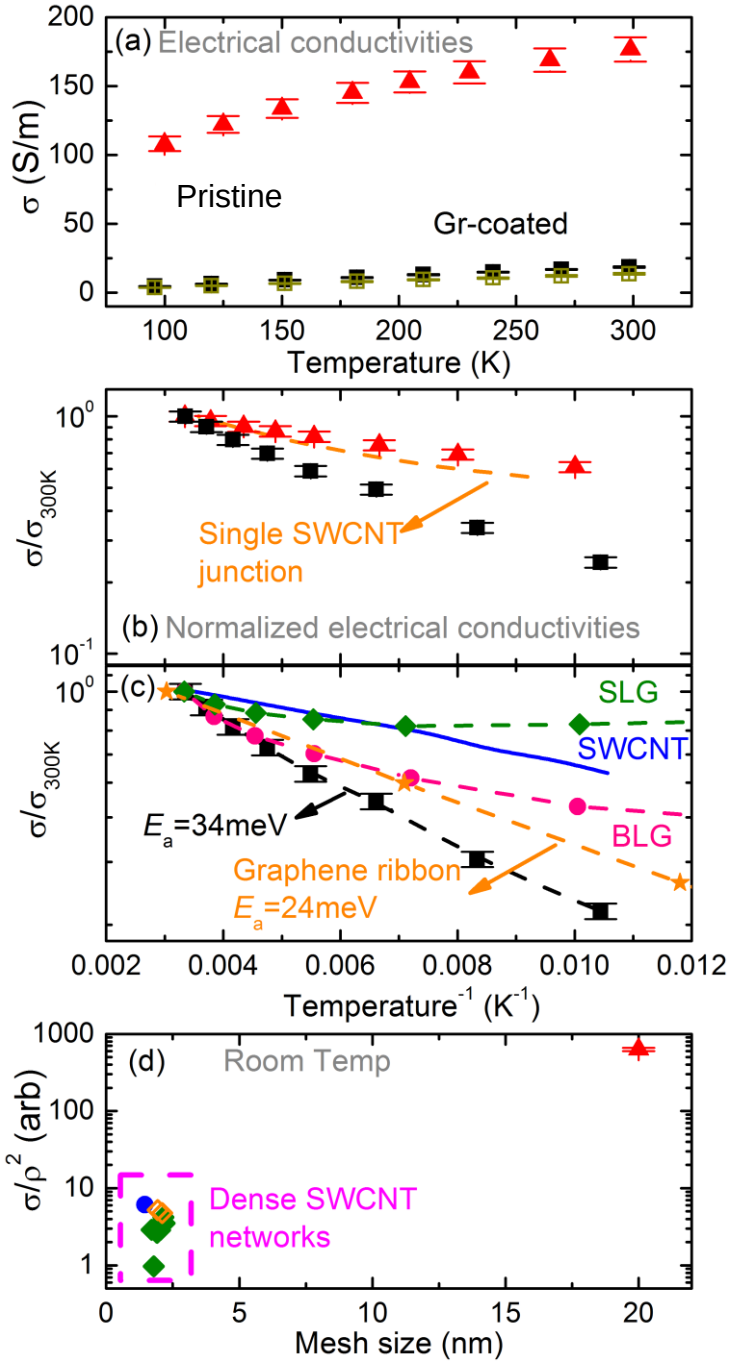

Figure 3.8 Electrical properties. (a) Electrical conductivities of SWCNT aerogels vs. temperature. ▲: pristine, ■ (black and olive): Gr-coated. (b) Temperature dependence of normalized conductivity of SWCNT aerogels. Dashed line shows data for an isolated (non-network) junction between two metallic SWCNTs.[37] (c) Temperature-dependent normalized conductivity of Gr-coated aerogel and: (solid line) a single 1.3 nm diameter SWCNT; [34] ◆: a single layer of graphene; [35] ●: bilayer graphene; [35] ★: a graphene ribbon with a width of 36 nm. [36](d) Junction electrical conductances of as-grown aerogel and dense SWCNT networks at room temperature. ◇,◆, ●: dense networks. [37] [23]

Similar to phonon transport, the mean free path and coherence length of electrons in SWCNTs are on the order of μm, [38], i.e., transport at the junctions dominates electrical transport in pristine SWCNT networks. [3] Similar to the way that the average junction thermal conductance in a network is proportional to k/ρ^2, the average junction electrical conductance in a network is proportional to σ/ρ^2. As shown in Fig. 3.8 (d), the average junction electrical conductance of an as-grown SWCNT aerogel is approximately 2 orders of magnitude greater than that of a dense or bundled SWCNT network. [23] [37] Following calculations equivalent to those given above for thermal conductance, we derive an average junction contact resistance for the as-grown aerogel of 9.8 MΩ. While smaller values in the range of 0.43-2.3 MΩ have been measured for a junction between two isolated (non-network) SWCNTs on a silicon dioxide substrate, [39] substrate effect has also been shown to pull SWCNTs into closer contact than when they are free-standing as in the SWCNT aerogels measured here.[6] The similarity in the temperature dependence of the electrical conductance for the SWCNT aerogel junctions and the isolated (non-network) junction (Fig. 3.8 (b)) further supports the electrical ideality of the SWCNT aerogel junctions. [40]

The Gr-coated aerogel has a lower electrical conductivity than the as-grown aerogel (suggesting increased carrier scattering due to the coating) and greater temperature dependence (Fig. 3.8 (c)) than the as-grown aerogel, a single SWCNT, single-layer graphene, bilayer graphene, or a graphene ribbon. [34] [35] [36] These differences between the as-grown and Gr-coated aerogels likely arise from a perturbation of the structural symmetry and band structure of the SWCNTs by the graphitic coating similar to the way these characteristics are perturbed in single-layer graphene when adding a second layer [35]. The derived activation energy for the Gr-coated aerogel is E_a = 34 meV is consistent with the values found for graphene ribbons [36].

Measured *S* data for the SWCNT aerogels are shown in Fig. 3.9. Unlike thermal conductivity and electrical conductivity, *S* does not have a strong dependence on density. The similarity of the *S* of the as-grown aerogel to a single (10, 0) SWCNT, [20]or a dense SWCNT network [41] suggests that *S* does not strongly depend on the junction properties. Both experiments [20] and simulations [42] have suggested that phonon drag effects strongly contribute to the Seebeck coefficient of a SWCNT and also increase over the temperature range of 10-300K. In fact, we find a much lower Seebeck for the Gr-coated aerogel than for the as-grown aerogel, as increased phonon scattering reduces ballistic phonon transport and hence the contribution of phonon drag(as well as the thermal conductivity discussed above).

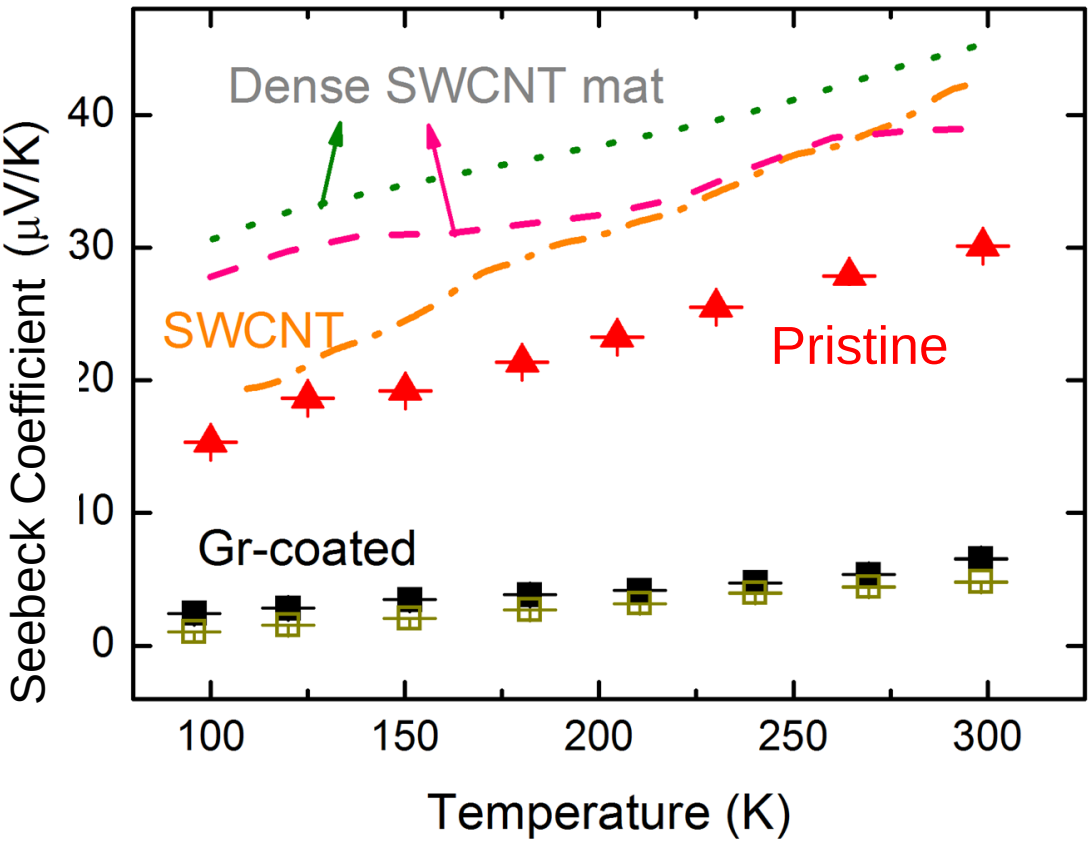

Figure 3.9 Seebeck coefficient. ▲: pristine, ■(black and olive): Gr-coated, dashed-dotted line: single (10, 10) SWNT, [20] dashed line: laser-synthesized dense SWNT mat, [41] dotted line: arc synthesized dense SWNT mat. [41]

3.3 BN-/ PEDOT:PSS-Coated SWNT Networks

The measured thermoelectric properties of the BN-coated and PEDOT:PSS-coated SWCNT networks and the references from the pristine and Gr-coated samples are shown in Fig. 3.10. The BN/SWNT (0.5/0.53) sample has a density and coating/SWNT ratio similar to the Gr-coated sample. It has lower thermal conductivity, increased electrical conductivity, and improved Seebeck coefficient compared to the Gr-coated sample, and the highest *ZT* value among all samples. Keeping the network density but increasing the coating/SWNT ratio (BN/SWNT = 1.7/0.3) doubles the thermal conductivity and stabilizes the electrical conductivity and Seebeck. We suggest that the improved coupling between the BN coating and SWNT backbones increases the heat-flow exchange to and from the coating [33]. The improved thermal conductivity may also be result from the excess BN coating contributing to thermal conductivity while the coated SWNT backbone remains at its lowest value.

The tradeoff between the thermal conductivity decrease of SWNT and the coating increase, can be explained by that the fact that the thermal conductivity of SWNT drops quickly with N dopants (see Chapter 4 for the details). Therefore, the optimum coating/SWNT ratio should not be a large number, which is consistent with our experiments, i.e., sample BN/SWNT(24.6/1) of mild density and very large coating/SWNT ratio has the highest thermal conductivity and the lowest electrical conductivity and Seebeck. Although we expected to observe a strong enhancement of both thermal and electrical conductivity via the BN-coating by the covalent bonds created between SWNT junctions, our experiments did not show it.

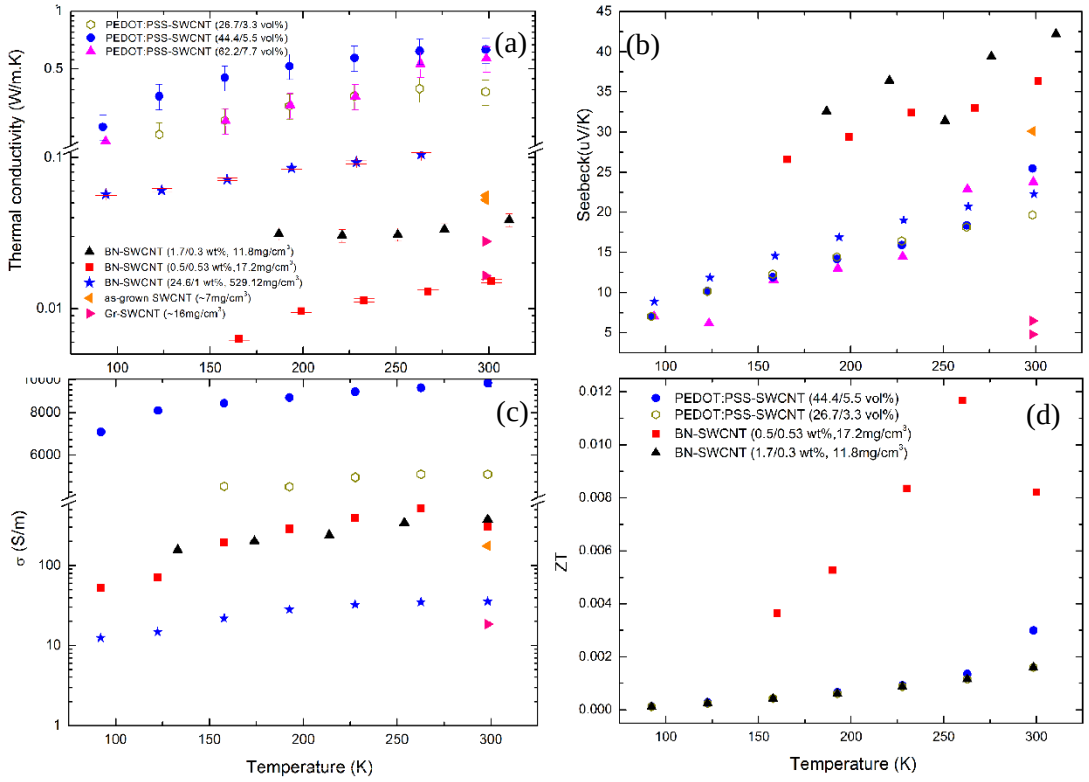

Figure 3.10 Thermoelectric properties of BN-and PEDOT:PSS-coated SWNT networks. (a)Thermal conductivity. (b) Seebeck coefficient. (c) electrical conductivity. (d) *ZT*.

The PEDOT:PSS coated samples have similar thermal conductivity to that of high *ZT* PEDOT:PSS film. [43] The electrical conductivity, however, is only 10% and the Seebeck coefficient is only 30% of that in PEDOT:PSS film. We conclude that a better de-doping method for 3D networks is still needed.

3.4 Summary

The dramatic (order of magnitude) improvements in the thermal and electrical conductances of the SWCNT junctions in ultra low density SWNT networks are measured and compared to previously reported junction conductances in dense SWCNT networks. The average junction conductances of the aerogel network are found to be close to the ideal thermal and electrical conductances at the junction of two isolated (non-network) van der Waals bonded SWCNTs, [2] [39], which suggests

the elimination of collective effects. Coating the junctions and nanotubes with a few layers of graphene/BN to improve the aerogel networks‘ mechanical properties [4] [7] degrade both electrical and thermal performance as the junction impedances became outweighted by the increased impedances of the coated SWCNTs themselves. The coating also caused a plateau region to in the aerogel thermal conductivity over a range of temperatures in the Gr-coated samples, which is consistent with a temperature-dependent phonon mean free path. [33] Reduction in the ballistic transport of phonon is evidenced by both thermal conductivity and Seebeck coefficient measurements; the latter suggests that increased phonon scattering in the Gr-coated aerogel reduces the contribution of phonon drag.

[1] R. S. Prasher, X. J. Hu, Y. Chalopin, N. Mingo, K. Lofgree, S. Volz, F. Cleri and P. Keblinski, "Turning carbon nanotubes from exceptional heat conductors into insulators," *Phys. Rev. Lett.*, vol. 102, p. 105901, 2009.

[2] Y. Chalopin, S. Volz and N. Mingo, "Upper bound to the thermal conductivity of carbon nanotube pellets," *J. Appl. Phys.*, vol. 105, p. 084301, 2009.

[3] P. N. Nirmalraj, P. E. Lyons, S. De, N. Coleman and J. J. Boland, "Electrical connectivity in single-walled carbon nanotube networks," *Nano Lett.,* vol. 9, p. 3890, 2009.

[4] K. H. Kim, Y. Oh and M. F. Islam, "Graphene coating makes carbon nanotube aerogels superelastic and resistant to fatigue," *Nat. Nanotechnol.*, vol. 7, p. 562, 2012.

[5] K. H. Kim, Y. Oh and M. F. Islam, "Mechanical and thermal management characteristics of ultrahigh surface area single-walled carbon nanotube aerogels," *Adv. Func. Mater.*, vol. 23, p. 377, 2013.

[6] L. A. Hough, M. F. Islam, B. Hammouda, A. G. Yodh and P. A. Heiney, "Structure of semidilute single-wall carbon nanotube suspensions and gels," *Nano Lett.,* vol. 6, p. 313, 2006.

[7] Y. J. Jeong and M. F. Islam, "Compressible elastomeric aerogels of hexagonal boron nitride and single-walled carbon nanotubes," *Nanoscale,* vol. 7, p. 12888, 2015.

[8] J. Hone, M. Whitney, C. Piskoti and A. Zettl, "Thermal conductivity of single-walled carbon nanotubes," *Phys. Rev. B,* vol. 59, p. R2514, 1999.

[9] R. Fainchtein, D. M. Brown, K. M. Siegrist, A. H. Monica, E. Hwang, S. D. Milner and C. C. Davis, "Time-dependent near-blackbody thermal emission from pulsed laser irradiated vertically aligned carbon nanotube arrays," *Phys. Rev. B,* vol. 85, p. 125432, 2012.

[10] M. A. Panzer, H. M. Duong, J. Okawa, J. Shiomi, B. L. Wardle, S. Maruyama and K. E. Goodson, "Temperature-Dependent Phonon Conduction and Nanotube Engagement in Metalized Single Wall Carbon Nanotube Films," *Nano Lett.,* vol. 10, p. 2395, 2010.

[11] A. N. Volkov and L. V. Zhigilei, "Scaling laws and mesoscopic modeling of thermal conductivity in carbon nanotube materials," *Phys. Rev. Lett.,* vol. 104, p. 215902, 2010.

[12] Z. P. Yang, L. Ci, J. A. Bur, S. Y. Lin and P. M. Ajayan, "Experimental observation of an extremely dark material made by a low-density nanotube array," *Nano Lett.,* vol. 8, p. 446, 2008.

[13] M. A. Aegerter, N. Leventis , H. P. Ebert and M. M. Koebel, Aerogels handbook, New York: Springer, 2011.

[14] X. Lu, O. Nilsson, J. Fricke and R. W. Pekala, "Thermal and electrical conductivity of monolithic carbon aerogels," *J. Appl. Phys.,* vol. 73, p. 581, 1993.

[15] M. Wiener, G. Reichenauer, S. Braxmeier, F. Hemberger and H. P. Ebert, "Carbon aerogel-based high-temperature thermal insulation," *Int. J. Thermophys.,* vol. 30, p. 1372, 2009.

[16] J. Feng, J. Feng and C. Zhang, "Thermal conductivity of low density carbon aerogels," *J. Porous Mater.,* vol. 19, p. 551, 2012.

[17] V. Bock, O. Nilsson, J. Blumm and J. Fricke, "Thermal properties of carbon aerogels," *J. Non-cryst. Solids,* vol. 185, p. 233, 1995.

[18] A. Jagannathan, R. Orbach and O. E. Wohlman, "Thermal conductivity of amorphous materials above the plateau," *Phys. Rev. B,* vol. 13465, p. 39, 1989.

[19] J. E. Graebner, B. Golding and L. C. Allen, "Phonon localization in glasses," *Phys. Rev. B,* vol. 34, p. 5696, 1986.

[20] C. Yu, L. Shi, Z. Yao, D. Li and A. Majumda, "Thermal Conductance and Thermopower of an Individual Single-Wall Carbon Nanotube," *Nano Lett.,* vol. 1842, p. 5, 2005.

[21] C. Kittel, Introduction to solid state physics, New York: John Wiley and Sons, 1996.

[22] J. Hone, Carbon nanotubes: synthesis, structure, properties and applications. Topic in Applied Physics, Vol. 80, Berlin Heidelberg: Springer, 2001.

[23] M. E. Itkis, F. Borondics, A. Yu and R. C. Haddon, "Thermal conductivity measurements of semitransparent single-walled carbon nanotube films by a bolometric technique," *Nano Lett.*, vol. 7, p. 900, 2007.

[24] S. N. Schiffres, K. H. Kim, L. Hu, A. J. H. McGaughey, M. F. Islam and J. A. Malen, "Gas diffusion, energy transport, and thermal accommodation in single-walled carbon nanotube aerogels," *Adv. Func. Mater.*, vol. 22, p. 5251, 2012.

[25] J. Hone, M. C. Llaguno, N. M. Nemes, A. T. Johnoson, J. E. Fischer, D. A. Walters, M. J. Casavant, J. Schmidt and R. E. Smalley, "Electrical and thermal transport properties of magnetically aligned single wall carbon nanotube films," *Appl. Phys. Lett.*, vol. 77, p. 666, 2000.

[26] P. Gonnet, Z. Liang, E. S. Choi, R. S. Kadambala, C. Zhang, J. S. Brooks, B. Wang and L. Kramer, "Thermal conductivity of magnetically aligned carbon nanotube buckypapers and nanocomposites," *Curr. Appl. Phys.*, vol. 6, p. 119, 2006.

[27] J. E. Fischer, W. Zhou, J. Vavro, M. C. Llaguno, C. Guthy, R. Haggenmueller, M. J. Casavant, D. E. Walters and R. E. Smalley, "Magnetically aligned single wall carbon nanotube films: Preferred orientation and anisotropic transport properties," *J. Appl. Phys.* , vol. 93, p. 2157, 2003.

[28] B. W. Smith, Z. Benes, D. E. Luzzi, J. E. Ficher, D. A. Walters, M. J. Casavant, J. Schmidt and R. E. Smalley, "Structural anisotropy of magnetically aligned single wall carbon nanotube films," *Appl. Phys. Lett.*, vol. 77, p. 663, 2000.

[29] R. Prasher, T. Tong and A. Majumda, "Approximate Analytical Models for Phonon Specific Heat and Ballistic Thermal Conductance of Nanowires," *Nano Lett.*, vol. 8, p. 99, 2008.

[30] J. Yang, S. Waltermine, Y. Chen, A. A. Zinn, T. T. Xu and D. Li, "Contact thermal resistance between individual multiwall carbon nanotubes," *Appl. Phys. Lett.*, vol. 96, p. 023109, 2010.

[31] Y. F. Zhu, J. S. Lian and Q. Jiang, "Re-examination of Casimir limit for phonon traveling in semiconductor nanostructures," *Appl. Phys. Lett.*, vol. 92, p. 113101, 2008.

[32] R. Yang and G. Chen, "Thermal conductivity modeling of core−shell and tubular nanowires," *Nano Lett.*, vol. 5, p. 1111, 2005.

[33] N. Mingo and L. Yang, "Phonon transport in nanowires coated with an

amorphous material: An atomistic Green's function approach," *Phys. Rev. B,* vol. 68, p. 245406, 2003.

[34] C. Zhou, J. Kong and H. Dai, "Intrinsic electrical properties of individual single-walled carbon nanotubes with small band gaps," *Phys. Rev. Lett.,* vol. 84, p. 5604, 2000.

[35] S. V. Morozov, K. S. Novoselov, M. I. Katsnelson, F. Schedin, D. C. Elias, J. A. Jaszczak and A. K. Geim, "Giant intrinsic carrier mobilities in graphene and Its bilayer," *Phys. Rev. Lett.,* vol. 100, p. 016602, 2009.

[36] M. Y. Han, J. C. Brant and P. Kim, "Electron transport in disordered graphene nanoribbons," *Phys. Rev. Lett.,* vol. 104, p. 056801, 2010.

[37] P. E. Lyons, S. De, F. Blighe, V. Nicolosi, C. Pereira, M. S. Ferreira and J. N. Coleman, "The relationship between network morphology and conductivity in nanotube films," *J. Appl. Phys.* , vol. 044302, p. 104, 2008.

[38] M. Purewal, B. H. Hong, A. Ravi, B. Chandra, J. Hone and P. Kim, "Scaling of resistance and electron mean free path of single-walled carbon nanotubes," *Phys. Rev. Lett.,* vol. 98, p. 186808, 2007.

[39] M. S. Fuhrer, J. Nygard, L. Shih, M. Forero, Y. G. Yoon, M. S. C. Mazzoni, H. J. Choi, J. Ihm, S. G. Louie, A. Zettl and P. L. McEuen, "Crossed nanotube junctions," *Science,* vol. 288, p. 494, 2000.

[40] J. W. Park, J. Kim and K. H. Yoo, "Electrical transport through crossed carbon nanotube junctions," *J. Appl. Phys.,* vol. 93, p. 4191, 2003.

[41] L. Grigorian, K. A. Williams, S. Fang, G. U. Sumanasekera, A. L. Loper, E. C. Dickey, S. J. Pennycook and P. C. Eklund, "Reversible Intercalation of Charged Iodine Chains into Carbon Nanotube Ropes," *Phys. Rev. Lett.,* vol. 80, p. 5560, 1998.

[42] M. Tsaousidou, "Theory of phonon-drag thermopower of extrinsic semiconducting single-wall carbon nanotubes and comparison with previous experimental data," *Phys. Rev. B,* vol. 81, p. 235425, 2010.

[43] G. H. Kim, L. Shao, K. Zhang and K. P. Pipe, "Engineered doping of organic semiconductors for enhanced thermoelectricity efficiency," *Nature Mater.,* vol. 12, p. 719, 2013.

Chapter 4

Thermal conductivity of N-doped SWNT from Molecular Dynamics

4.0 Introduction

Intrigued by their prominent potential as thermal management materials, many research have studied the thermal conductivity of pristine CNTs experimentally [1] [2] [3] [4] and theoretically [5] [6] [7]. The quantities of CNTs needed in applications, however, preclude the use of pristine products, e.g., the BN-coated CNT networks with modified thermal conductivity is better than pristine CNT networks for the thermoelectric applications discussed in Chapter 3.

Defects (single vacancy, double vacancy, Stones-Wales, functionalized group with –OH/–H/–C_6H_5/–COOH) and dopants (isotope, substitutional N at extremely low concentration) have been shown to modify the thermal properties of CNTs [8] [9] [10] [11] [12] [13] [14]. Molecular dynamic- and first principles-based studies have predicted that thermal conductivity decreases as the defect concentration increases, with reductions as large as 80% depending on defect type and concentration.

The choice of modification can allow the electronic properties of CNTs to be deliberately tuned by doping. Nitrogen is a natural choice for a CNT dopant because its atomic radius is similar to carbon while it possesses one additional electron. Various theoretical studies have predicted that substitutional N doping in

semiconducting CNTs will exhibit strong electron donor states near the Fermi level and also increase the bandwidth. Thus, the greater mobility of charge-carriers should make them favorable to conduction. [15] [16] [17] Seebeck coefficient measurements in N-doped MWNTs have confirmed that the majority charge carriers are electrons, and in fact, the doping reduces the inter-tube hopping barrier for the charges. [18] Reduced thermal conductivity and increased electronic conductivity suggest N doping could be better than coating to increase the thermoelectric performance of CNT materials.

N-doped CNTs are also attractive for applications including field effect transistors (FET), field emission sources, bio- and gas-sensors, and metal storage. [19] [20] The thermal properties of N-doped CNTs play a key role in controlling the performance and stability of devices, e.g., FETs, which require accounting for the dissipation of waste heat to ensure optimal performance. [21] [22]

This chapter uses MD simulations to investigate the effects of dopant types and concentration on N-doped SWNTs. The pyridine-like N dopant is studied for the first time, and the doping concentration range is broader than previous available studies [11]. We begin by describing the simulation methodology and thermal conductivity prediction procedure, and then investigate the variation in thermal conductivity for 5 to 40 nm long SWNTs. A comparison of the phonon density of states (PDOS) of pristine and doped SWNTs demonstrates that thermal conductivity reductions are primarily due to the enhanced phonon scattering, which is further investigated in Chapter 5.

4.1 Molecular Dynamic Simulation Techniques

MD simulations can model phonon-phonon interactions, but not phonon-electron and electron-electron interactions. Since the electron contribution to the thermal

conductivity of CNTs can be considered negligible due to small electron specific heat, the phonon contribution dominates both MWNTs and SWNTs at all temperatures. [23] [24] [25] For this reason, the thermal conductivity obtained from a MD simulation, referred to as the lattice thermal conductivity, is expected to accurately represent the total thermal conductivity.

In general there are three ways to compute the thermal conductivity (k) of a solid. Non-equilibrium Molecular Dynamics (NEMD) is based on Fourier's law, which relates the heat current in the axial direction (z direction) to the axial temperature gradient through thermal conductivity. The heat flux is generated by exchanging the velocity vectors of an atom in the cool slab and one in the hot slab so that the temperature increases in the hot slab and decreases in the cool slab. The resulting temperature gradient is then measured as [26]

$$J_z = q_z V = -kV\frac{\mathrm{d}T}{\mathrm{d}z} \tag{4.1.1}$$

In principle, the use of NEMD techniques should allow for faster convergence [27] but there are some drawbacks: both finite size and boundary effects are serious concerns in nonhomogeneous NEMD simulations, and 1D systems do not obey Fourier's law, [28] meaning that k may not be calculated directly from the temperature gradient, although it is still a well-defined quantity in terms of heat currents. [28] [29]

Homogenenous NEMD (HNEMD) [30], a non-equilibrium approach, applies an external field to the system to represent the effects of heat flow without physically imposing a temperature gradient or flux. $\boldsymbol{F}_\mathrm{e}$ is the external field that adds an extra force $\Delta\boldsymbol{F}_\mathrm{i}$ each individual atom according to

$$\Delta\boldsymbol{F}_i = \left(\varepsilon_i - \langle\varepsilon\rangle\right)\boldsymbol{F}_e - \sum_{j\neq i}\boldsymbol{f}_{ij}\left(\boldsymbol{r}_{ij}\cdot\boldsymbol{F}_e\right) + \frac{1}{N}\sum_{jk(j\neq k)}\boldsymbol{f}_{jk}\left(\boldsymbol{r}_{jk}\cdot\boldsymbol{F}_e\right), \tag{4.1.2}$$

where ε is the atomic energy including both potential and kinetic energy, $\boldsymbol{f}_\mathrm{ij}$ is the

force on atom *i* due to atom *j*, and $\boldsymbol{r}_{ij}$ is the atomic position vector from atom *i* to atom *j*. Extrapolating to zero external field $\boldsymbol{F}_e$ and applying in the axial direction allows the thermal conductivity to be determined as [30]

$$k = \lim_{F_e \to 0} \lim_{t \to \infty} \frac{\left\langle J_z\left(\boldsymbol{F}_e, t\right)\right\rangle}{F_e T V}, \tag{4.1.3}$$

where the axial heat current it time averaged. The drawbacks are the challenge of extrapolating to zero field as well as the fact that the formation of solitons makes the approach improper for calculating *k* in 1D and quasi-1D systems. [31]

Equilibrium Molecular Dynamics (EMD) is based on the Green-Kubo formula derived from linear response theory. [32] A system is considered to be in an equilibrium state if the velocity distribution of the atoms corresponds to a Maxwell-Boltzmann distribution and if the total energy of the system is constant in time. EMD avoids the unphysical huge thermal gradient introduced in the system during NEMD simulations (~10^{10}K/m, difference of 50K in a 5nm long SWNT). Simplifying for the case of axial conduction yields the thermal conductivity expression [33]

$$k = \frac{V}{k_B T_{\mathrm{MD}}^2} \int_0^\infty \left\langle J_z\left(0\right) J_z\left(t\right)\right\rangle dt, \tag{4.1.4}$$

where k_B is the Boltzmann constant, T_{MD} is the temperature of the system (taken as the time average of the mean temperature of the system during the simulation), *V* is the volume of SWNT (a hollow cylinder with a thickness equal to 3.4Å), and J_z is the axial component of the heat current, given by

$$\boldsymbol{J}\left(t\right) = \frac{1}{V}\left(\sum_i \boldsymbol{v}_i \varepsilon_i + \frac{1}{2} \sum_{ij(i \neq j)} \boldsymbol{r}_{ij}\left(\boldsymbol{f}_{ij} \cdot \boldsymbol{v}_i\right)\right) \tag{4.1.5}$$

the heat current auto-correlation function (HCACF) in Eq. (4.1.5) is calculated using a

fast Fourier transform (FFT), which is much faster than the direct method. The numerical implementation of the FFT method is detailed in [34].

4.2 Pre Simulation

Various structural models have been proposed for the bonding configuration of N doping in CNTs. There are three primary ways that nitrogen can be incorporated into a CNT structure. [19] [35]

i) Substitutional: N is coordinated to three C atoms in sp^3-like fashion, which induces sharp localized states above the Fermi level associated with the injection of additional electrons into the structure.

ii) Pyridine-like: N is arranged around a vacancy, since the valency of the nitrogen can be satisfied by two sp^2 bonds, a delocalized π-orbital, and a lone pair in the remaining sp^2 orbital, pointing at the vacancy. As a result this configuration is non-doping (neither electron donor nor acceptor).

iii) Chemical adsorption of N_2 molecules.

We focus on the first two cases; the configurations are plotted in Fig. 4.1.

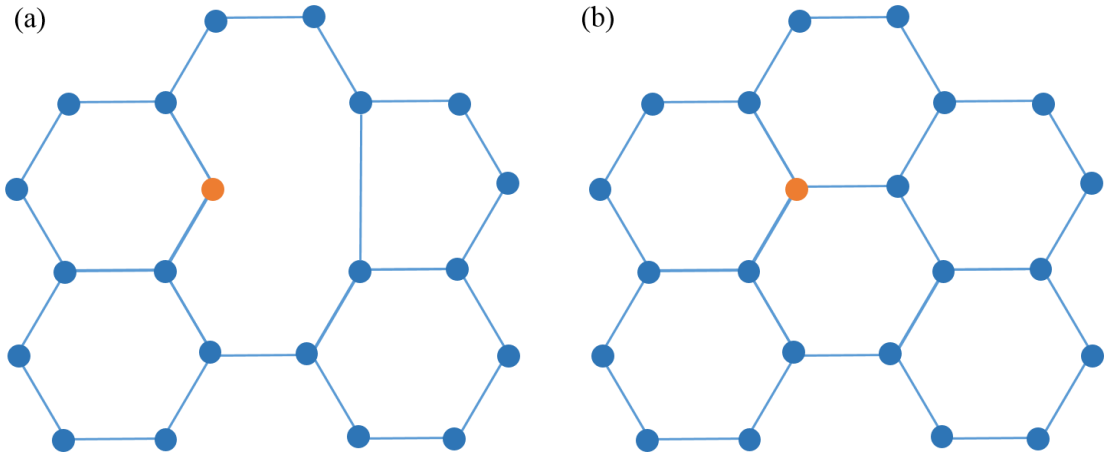

Figure 4.1 Two major bonding configurations for N in CNTs. (a) Pyridine-like N. (b) Substitutional N.

We use custom MATLAB scripts to create the initial position of pristine/substitutional-N-doped/pyridine-like-N-doped SWNTs by reading the coordinate locations of a pristine (13, 0) SWNT listed in an ×.xyz file constructed by using visual molecular dynamics (VMD) software nanotube builder developed by the theoretical and computational biophysics group in University of Illinois. The atom index of a pristine SWNT is shown in Fig. 4.2 (this is also critical in the phonon dispersion calculations presented in Chap. 5). To create structures having substitutional N/ isotope dopants, we select atom identification numbers at random and replace them with the dopant atoms. To create structures having pyridine-like N dopants, we first create N atoms that follow the same rule as the substitutional ones, and then create the vacancies as shown in Fig. 4.3. For each pyridine defect, there are two candidate lattice sites for vacancy; we select one at random and delete it from the compiled list.

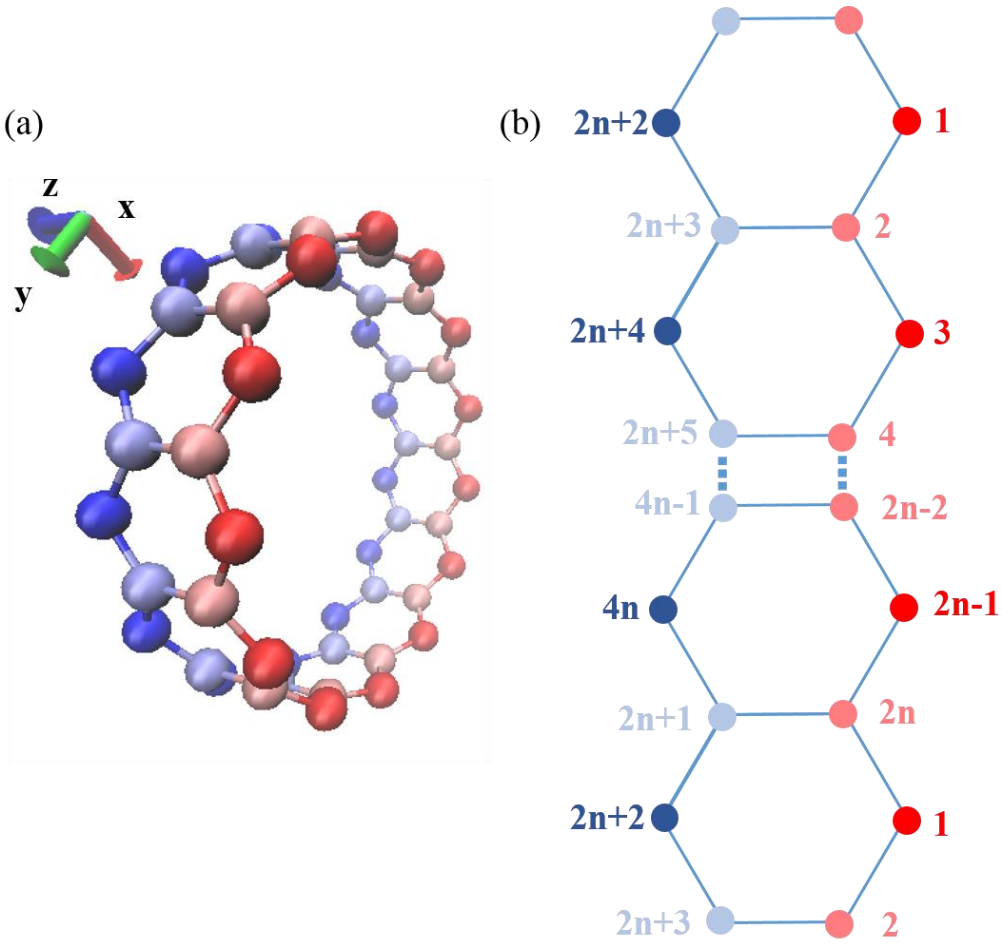

Figure 4.2 (a) A unit cell of a rolled (n, 0) CNT in the xyz plane. One unit cell consists of four atom rings distinguished in different colors. (b) The indices of the C atoms of the unrolled unit cell in the xy plane.

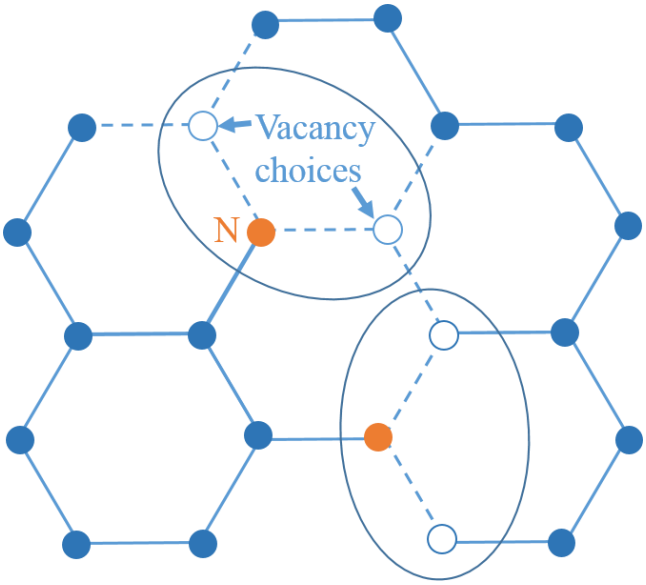

Figure 4.3 Constructing pyridine-like N-doped SWNT. For each N atom, there are two candidate lattice sites for vacancy. One of the candidates is selected at random and deleted from the structure.

We note that the choice of the inter-atomic potential is a crucial step in the simulation procedure, because it must properly represent both the microscopic and macroscopic properties of the simulated materials. We use the Tersoff potential developed for BN-C hybrid structures [36] to simulate the interactions between carbon/carbon and carbon/nitrogen. Between atom *i* and *j*, the Tersorff potential is

$$U_{ij} = f_C\left(r_{ij}\right)\left[A_{ij}\exp\left(-a_{ij}r_{ij}\right) - \gamma_{ij}B_{ij}\exp\left(-b_{ij}r_{ij}\right)\right], \tag{4.2.1}$$

where f_C is the cutoff function, and A_{ij}, a_{ij}, B_{ij} and γ_{ij} and b_{ij} are the parameters obtained by fitting for each material.

We find that the thermal conductivity of 5nm long pristine (13, 0) SWNT calculated from the BN-C Tersoff potential is within about 15% of that made using the second-generation REBO potential (there is no REBO potential includes interaction between C and N). [37] The difference caused by the slightly different form of potential used is within the acceptable range, considering the literature discrepancies of SWNT thermal conductivity (±~30 %). [21]

Next, we use periodic boundary conditions (PBCs) to avoid the boundary scattering at the ends of the samples with free boundary condition. Even though PBCs are meant to represent a system of infinite size, there are still issues which can cause finite size effect when using PBCs, e.g., the length dependence of thermal conductivity of SWNT using PBCs has been found in [6] [38], since no axial mode of wavelength larger than the simulation domain can exist.

As mentioned, the initial velocities of atoms in the system are assigned by custom MATLAB script, so that the velocity distribution matches the Maxwell-Boltzamann distribution. Letting $f(x)$ be the uniform probability density function (PDF), as in Fig. 4.4 (b), $F(x) = f(x)\mathrm{d}x$ is the cumulative distribution function (CDF) of the uniform distribution, as in Fig. 4.4 (a). Similarly, letting $f(v)$ be the Maxwell-Boltzmann PDF

at T_{MD}, as in Fig. 4.4 (d), allows us to obtain the Maxwell-Boltzmann CDF $F(v)$ by integrating $f(v)$, as in Fig. 4.4. (c). To obtain a mapping from $f(x)$ into $f(v)$, we find the value v_X by integrating f(v) on the interval [0, v_X] that gives the same probability as the integral of f(x) on the interval [0, X], where X is randomly given by the uniform function f(x). Finally, we randomly assign a direction to each of the velocity vectors.

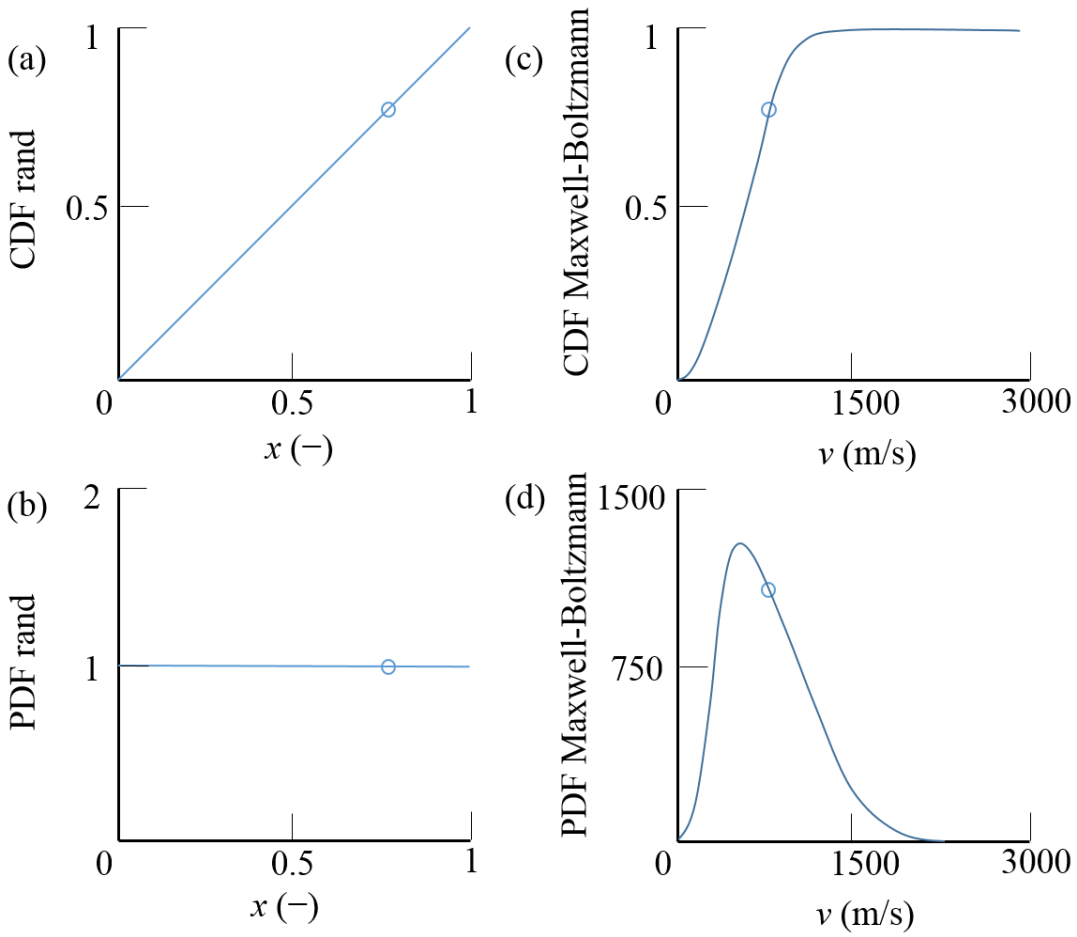

Figure 4.4 Assign initial atom velocities using uniform and Maxwell-Boltzmann distributions. The small circle in (b) is an example of a random point sampled from the uniform PDF with a corresponding $F(X)$ using the CDF (a). This probability must be the the same as the one given by the Maxwell-Boltzmann CDF (c). The velocity is then found by numerically integrating the Maxwell-Boltzmann PDF (d) until $F(v_X) = F(X)$.

Once the velocity vectors of all the atoms (in total N atoms) have been initialized, we remove the total linear and angular momenta of the system by subtracting the

linear and angular velocity components. Doing so ensures that the isolated CNT does not have translational or rotational movements, which simplifies the calculation of heat current along the tube axis. [39] We calculate the center of mass (CM) velocity and remove it as follows

$$\boldsymbol{v}_i\big|_{\text{new}} = \boldsymbol{v}_i\big|_{\text{old}} - \sum_j \frac{\boldsymbol{v}_j\big|_{\text{old}}}{N} \tag{4.2.2}$$

the angular momentum $\boldsymbol{L}$ and the moment of inertia coefficients tensor I of the system are given by

$$\begin{aligned} \boldsymbol{L} &= I\boldsymbol{\omega} = \sum_i m_i \left(\boldsymbol{r}_i \times \boldsymbol{v}_i\right) \\ I_{jk} &= \sum_i m_i \left(r_i^2 \delta_{jk} - r_{i,j} r_{i,k}\right) \quad j,k \in x,y,z \end{aligned}, \tag{4.2.3}$$

where j and k represent component of Cartesian coordinates (x, y, or z). The Cartesian components of the positon vector $\boldsymbol{r}_{\text{i}}$ are denoted by $\boldsymbol{r}_{\text{i,x}}$, $\boldsymbol{r}_{\text{i,y}}$, and $\boldsymbol{r}_{\text{i,z}}$. We obtain the angular velocity $\boldsymbol{\omega}$ from Eq. (4.2.2) and remove the rotational motion of the SWNT by applying

$$\boldsymbol{v}_i\big|_{\text{new}} = \boldsymbol{v}_i\big|_{\text{old}} - \boldsymbol{\omega} \times \boldsymbol{r}_i \tag{4.2.4}$$

We plot the initial velocity distributions from 5 independent runs using the above method. As shown in Fig. 4.5, 5 runs approximately reflect the shape of the Maxwell-Boltzmann distribution. We perform at least 5 independent runs for each set of simulations so that we can take ensemble averages to reduce noise.

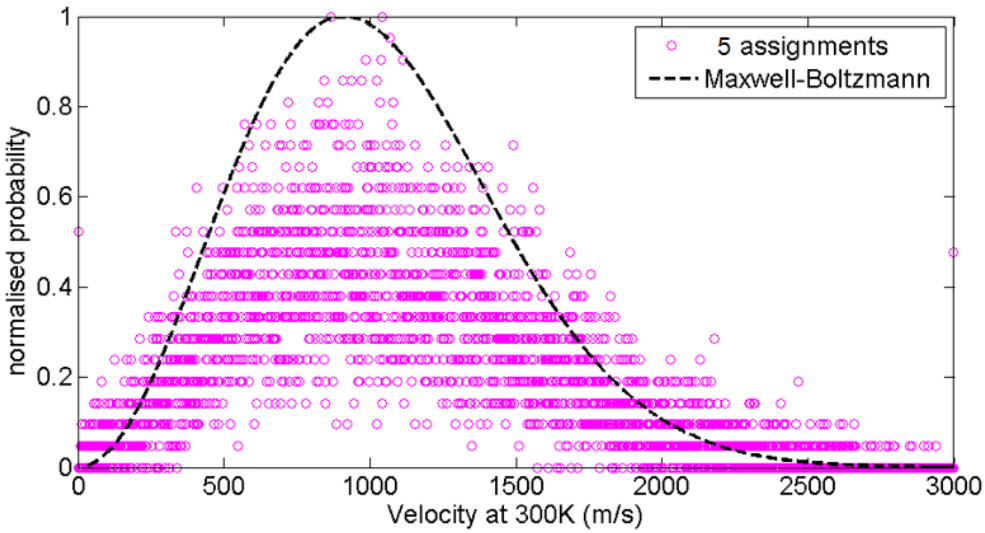

Figure 4.5 Initial velocity distribution of a 5nm long (13, 0) SWNT from 5 runs at 300K and the corresponding Maxwell-Boltzmann distribution.

The time steps of each simulation set are listed in Table 4.1. Note that smaller time steps for doped SWNTs maintain the simulation temperature fluctuations near the desired temperature and avoid increases which may cause (for example) the system to become unstable.

Table 4.1 Time steps for thermal conductivity simulation of (13, 0) SWNT.

Simulation set	Time step (fs)
Pristine	1
1% Substitutional doped (N/^{14}C isotope)	1
2~4% Substitutional doped (N/^{14}C isotope)	0.5
5% Substitutional doped (N/^{14}C isotope)	0.25
1% Pyridine-like N-doped	0.5
2~5% Pyridine-like N-doped	0.25

Well-equilibrated simulation structures with dopants and vacancies are achieved by performing a potential energy minimization routine [14] followed by 50ps of time integration with microcanonical ensemble (NVE). We bring each structure to the desired temperature (300K) using a minimum of 80ps of time integration with

canonical ensemble (NVT), which controls the simulation box temperature using a Nose-Hoover thermostat. Next, we monitor the potential energy of the samples for 40ps of NVE integration time to ensure constancy of the system's potential energy. Finally, we perform a 1.4ns long NVE to compute the heat current along the tube axis. HCACF is calculated up to 200ps, since after that it has decayed to approximately zero.

4.3 Post Treatment

To calculate thermal conductivity using EMD, it is necessary to integrate the HCACF (Eq. (4.1.4)). As suggested by [40], we fit the decay of the HCACF by the double exponential function

$$\left\langle J_z(0) J_z(t) \right\rangle = A_{\mathrm{ac,sh}} \exp\left(-\frac{t}{\tau_{\mathrm{ac,sh}}} \right) + A_{\mathrm{ac,lg}} \exp\left(-\frac{t}{\tau_{\mathrm{ac,lg}}} \right), \tag{4.3.1}$$

where the subscripts *ac,sh* and *ac,lg* denote the acoustic short-range phonon and acoustic long-range phonon, respectively. Physically $\tau_{\mathrm{ac,sh}}$ and $\tau_{\mathrm{ac,lg}}$ are interpreted as half of the period for energy transfer between two neighboring atoms (local time decay) and as the average phonon-phonon scattering time, respectively. [41] This allows us to obtain the thermal conductivity by performing direct integrals of these exponential functions.

When PBCs are used, phonons will reenter the simulation box and interfere with themselves at times longer than the time a phonon takes to ballistically traverse the nanotube, τ_b, thus resulting in spurious self-correlation effects in HCACF. [42] We estimate the time conservatively as the nanotube length l divided by the speed of sound of the longitudinal acoustic mode v_{LA} (20km/s) [23], which is the fastest traveling mode in the nanotube. For 5nm long SWNT, τ_b is around 0.25ps. Although a

fitting time $\tau < \tau_b$ can avoid the spurious effects, it improperly represents the slow exponential decay behavior because the relaxation time of the phonons that contribute to heat conduction has a fairly wide range; the details are given in Chap.5. Similar to that in [6], we use a longer fitting time (~20 τ_b, 5ps for 5nm long SWNT) to better represent the long exponential decay.

When calculating the HCACF, the contribution from acoustic phonons is immersed in the optical-phonon oscillations, and causes huge oscillations in the HCACF, making it difficult to fit with the exponential decay form. Therefore, we use a low-pass Butterworth filter to remove high-frequency optical phonon components in the HCACF. As a first approximation, we assume that the highest physical frequency in the system is the natural frequency that exists because of the spring-like bond between two adjacent atoms. [43] The spring constant Π can be approximated by

$$\Pi = \frac{\mathrm{d}^2 U}{\mathrm{d}^2 x}\Big|_{x=a}, \tag{4.3.2}$$

where U is the potential energy of one atom and a is the lattice constant. For the Tersoff potential used in this study and combined with Eq. (4.2.1), the natural frequency can be calculated as

$$f_{\mathrm{N}} = \sqrt{\frac{\Pi}{m}} = \sqrt{\frac{a_{ij}^2 A_{ij} \exp\left(-a_{ij} a\right)}{m}}. \tag{4.3.3}$$

The calculated spring constant is 7.01×10^{-7} N/nm, similar to the literature value [44] 6.52×10^{-7} N/nm. We calculate the natural frequency to be 18.7THz, which is very close to the frequency of the longitudinal acoustic mode at the Brilliouin zone edge (~23THz) derived from the phonon dispersion curve described in Chap. 5. We use this value as the cutoff frequency for the low pass filter. Fig. 4.6 shows the typical HCACF as a function of time before and after applying the filter. After the filtering,

most of the large oscillations are removed and the expected decay emerges.

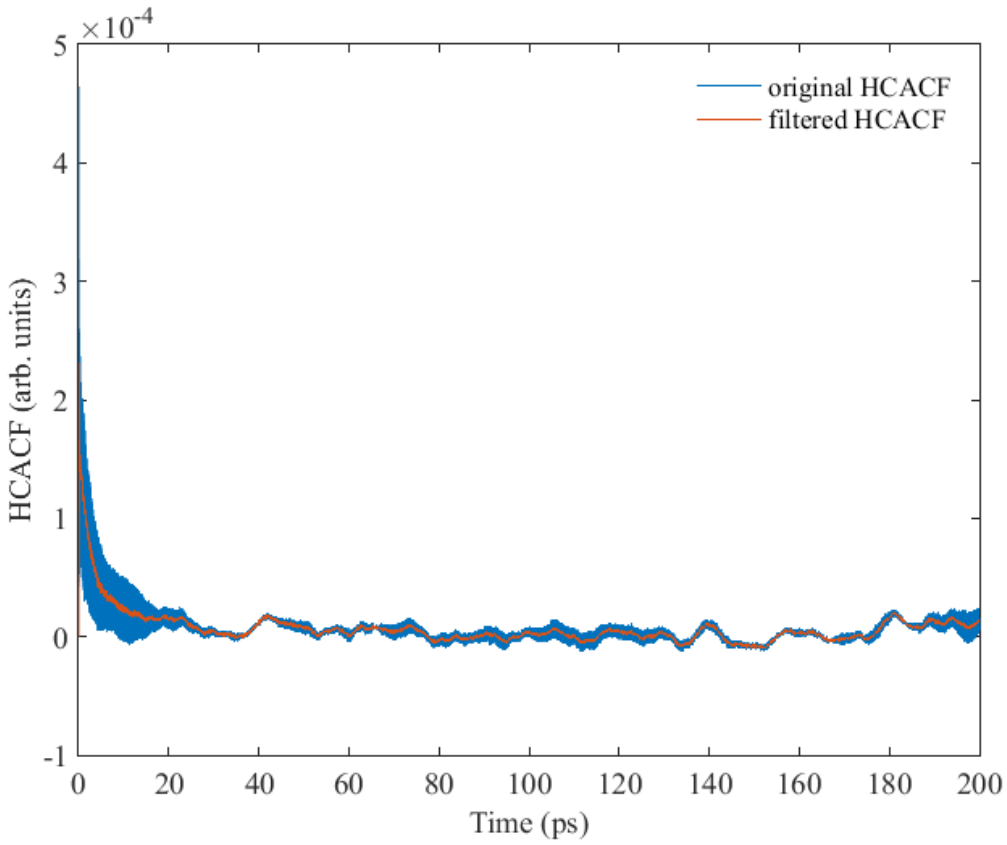

Figure 4.6 Typical HCACF with respect to time at 300K for a 5nm long (13, 0) CNT before and after filtering.

From the fitting, the typical relaxation time constants for short-range acoustic phonons and long-range acoustic phonons are listed in Table 4.2. An example of HCACF fitted to a double exponential function is shown in Fig. 4.7.

Table 4.2 Relaxation time constants at different length.

	$\tau_{ac,sh}$ (fs)	$\tau_{ac,lg}$ (ps)
5nm (pristine)	9.44	5.26
5nm (5% substitutional N-doped)	6.10	2.57
5nm (5% pyridine-like N-doped)	6.66	0.85
10nm (pristine)	9.54	10.3
20nm (pristine)	10.48	21.2
40nm (pristine)	11.16	38.9

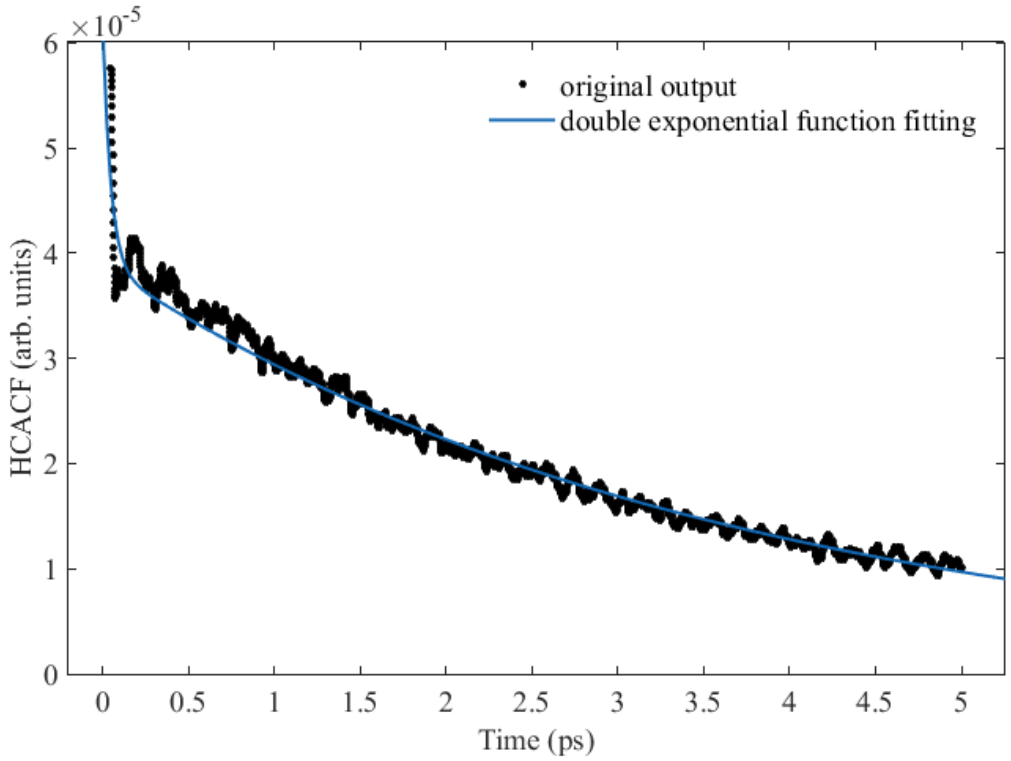

Figure 4.7 Example of HCACF and best fit of a 5nm long (13, 0) CNT, which is similar to the decay curve of a 5nm long SWNT (diameter 1.3nm) calculated in [45].

Table 4.2 shows that the fast relaxation time $\tau_{ac,sh}$ increases slightly with tube length, ranging between 7fs and 12fs, for the various cases considered. These local decay times are typically associated with half the vibration period of the C−C bond, which in general is a length independent quantity. Using the G-band mode frequency of 48THz [46] yields a $\tau_{ac,sh}$ value of 10.4fs, which is similar to the values obtained from fitting. The slight length dependencies shown in the table are likely due to minor fitting errors.

4.4 Thermal Conductivity Results and Analysis

Fig 4.8 shows the thermal conductivity as a function of doping concentration of ^{14}C isotope/substitutional N/pyridine-like N in 5nm long (13, 0) CNTs at 300K. The thermal conductivity of pristine SWNT is calculated to be 92 ± 8.5W/m·K, a reasonable value compared to 80W/m·K as previously calculated for a 5nm long (6, 6)

CNT [14]. It is also higher than that of a 5nm long (10, 10) CNT (40W/m·K) [6], most likely due to the larger fitting time used here.

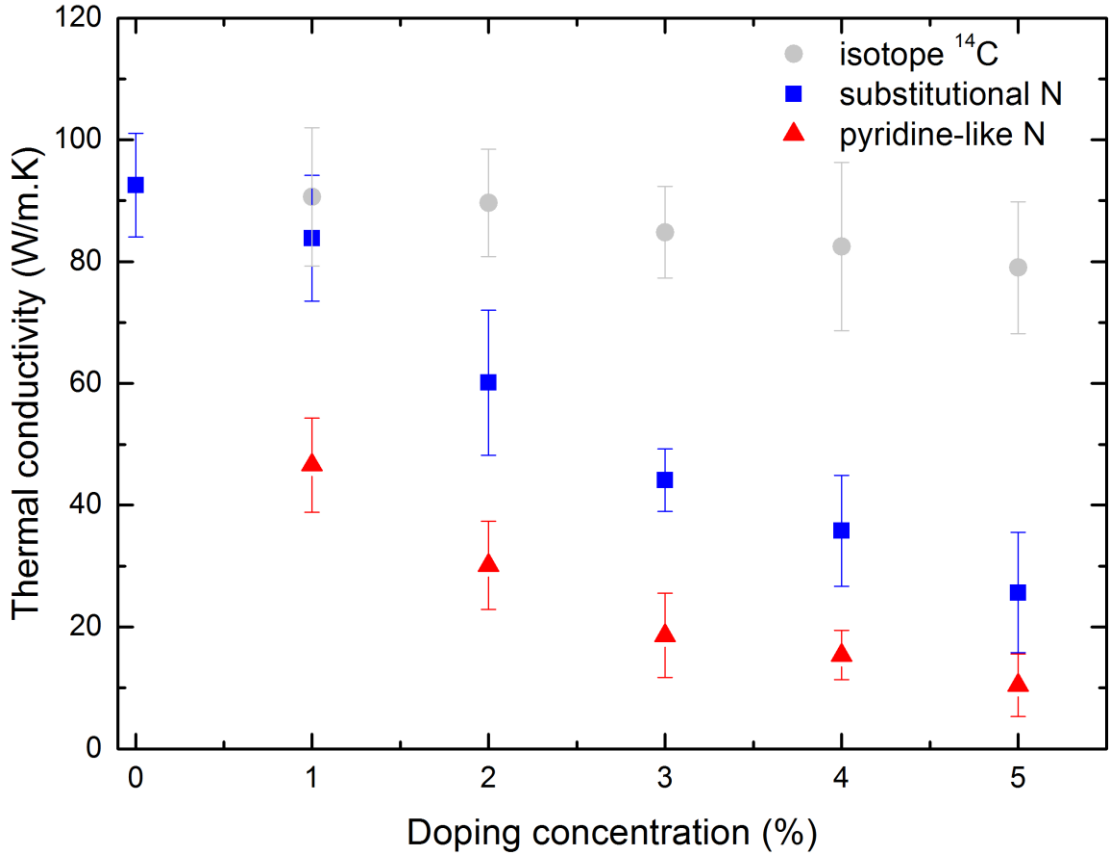

Figure 4.8 Thermal conductivity compared to doping concentration at 300K for 5nm long (13, 0) CNTs, with 1~5% isotope, substitutional N, and pyridine-like N dopants.

We also investigate the effect of dopant mass ratio by calculating the thermal conductivity of SWNT with ^{14}C impurities. Previous work studying a 1D diatomic chain indicated that a critical mass ratio (m_{light}/m_{heavy}), $r_{m,C}$ (~0.85), is required for the transition of thermal transport from ballistic to semi-ballistic/ diffusive. [47] A mass ratio larger than $r_{m,C}$ has a limited impact on thermal transport. In our case, the mass ratio for ^{14}C-doped SWNTs is 0.86, and we find that the thermal conductivities of isotope doped SWNTs and pristine SWNT are similar. For doped SWNTs, the thermal conductivity reduces almost linearly with increasing doping concentration. For 5% isotope concentration, the ratio of thermal conductivity ($k_{isotope}/k_{pristine}$) between isotope doped and pristine SWNTs is 85%. One study reported that this ratio is 61% at

10% concentration for a10nm long (5, 5) CNT [12], and 60% at 10.7% concentration for a 65nm long (7, 0) CNT [13].

Even though substitutional N dopants have the same mass ratio as ^{14}C, the ratios of thermal conductivity ($k_{subN}/k_{pristine}$) of substitutional N-doped SWNTs are much less than those of the isotope-doped ones, i.e., $k_{sub\_N}/k_{pristine}$ is 28% at 5% concentration. Similar to the isotope-doped SWNTs, there is a linear dependence between doping concentration and thermal conductivity. Using the ratio at 1% concentration, $k_{sub\_N}/k_{pristine}$ at 0.7% is 93.7%, which is consistent with 96% calculated from first principles [11].

For pyridine-like N-doped SWNT the ratio is even smaller, i.e., $k_{p\_N}/k_{pristine}$ is only 11% at 5% concentration.

For thermoelectric applications, we prefer substitutional N dopants because even a small amounts (1–5%) effectively reduce the thermal conductivity whereas larger concentrations (5–10% doped MWNTs) enhance electrical conductivity. [48]. We believe that pyridine-like N dopants could reduce thermal conductivity even more, but their effects on electrical conductivity are still unclear. One study suggested it is neither an electron donor nor an acceptor, but others suggest it would act as an electron acceptor, creating localized valence states and shifting the Fermi level to the valence band [49].

To understand the order of the thermal conductivities, we calculate the formation energy of dopants for the 1% doped samples, $\Delta\varepsilon_{def}$. For isotope-doped SWNTs, it is

$$\varepsilon_{dop} = \frac{E_{iso\_SWNT} - E_{pris\_SWNT}}{N_{dop}}, \tag{4.4.1}$$

where E is the total energy of the system, subscrips *iso_SWNT* and *pirs_SWNT* are the isotope doped and pristine SWNTs, respectively, and N_{dop} is number of dopant. For

N-doped SWNTs, it is [50]

$$\varepsilon_{\mathrm{dop}} = \frac{E_{\mathrm{N\_SWNT}} - E_{\mathrm{pris\_SWNT}} - N_{\mathrm{dop}}/2 \cdot E_{N_2}}{N_{\mathrm{dop}}}. \tag{4.4.2}$$

subscripts *N_SWNT* and N_2 are N-doped SWNT and nitrogen gas, respectively. At 300K the reduced pressure $P_r = P/P_c$ (where P_c is the critical pressure) of saturated N_2 equals 0.03 which is sufficiently low for ideal gas law to be valid (for $P_r < 0.1$, the error is less than 10%) [51]. Therefore, E_{N2} can be determined from the molecular kinetic energy, since it is much larger than the molecular potential energy. The average energy per molecular equals $3k_BT$, which is approximately 0.084eV.

Calculated formation energies and thermal conductivity ratios for various defect types are summarized in Table 4.3.

Table 4.3 Thermal conductivity ratios and defect formation energies for SWNT.

Defect type	Thermal conductivity ratios	Formation energy (eV)
^{14}C	98.5% @ 1% concentration 85.4% @ 5% 61% @ 10% [12] 60% @ 10.7% [13] [1]	0.15
Substitutional N	90.5% @ 1% 27.7% @ 5% 96% @ 0.7% [11]	1.23
Pyridine-like N	50.3% @ 1% 11.2% @ 5%	7.01
Add –H (out) [14][2]	74% @ 1% 45% @ 5%	——
Add $–C_6H_5$ (out) [9][3]	54% @ 1% 21% @ 5%	——
Add –C (out) [8]	84% @ 0.1%	4.0

Add –C (in) [8]	75% @ 0.1%	4.7
Vacancies	50% @ 1% [14]	
	25% @ 1% [52]	
Single vacancy [8]	61% @ 0.1%	6.9
Double vacancy [8]	54% @ 0.1%	9.3
Stone-Wales	71% @ 0.1% [8]	4.5 [8]
	30% @ 1% [53]	

[1] Derived from the data of 65nm long (7, 0) CNT.

[2] Derived from the data of 14nm long (6, 6) CNT.

[3] Derived from the data of 60nm long (10, 10) CNT.

The defect formation energy follows $\varepsilon_{iso} < \varepsilon_{sub\_N} < \varepsilon_{adatom} < \varepsilon_{pyridine\_N} \approx \varepsilon_{vacancy}$, and the thermal conductivities roughly follow the same order. Note that there is still significant uncertainty about the correct value for a SWNT with vacancy defects. The pyridine-like N-doped SWNT thermal conductivity calculated here is similar to those of CNT with Stone-Wales defects, even though the defect formation energy is higher.

Fig. 4.9 shows that the thermal conductivity increases as the system size increases. This is consistent with the length dependence reported in the literature. [12] Since the longest tube here is 40nm, the thermal conductivity is still far from its ultimate bulk value.

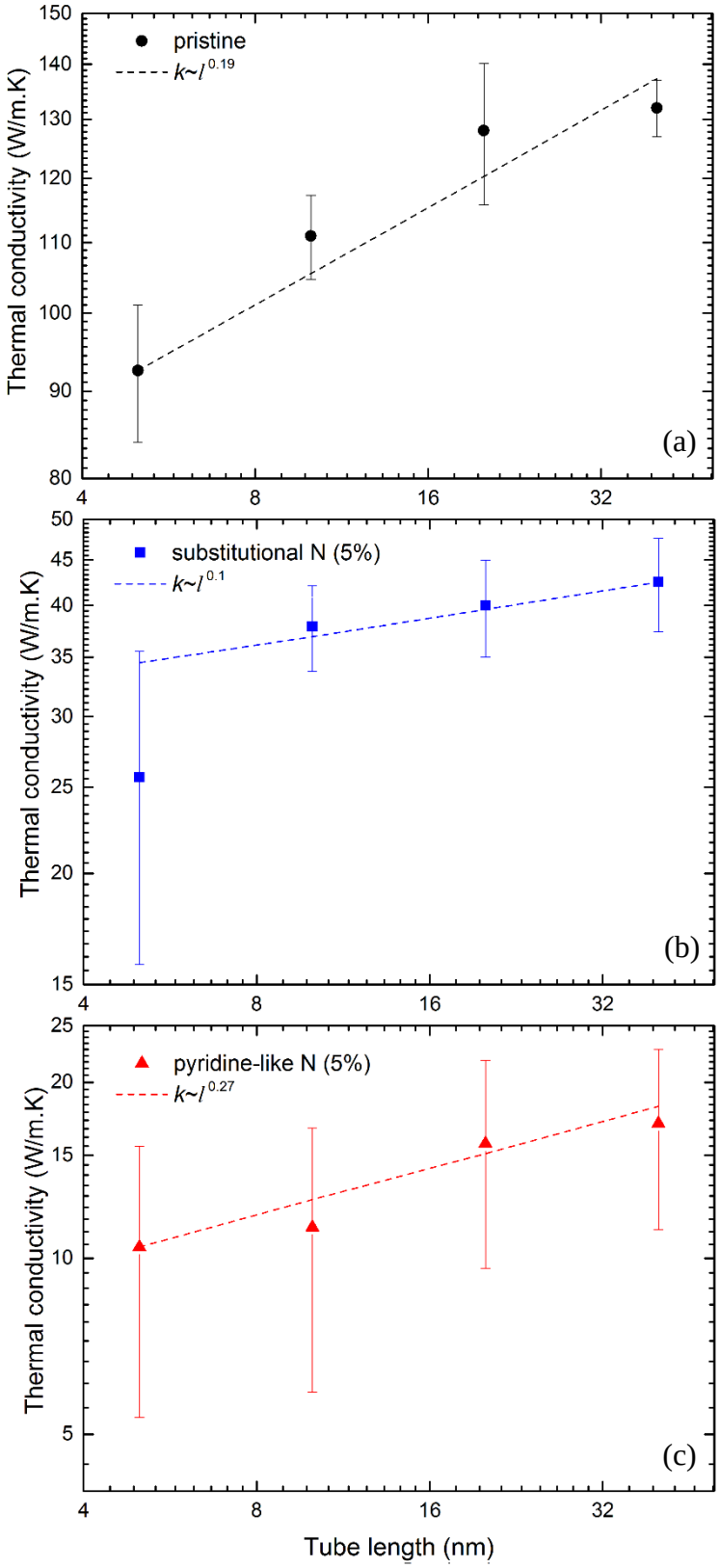

Figure 4.9 Thermal conductivity (k) compared to tube length (l) in Log-Log scale for (13, 0) CNT at 300K. In all cases, k is fitted to l in the form of $k \sim l^{\beta}$ (dashed line), whose slope is the value of β. (a) Pristine SWNTs. (b) 5% substitutional N-doped SWNTs. (c) 5% pyridine-like N-doped SWNTs.

The thermal conductivity of a 40nm pristine (13, 0) CNT at 300K is 132W/m·K, similar to the 158W/m·K for 40nm long and 160W/m·K for the 61.5nm long (10, 10) CNTs reported in [6] and [9]. There are two reasons for the length dependence of the thermal conductivity in the PBC cases. First, longer nanotubes allow additional modes, and each mode provides a new channel for heat transport. The additional modes have smaller wavevectors, which have a lower probability of Umklapp scattering, and thus are more long lived than the already existing higher frequency modes. When including these modes, the net effect is to increase both the overall phonon lifetime and the thermal conductivity. Some studies have showed that a normalized phonon density of states displays weak length dependence. [6] [54] The frequency distribution does not remain constant with increasing length; instead, redistribution toward lower frequencies occurs. In general, the lower frequencies have higher group velocities, meaning that the total thermal conductivity increases accordingly.

The thermal conductivity follows a power-law relationship with nanotube length $k \sim l^{\beta}$, as suggested by [12] [55]. The value of β reflects the strength of mode coupling. In CNTs, a stronger coupling between the longitudinal and transverse modes lead to a smaller value of β. [56] For a pristine (13, 0) CNT, β = 0.19, which falls between 0.15 for and (8, 8) CNT and 0.27 for a (5, 5) CNT [55]. This is consistent with the finding that mode coupling is weaker in tubes with smaller radii. [12] For substitutional N-doped SWNTs, the best fit leads to β = 0.1. Note that this value excludes the data of the 5nm case, but if we include the 5nm case, then the value of β increases. The best fit of pyridine-like N-doped SWNTs gives β = 0.27, suggesting that its mode coupling is weaker than that of pristine SWNTs.

Thermal properties strongly depend on the phonon density of states (PDOS), which is the number of vibrational states per unit frequency. We use the velocity autocorrelation function to calculate the PDOS. The full PDOS of a system is

proportional to the Fourier-transform of the velocity autocorrelation averaged over all atoms. Thus, the total PDOS of an N atom system at frequency ω is given by [57]

$$D(\omega) = \int_{-\infty}^{\infty} dt \frac{\sum_j \langle \boldsymbol{v}_j(t) | \boldsymbol{v}_j(0) \rangle}{\sum_j \langle \boldsymbol{v}_j(0) | \boldsymbol{v}_j(0) \rangle} \exp(i\omega t). \tag{4.4.3}$$

The projected PDOS along tube axis (D_z) gives the longitudinal PDOS, calculated by replacing the velocity vector in Eq. (4.4.3) with v_z. The full and longitudinal PDOSs of 5% substitutional N-doped SWNTs (5nm) are plotted in Fig. 4.10, and those of pristine SWNTs are also plotted for reference. The PDOS of 5% pyridine-like N-doped SWNTs is plotted in Fig. 4.11.

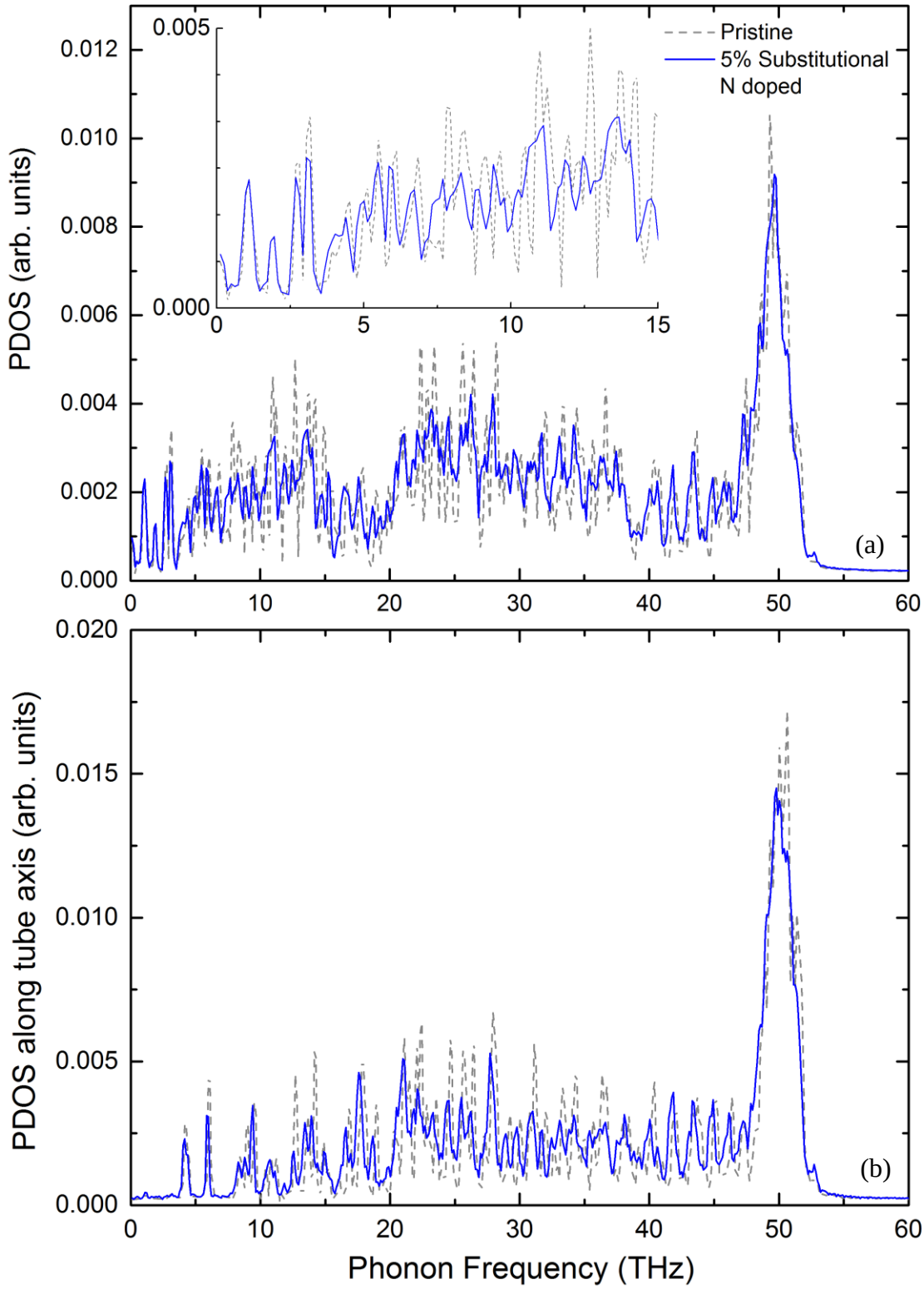

Figure 4.10 Phonon density of states at 300K for 5nm long (13, 0) pristine and substitutional N-doped SWNTs. (a) Full PDOS. Insert: PDOS at low frequencies. (b) Longitudinal PDOS.

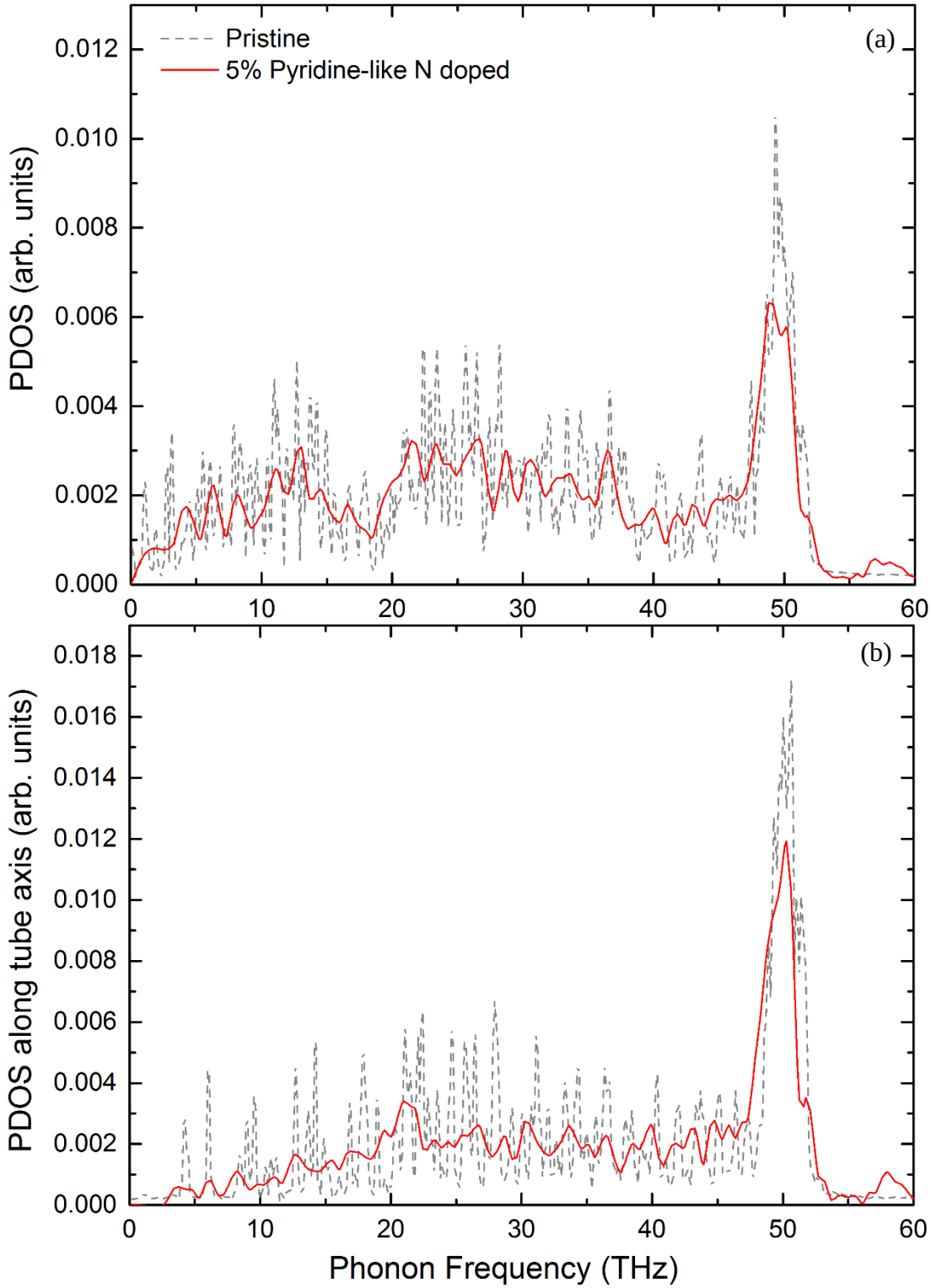

Figure 4.11 Phonon density of states at 300K for (13, 0) pristine and pyridine-like N-doped SWNTs. (a) Total PDOS. (b) Longitudinal PDOS.

Our calculated PDOS resemble others' work in shape. [6] [7] That is, longitudinal PDOS has stronger peaks at 50THz (G-band) than full PDOS, since the G-band is an optical mode related to the vibrations of C atoms within the tube surface. [46] In the

low frequency region, a longitudinal PDOS only covers part of the peaks shown in full PDOS. In pristine SWNTs, most peaks in the PDOS are kept after being doped with substitutional N atoms, while at the same time they are broadened particularly in the middle frequency region between 5 and 20THz. A slight redshift suggests that the phonon velocity changes very little. In pyridine-like N-doped SWNT, PDOS is greatly broadened; adjacent sharp peaks merge into broad single peak, and their magnitude reduces significantly. The integral of the PDOS is roughly the same for both pristine and doped SWNT, suggesting that specific heat is insensitive to dopants. Thermal conductivity can be expressed as [58]

$$k = Cv_{\mathrm{p}} l_{\mathrm{mfp}} / 3, \tag{4.4.4}$$

where C is the specific heat, v_{p} is the phonon velocity, and l_{mfp} is the phonon mean free path. Since the change of specific heat and phonon velocity is small, the greatly reduced thermal conductivity in N-doped SWNTs most likely results from the shortened phonon mean free path, i.e., the phonon lifetime is shortened due to scattering. To validate this finding, a deeper study of the phonon spectrum is developed in Chap. 5.

4.5 Summary

The thermal properties of N-doped SWNTs are systematically investigated. Using molecular dynamics simulations, we calculate the thermal conductivity for (13, 0) SWNT as a function of doping type, doping concentration, and length. Thermal conductivity from high to low is in the order of $k_{\mathrm{pris}} \sim k_{\mathrm{isotope}} > k_{\mathrm{sub\_N}} > k_{\mathrm{pyridine\_N}}$, which is the same order of their defect formation energies from low to high. Thermal conductivity increases with length for all doping cases. The thermal conductivity diverges with tube length as l^{β}, and the modes coupling in pyridine-like N-doped

SWNTs is weaker than those of pristine SWNTs. The phonon density of states reveal that the reduced thermal conductivity in N-doped SWNTs is primarily due to smaller phonon lifetimes. Substitutional N-doped SWNTs is found to be a good candidate for thermoelectric applications because their thermal conductivity is effectively reduced in the concentration region where electrical performance could be improved. While pyridine-like N dopants also effectively reduce thermal conductivity, their impact on electrical conductivity is still uncertain.

[1] C. Yu, L. Shi, Z. Yao, D. Li and A. Majumdar, "Thermal conductance and thermopower of an individual single-wall carbon nanotube," *Nano Lett.*, vol. 5, p. 1842, 2005.

[2] E. Pop, D. Mann, Q. Wang, K. Goodson and H. Dai, "hermal conductance of an individual single-wall carbon nanotube above room temperature," *Nano Lett.*, vol. 6, p. 96, 2006.

[3] J. Hone, M. C. Llaguno, N. M. Nemes and A. T. Johnson, "Electrical and thermal transport properties of magnetically aligned single wall carbon nanotube films," *Appl. Phys. Lett.* , vol. 77, p. 666, 2000.

[4] J. Hone, M. Whitney, C. Piskoti and A. Zettl, "Thermal conductivity of single-walled carbon nanotubes," *Phys. Rev. B*, vol. 59, p. R2514, 1999.

[5] D. Donadio and G. Galli, "Thermal conductivity of isolated and interacting carbon nanotubes: comparing results from molecular dynamics and the Boltzmann tranport equations," *Phys. Rev. Lett.*, vol. 99, p. 255502, 2007.

[6] J. R. Lukes and H. Zhong, "Thermal conductivity of individual single-wall carbon nanotubes," *J. Heat. Trans.*, vol. 129, p. 705, 2007.

[7] S. Maruyama, "A molecular dynamics simulaton of heat conduction of a finite length single-walled carbon nanotube," *Microscale Thermophys. Eng.*, vol. 7, p. 41, 2003.

[8] H. Chen and A. J. H. McGaughey, "Thermal conductivity of carbon nanotubes with defects," in *Proceedings of the ASME/JSME 2011, 8th Thermal engineering joint conference*, Honolulu, Hawaii, USA, 2011.

[9] C. W. Padgett and D. W. Brenner, "Influence of Chemisorption on the Thermal Conductivity of Single-Wall Carbon Nanotubes," *Nano Lett.*, vol. 4, p. 1051, 2004.

[10] H. Fan, K. Zhang and M. Yuen, "Effect of defects on thermal performance of carbon nanotube investigated by molecular dynamics simulation," in *International conference on electronic materials and packaging, EMAP.*, 2006.

[11] N. Mingo, D. A. Stewart, D. A. Broido and D. Srivastava, "Phonon transmission through defects in carbon nanotubes from first principles," *Phys. R. B,* vol. 77, p. 033418, 2008.

[12] G. Zhang and B. Li, "Thermal conductivity of nanotubes revisited: Effects of chirality, isotope impurity, tube length, and temperature," *J. Chem. Phys.* , vol. 123, p. 114714, 2005.

[13] I. Savic, N. Mingo and D. A. Stewart, "Phonon Transport in Isotope-Disordered Carbon and Boron-Nitride Nanotubes: is localization observable?," *Phys. Rev. Lett.,* vol. 101, p. 165502, 2008.

[14] J. Park, M. F. P. Bifano and V. Prakash, "Sensitivity of thermal conductivity of carbon nanotubes to defect concentrations and heat-treatment," *J. Appl. Phys.* , vol. 113, p. 034312, 2013.

[15] Y. Huang, J. Gao and R. Liu, "Structure and electronic properties of nitrogen-containing carbon nanotubes," *Synthentic Met.,* vol. 113, p. 251, 2000.

[16] R. Czerw, M. Terrones, J. C. Charlier, X. Blase, B. Foley, R. Kamalakaran, N. Grobert, H. Terrones, D. Tekleab, P. M. Ajayan, W. Blau, M. Ruhle and D. L. Carroll, "Identification of Electron Donor States in N-Doped Carbon Nanotubes," *Nano Lett.,* vol. 1, p. 457, 2001.

[17] S. H. Lim, H. I. Elim, X. Y. Gao, A. T. S. Wee, W. Ji, J. Y. Lee and J. Lin, "Electronic and optical properties of nitrogen-doped multiwall carbon nanotubes," *Phys. Rev. B,* vol. 73, p. 045402, 2006.

[18] Y. M. Choi, D. S. Lee, R. Czerw, P. W. Chiu, N. Grobert, M. Terrones, M. Reyes-Reyes, H. Terrones, J. C. Charlier, P. M. Ajayan , S. Roth, D. L. Carroll and Y. W. Park, "Nonlinear behavior in the thermopower of doped carbon nanotubes due to strong, localized states," *Nano Lett.,* vol. 3, p. 839, 2003.

[19] C. P. Ewels and M. Glerup, "Nitrogen doping in carbon nanotubes," *J. Nanosci. Nanotech.,* vol. 5, p. 1345, 2005.

[20] J. Guo, A. Javey, H. Dai, S. Datta and M. Lundstrom, "Predicted performance advantages of carbon nanotube transistors with doped nanotubes as source/drain," *arXiv:cond-mat/0309039,* 2003.

[21] M. A. Kuroda and J. P. Leburton, "High-field electrothermal transport in metallic carbon nanotubes," *Phys. Rev. B,* vol. 80, p. 165417, 2009.

[22] E. Pop, "Energy dissipation and transport in nanoscale devices," *Nano Res.,* vol.

3, p. 147, 2010.

[23] M. S. Dresselhaus and P. C. Eklund, "Phonons in carbon nanotubes," *Advances in Physics*, vol. 49, p. 705, 2000.

[24] J. Hone, "Phonons and thermal properties of carbon nanotubes," in *Carbon nanotubes, Topics in applied physics*, Berlin, Germany, Springer, 2001, pp. 273-286.

[25] W. Yi, L. Lu, D. L. Zhang, Z. W. Pan and S. S. Xie, "Linear specific heat of carbon nanotubes," *Phys. Rev. B,* vol. 59, p. R9015, 1999.

[26] F. Muller-Plathe, "A simple nonequilibrium molecular dynamics method for calculating the thermal conductivity," *J. Chem. Phys.*, vol. 106, p. 6082, 1997.

[27] D. J. Evans and G. P. Morris, Statistical mechanics of nonequilibrium liquids, New York: Academic, 1990.

[28] K. Aoki and D. Kusnezov, "Fermi-Pasta-Ulam β Model: boundary jumps, Fourier's Law, and scaling," *Phys. Rev. Lett.*, vol. 86, p. 4029, 2001.

[29] O. Narayan and S. Ramaswamy, "Anomalous Heat Conduction in One-Dimensional Momentum-Conserving Systems," *Phys. Rev. Lett.*, vol. 89, p. 200601, 2002.

[30] D. J. Evans, "Homogeneous NEMD algorithm for thermal conductivity—Application of non-canonical linear response theory," *Phys. Lett.* , vol. 91, p. 457, 1982.

[31] F. Zhang, D. J. Isbister and D. J. Evans, "Multiple nonequilibrium steady states for one-dimensional heat flow," *Phys. Rev. E,* vol. 64, p. 021102, 2001.

[32] J. P. Hansen and I. R. McDonald, Theory of simple liquids, London: Academic, 1986.

[33] G. Chen, Nanoscale energy transport and conversion - A parallel treatment of electrons, molecules, phonons, and photons, New York: Oxford University Press, 2005.

[34] M. P. Allen and D. J. Tildesley, Computer simulation of liquids, New York: Oxford University Press, 1989.

[35] N. Yahya, Carbon and oxide nanostructures, Synthesis, characterisation and applications, Springer, 2011.

[36] A. Kinaci, J. B. Haskins, C. Sevik and T. Cagin, "Thermal conductivity of BN-C nanostructures," *Phys. Rev. B,* vol. 86, p. 115410, 2012.

[37] D. W. Brenner, O. A. Shenderova, J. A. Harrison, S. J. Stuart, B. Ni and S. B. Sinnott, "A second-generation reactive empirical bond order (REBO) potential energy expression for hydrocarbons," *J. Phys. Condens. Matter,* vol. 14, p. 783,

2002.

[38] M. Grujicic, G. Cao and W. N. Roy, "Computational analysis of the lattice contribution to thermal conductivity of single-walled carbon nanotubes," *J. Mater. Sci.,* vol. 40, p. 1943, 2005.

[39] Y. Zhou, M. Cook and M. Karplus, "Protein motions at zero-total angular momentum: the importance of long-range correlations," *Biophys. J.,* vol. 79, p. 2902, 2000.

[40] J. Che, T. Cagin, W. Deng and W. A. Goddard, "Thermal conductivity of diamond and related materials from molecular dynamics simulations," *J. Chem. Phys.,* vol. 113, p. 6888, 2000.

[41] A. J. H. McGaughey and M. Kaviany, "Thermal conductivity decompositon and analysis using molecular dynamics simulaitons," *Int. J. Heat Mass Transfer,* vol. 47, p. 1783, 2004.

[42] S. G. Volz and G. Chen, "Molecular-dynamics simulation of thermal conductivity of silicon crystals," *Phys. Rev. B,* vol. 61, p. 2651, 2000.

[43] A. Guajardo-Cuellar, D. B. Go and M. Sen, "Evaluation of heat current formulations for equilibrium molecular dynamics calculations of thermal conductivity," *J. Chem. Phys.,* vol. 132, p. 104111, 2010.

[44] R. M. Moghadam, S. A. Hosseini and M. Salehi, "The influence of Stone–Thrower–Wales defect on vibrational characteristics of single-walled carbon nanotubes incorporating Timoshenko beam element," *Physica E,* vol. 62, p. 80, 2014.

[45] J. Dallaire, "Thermal conductivity of carbon nanotubes from equilibrium molecular dynamics simulations: sensitivity to modeling and simulation parameters," Laval University, Master Thesis, 2012.

[46] T. Belin and F. Epron, "Characterization methods of carbon nanotube: a review," *Mater. Sci. Eng. B,* vol. 119, p. 105, 2005.

[47] E. A. Jackson and A. D. Mistriotis, "Thermal conductivity of one- and two-dimensional lattices," *J. Phys.: Condens. Matter,* vol. 1223, p. 1, 1989.

[48] H. J. Burch, "Bioapplications of nitrogen-doped carbon nanotubes, PhD Thesis," University of oxford, Linacre college, 2006.

[49] E. Cruz-Silva, F. Lopez-Urias, E. Munoz-Sandoval, B. G. Sumpter, H. Terrones, J. C. Charlier, V. Meunier and M. Terrones, "Electronic transport and mechanical properties of phosphorus- and phosphorus-nitrogen-doped carbon nanotubes," *ACS Nano,* vol. 3, p. 1913, 2009.

[50] B. G. Sumpter, J. Huang, V. Meunier, J. M. Romo-Herrera, E. Cruz-Silva, H.

Terrones and M. Terrones, "Manipulating the structure and properties of carbon nanotubes using substitutional dopants," *Int. J. Quan. Chem.*, vol. 109, p. 97, 2009.

[51] M. D. Koretsky, Engineering and Chemical Thermodynamics, Wiley, 2004.

[52] N. Kondo, T. Yamamoto and K. Watanabe, "Molecular-dynamics simulatons of thermal transport in carbon nanotubes with structural defects," *e-J. Surf. Sci. Nanotech.*, vol. 4, p. 239, 2006.

[53] W. Li, Y. Feng, J. Peng and X. Zhang, "Effect of Stone-Wales defects on the thermal conductivity of carbon nanotubes," *J. Heat. Trans.*, vol. 134, p. 092401, 2012.

[54] J. R. Lukes and H. Zhong, "Thermal conductivity of single wall carbon nanotubes: a comparison of molecular dynamics simulation approches," in *Proceedings of the 13th international heat transfer conference.*, Sydney, Australia, 2006.

[55] S. Maruyama, "A molecular dynamics simulatoin of heat conduction in a carbon nanotube,"
http://www.photon.t.u-tokyo.ac.jp/~maruyama/papers/02/CNT_Turkey.pdf,
Tokyo, Japan, 2002.

[56] B. Li and J. Wang, "Intriguing heat conduction of a chain with transverse motions," *Phys. Rev. Lett.*, vol. 92, p. 074302, 2004.

[57] R. Meyer and D. Comtesse, "Vibrational density of states of silicon nanoparticles," *Phys. Rev. B*, vol. 83, p. 014301, 2011.

[58] C. Kittle, Introduction to solid state physics, New York: John Wiley and Sons, 1996.

Chapter 5

Phonon Dispersion of N-doped SWNT from Molecular Dynamics

5.0 Introduction

Using Green-Kubo or non-equilibrium direct methods, molecular dynamics simulation can predict thermal conductivity. System-level analyses, however, only give very limited information about phonon group velocity, lifetimes and other phonon properties which are needed to fully understand the microscopic dynamics of phonon relaxation. Among phonon properties calculation methods, while anharmonic lattice dynamics (ALD) calculations based on perturbation theory can be used to predict the mode properties of a crystal in vacuum, [1] [2] the method is only valid at low temperatures (less than one fourth of the Debye temperature, ~120–240K for SWNTs), [3] [4] where 3-phonon processes dominate. At higher temperatures, as the magnitude of atomic displacements grows and the influence of higher-order phonon scattering events become increasingly important, overestimation of phonon lifetimes will occur. [2] [5] In doped CNTs, phonons scatter via interactions with defects at surfaces, but their effects on phonon properties cannot be directly incorporated into a lattice dynamics calculation since the interactions are non-periodic in space.

Normal mode decomposition (NMD) is used to predict phonon lifetimes from fitting the time auto-correlation of normal mode coordinates with an exponential

decay. [6] NMD is impractical, however, for SWNTs because the unit cell has a large set of basis atoms (e.g., in a (13, 0) CNT, the unit cell has 52 basis atoms) NMD also cannot provide dispersion relations.

Chapter 5 proposes a computationally convenient method to predict phonon dispersion relations and lifetimes directly from the velocities and coordinates of the atoms using the dynamic structure factor. Our method, which extends formulations developed by others particularly for SWNT systems, [7] [8] [9] [10] includes the full temperature-dependent anharmonicity of the atomic interactions, can be applied to both crystal and disordered systems. We discuss its application to MD simulations of pristine, isotope doped, substitutional N-doped, and pyridine-like-N-doped SWNTs. We explain the main mechanisms of the reduced thermal conductivities of doped SWNTs by comparing the phonon properties obtained.

5.1 SWNT Phonon Modes

A SWNT can be thought of as an infinite strip that is cut from a graphene sheet and rolled up into a seamless cylinder. Its phonon modes therefore share many similarities with those of graphene. In fact, the zone-folding method is reasonably efficient for predicting the phonon dispersion relation of SWNTs from the phonon dispersion of a graphene sheet. [11]

The phonons modes can be categorized in four groups by similarity with the four types of atomic displacements in the phonons of graphene: in phase & in plane, in phase & out of plane, out of phase & in plane, and out of phase & out of plane. Example modes in these four categories and their corresponding peaks (not all modes have peaks) in the Raman spectrum [12] are shown in Fig. 5.1.Each tube has four acoustic phonons:

i) One in-phase & in-plane longitudinal (LA) mode,

ii) One in-phase & in-plane twist (TW) mode (shown in Fig. 5.1 (b)), and

iii) Two degenerate in-phase & out-of-plane transverse (TA) modes.

Among the optical phonons, the following Raman-active modes are the most intense:

iii) In-phase & out-of-plane mode, otherwise known as the radial breathing mode (RBM), which is unique to CNTs. Its long wavelength limit frequency has inverse dependence on nanotube diameter *d*, given by $\omega \sim 28\text{meV}\cdot\text{nm}/d$ [13]. It appears to at a low frequency in Raman spectrum (shown in in Fig. 4.1 (a)).

iv) Out-of-phase & in-plane modes, (e.g., the G-band modes), with peaks in the approximate range of 1550-1600cm^{-1} related to the tangential vibrations of C atoms (shown in in Fig. 4.1 (d)).

We limit our phonon dispersion analysis to the low frequency region where the phonon modes are concentrated.

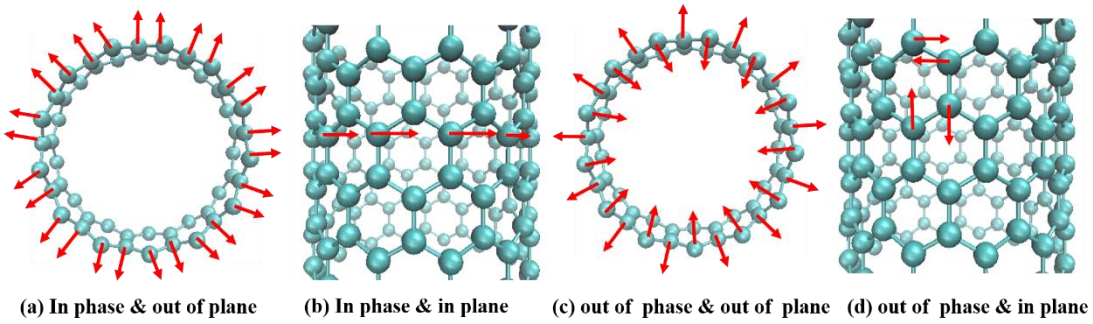

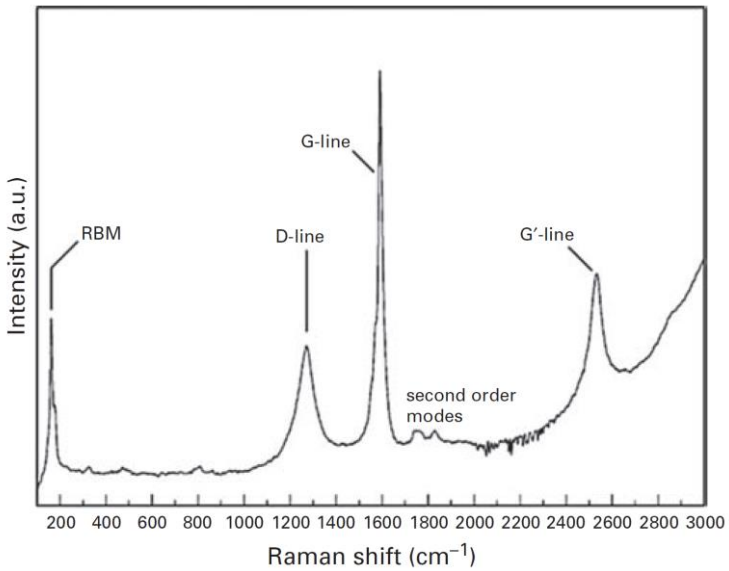

Figure 5.1 Top: Typical atomic displacements associated with mode vibrations. (a) RBM, (b) Twist (TW) mode, (c) RO (radial optical) mode, and (d) G band mode, corresponding to the G-line in the Raman spectrum. Bottom [12]: Raman spectrum obtained from SWNT sample with diameter of approximately 1.07nm, showing most characteristic features of CNTs.

5.2 Dynamic Structure Factor

Neutron scattering is frequently used to measure phonon dispersion relations in crystals and amorphous materials. [14] [15] The change in neutron momentum is the negative of the change in total phonon crystal momentum, to within an additive reciprocal lattice vector. Among all possible types of scattering, one-phonon scattering can be distinguished from background (zero-phonon scattering, multi-phonon scattering). In the one-phonon process, the neutrons absorb or emit precisely one phonon within the detecting object. The change of neutron energy and momentum

follows [14]

$$\frac{p'^2}{2M_n} = \frac{p^2}{2M_n} \pm \hbar\omega_k\left(\frac{\boldsymbol{p}'-\boldsymbol{p}}{\hbar}\right), \tag{5.2.1}$$

where $\boldsymbol{p}$ and $\boldsymbol{p}'$ are the initial and final neutron momenta, respectively, M_n is the neutron mass, and ω_k is given by the phonon dispersion relation.

Neutrons are only scattered at a few discrete energies $E' = p'^2/2M_n$. Points in an object's phonon spectrum are determined from $\boldsymbol{p} - \boldsymbol{p}'$ and $E' - E$. For perfect harmonic crystals, the one-phonon peak is perfectly sharp. In real materials, however, the peaks broaden since the harmonic stationary state decays with time due to anharmonic effects, and the peak width is associated with the phonon lifetime τ. [14]

For given projectile neutrons, the scattering cross section $d\sigma/(d\Omega dE)$, which quantifies the intrinsic rate that scattered neutrons can be detected at a certain angle, is related to the transition probability P, [14]

$$j\frac{d\sigma}{d\Omega dE} = \frac{PUM_n p'}{(2\pi\hbar)^3}, \tag{5.2.2}$$

where j is the incident neutron flux, Ω is the angular span of the detector, and U is the neutron-atom interaction. P can be further calculated from time-dependent perturbation theory, [16] and Eq. (5.2.2) becomes

$$\begin{aligned}\frac{d\sigma}{d\Omega dE} &= \frac{p'}{p}\frac{Na^2}{\hbar}S(\boldsymbol{q},\omega)\\ S(\boldsymbol{q},\omega) &= \frac{1}{N}\sum_{j,k=1}^{N}\exp\left[-i\boldsymbol{q}\cdot\left(\boldsymbol{R}_i-\boldsymbol{R}_j\right)\right]\int\frac{dt}{2\pi}\exp(i\omega t)\left\langle\exp\left[i\boldsymbol{q}\cdot\left(\boldsymbol{u}_i-\boldsymbol{u}_j(t)\right)\right]\right\rangle\end{aligned} \tag{5.2.3}$$

where $S(\boldsymbol{q}, \omega)$ is the dynamic structure factor, $\boldsymbol{q}$ is the wave vector, ω is the frequency, N is the total number of atoms, $\boldsymbol{R}_j$ is the equilibrium positon of atom j, $\boldsymbol{u}_j$ is the displacement of atom j from its equilibrium position, and the brackets < > denote the ensemble average. For a given $\boldsymbol{q}$, as a function of energy, S shows a series of spikes at

phonon energy, and the phonon dispersion curves appear as ridges on the contour map of S(***q***, w). Furthermore, Eq. (5.2.3) even without exploiting the harmonic approximation therefore can be applied to general material systems and temperature ranges. [14]

S can be presented in different forms, depending on the simulation method used. Moving the relative position term in Eq. (5.2.3) into the bracket yields the most well-known expression for *S*, as the spectrum of intermediate scattering function *F*(***q***, t), where ***r*** = ***R*** + ***u*** is the atom coordinate

$$\begin{aligned} S(\boldsymbol{q},\omega) &= \frac{1}{\pi}\int_0^{\infty} F(\boldsymbol{q},t)\exp(i\omega t)\,dt \\ F(\boldsymbol{q},t) &= \frac{1}{N}\sum_{j,k=1}^{N}\left\langle \exp\left[-i\boldsymbol{q}\cdot(\boldsymbol{r}_i-\boldsymbol{r}_j)\right]\right\rangle \end{aligned} \tag{5.2.4}$$

The time-dependent microscopic density is defined by weighting number w_j =1 to get the particle density, and $w_j = m_j/\langle m\rangle$ to get the normalized mass density

$$\rho(\boldsymbol{r},t) = \sum_{j=1}^{N} w_j \delta\left(\boldsymbol{r}-\boldsymbol{r}_j(t)\right) \tag{5.2.5}$$

F can be determined from the autocorrelation of density Fourier components $\rho_{\mathbf{q}}$

$$\begin{aligned} F(q,t) &= \frac{1}{N}\left\langle \rho_{\boldsymbol{q}}(t)\rho_{-\boldsymbol{q}}\right\rangle \\ \rho_{\boldsymbol{q}}(t) &= \sum_{j=1}^{N} w_j \exp\left(i\boldsymbol{q}\boldsymbol{r}_j(t)\right) \end{aligned} \tag{5.2.6}$$

The nature of the weighting number obtains either the number-based or mass-based dynamic structure factors, which should be similar for a 1D chain. [17] Since *F* only contains the ensemble information over all possible polarizations and suffers from slow decay, it is ill-suited for Fourier transformation. [7] Therefore, we modify the method by defining the density current associated with Eq. (5.2.6) as

$$\boldsymbol{J}\left(\boldsymbol{r},t\right)=\sum_{j=1}^{N}\boldsymbol{v}_j\left(t\right)w_j\delta\left(\boldsymbol{r}-\boldsymbol{r}_j\left(t\right)\right) \tag{5.2.7}$$

where $\boldsymbol{v}_j$ is the velocity of atom *j*. Applying Fourier transform on continuity equation, the corresponding equation for the Fourier components of $\boldsymbol{J}$ is

$$\frac{\partial\rho_{\boldsymbol{q}}\left(t\right)}{\partial t}+i\boldsymbol{q}\cdot\boldsymbol{J}_{\boldsymbol{q}}\left(t\right)=0 \tag{5.2.8}$$

with the general property of autocorrelation $d^2<A(t)A^*>/dt^2 = -<\dot{A}(t)\dot{A}^*>$, Eq. (5.2.8) implies

$$C\left(\boldsymbol{q},t\right)=\frac{q^2}{N}\left\langle J_{\boldsymbol{q}}\left(t\right)J_{-\boldsymbol{q}}\right\rangle=-\frac{\mathrm{d}^2}{\mathrm{d}t^2}F_{\hat{\boldsymbol{v}}}\left(\boldsymbol{q},t\right) \tag{5.2.9}$$

where $F_{\hat{\boldsymbol{v}}}$ is the projection of *F* on $\boldsymbol{v}$ direction. Written in terms of Laplace transform and taking the real part, Eq. (5.2.9) becomes

$$C\left(\boldsymbol{q},\omega\right)=\omega^2S_{\hat{\boldsymbol{v}}}\left(\boldsymbol{q},t\right) \tag{5.2.10}$$

Since $\boldsymbol{J}_{\mathbf{q}}$ is a vector, *C* is a second-rank tensor. The independent components of *C* (or *S*) representing different phonon polarizations are obtained by decomposing the velocity in a proper orthonormal coordinate system, where each coordinate is given by the polarization vector of normal modes, e.g., for isotropic materials, there are only two independent components S_{L} (longitudinal) and S_{T} (transverse), and $\boldsymbol{v}$ is decomposed as $\boldsymbol{v}\cdot\boldsymbol{q}$ and $\boldsymbol{v}-\boldsymbol{v}\cdot\boldsymbol{q}$. [8]

Therefore, the phonon dispersion curve can be separately calculated by mapping the dynamic structure factor projected along the phonon polarization (S_α) in $\boldsymbol{q}$ space. Combining the separately taken phonon branches into one contour map leads to the overall phonon dispersion

$$S_\alpha(q,\omega)=\frac{q^2}{\pi\omega^2 N}\int_0^\infty dt\left\langle\left[\sum_{j=1}^{N}v_{\alpha,k}(t)\,w_j\exp\left(i\boldsymbol{q}\cdot\boldsymbol{r}_j(t)\right)\right]\cdot\left[\sum_{j=1}^{N}v_{\alpha,j}\,w_j\exp\left(-i\boldsymbol{q}\cdot\boldsymbol{r}_j\right)\right]\right\rangle\exp(i\omega t). \tag{5.2.11}$$

5.3 Allowed Wavevectors of SWNT and Subbands

Here, we explain how to evaluate and use the expression above to predict the phonon dispersion curves of SWNTs. By definition, we have to calculate S (or S_α) from allowed wavevectors (see Eq. (5.2.3)). Note that prohibited wavevectors would render exceptional low S value between the allowed wavevectors and would break the correct ridges of the contour map of S. For isotropic materials, we determine the wavevectors by $n\cdot 2\pi/L$, where L is the linear size of the simulation box, n is a natural number, and the maximum number cannot be larger than $2\pi/a$, where a is lattice constant. The process is somewhat complicated in anisotropic systems like SWNT.

The lattice vectors and reciprocal lattice vectors for the zigzag (n, 0) SWNTs we use are shown in Fig. 5.2, and summarized in Table 5.1.

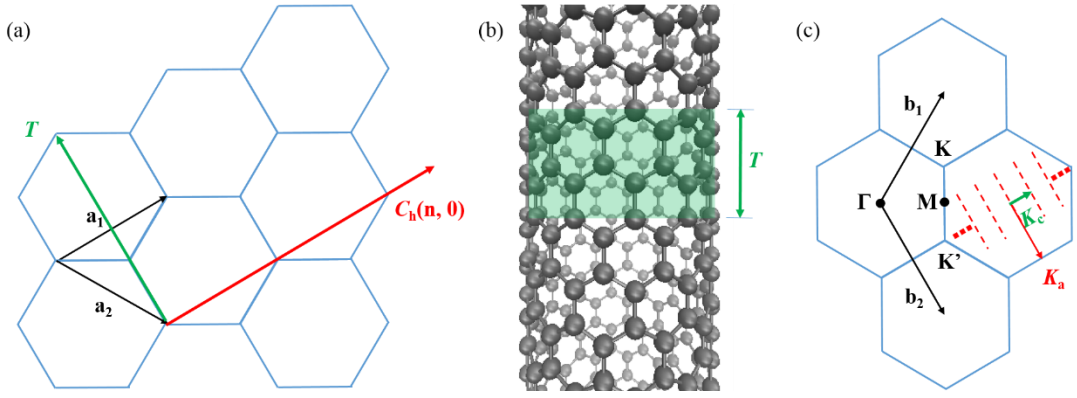

Figure 5.2 (a) Zigzag SWNT is wrapped from graphene according to chiral vector $\boldsymbol{C}_h$, and translation vector $\boldsymbol{T}$ gives the tube axis direction. (b) Unit cell of a zigzag SWNT is the highlighted cylinder. (c) Reciprocal lattice, axial vector $\boldsymbol{K}_a$, and circumferential vector $\boldsymbol{K}_c$, of the zigzag SWNT with the high-symmetry points illustrated.

Table 5.1 Parameters and associated equations for zigzag (n, 0) SWNT.[1]

Symbol	Name	Expression
$\boldsymbol{a}_1$, $\boldsymbol{a}_2$	primitive lattice vectors	$\boldsymbol{a}_1 = [\sqrt{3}a/2, a/2]$, $\boldsymbol{a}_2 = [\sqrt{3}a/2, -a/2]$
$\boldsymbol{C}_h$	chiral vector	n $\boldsymbol{a}_1$
C_h	length of $\boldsymbol{C}_h$	an
$\boldsymbol{T}$	translation vector	$\boldsymbol{a}_1 - 2\boldsymbol{a}_2$
T	length of $\boldsymbol{T}$	$\sqrt{3}a$
N_h	number of hexagons/cell	2n
$\boldsymbol{b}_1$, $\boldsymbol{b}_2$	basis of reciprocal lattice	$\boldsymbol{b}_1 = [2\pi/\sqrt{3}a, 2\pi/a]$, $\boldsymbol{b}_2 = [2\pi/\sqrt{3}a, -2\pi/a]$
$\boldsymbol{K}_a$	axial lattice vector	$-\boldsymbol{b}_2/2$
K_a	length of K_a	2π/T
$\boldsymbol{K}_c$	circumferential lattice vector	$(2\boldsymbol{b}_1+\boldsymbol{b}_2)/2$
K_c	length of K_c	$2\pi/C_h$

[1] a is the Bravais lattice constant, $a = \sqrt{3}a_{C\text{-}C} = 2.46$Å, and $a_{C\text{-}C}$ is the carbon-carbon bond length ($\sim$1.42 Å).

We consider a finite length nanotube with N_{uc} unit cells and obtain the allowed wavevectors q_a along the axial direction from periodic boundary conditions on Bloch wave functions:

$$\psi(0) = \psi(N_{uc}T) = e^{iq_a N_{uc} T}\psi(0) \quad \Rightarrow \quad e^{iq_a N_{uc} T} = 1, \tag{5.3.1}$$

which yields the set of wavevectors

$$q_a = \frac{2\pi}{N_{uc}T} l, \quad l = 0,1\ldots N_{uc} - 1, \tag{5.3.2}$$

where the maximum integer value of l is determined from the requirement that unique solutions for k are restricted to the first Brillouin zone. Applying the same period conditions to determine the allowed wavevectors q_c along the circumferential direction yields

$$\psi(0)=\psi(C_h)=e^{iq_cC_h}\psi(0) \quad \Rightarrow \quad e^{iq_cC_h}=1$$
$$q_c=\frac{2\pi}{C_h}\beta, \quad \beta=0,1\ldots N_h-1 \qquad , \tag{5.3.3}$$

$\boldsymbol{q}=\boldsymbol{q}_a+\boldsymbol{q}_c$ give the allowed wavevectors.. The Brillouin zone of SWNT consists of N_h lines representing 1D bands as shown in Fig. 5.2 (c). Each line gives a phonon subband indexed with azimuthal quantum number β.

To calculate the $\exp(i\boldsymbol{q}\cdot\boldsymbol{r}(t))$ in Eq. (5.2.11), we need to transform the global Cartesian coordinate system used in MD simulation to a local cylindrical coordinate system to get the correct dot production between the circumferential wavevector and the atom trajectory, reproducing the value in an unfolded 2D graphene plane. The transform method is shown in Fig. 5.3.

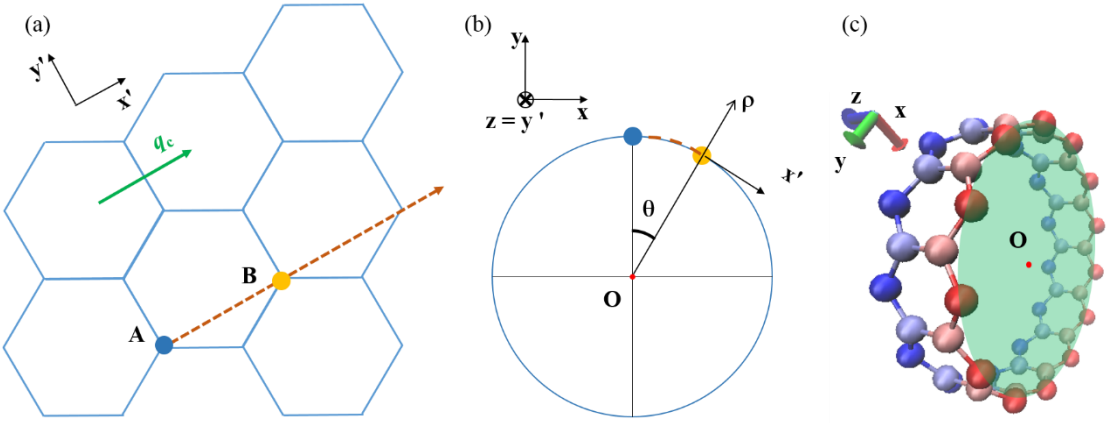

Figure 5.3 (a) 2D x′y′ coordinate system in 2D graphene plane. A and B represent two C atoms along the chiral vector. (b) A and B in local cylindrical coordinate system Ozρθ and in global Cartesian coordinate system xyz. (c) Defining the equilibrium coordinate of the center (point O) from a C-atom ring; atoms in one ring are the same color.

Since tube axis ($\mathbf{y}'$ in 2D coordinates, and $\mathbf{z}$ in Cartesian coordinates) is invariant during the transform, we easily obtain $\boldsymbol{q}_a\cdot\boldsymbol{r}_j$ as q_az_j. In 2D graphene coordinates, when we choose the equilibrium position of a reference atom (A) as the origin point, $q_cx'_j$ gives $\boldsymbol{q}_c\cdot\boldsymbol{r}_j$. After folding the graphene sheet to CNT, x'_j becomes the arc length from

the reference point, $\rho\theta$, where ρ is the radial length from the center of the ring (point *O*) to the atom and θ is the azimuth angle. The position of point *O* is space-time dependent, since CNT would vibrate slowly (~0.005THz, shown in Fig 5.4) during simulation, as noted in [18].

Figure 5.4 Two consecutive snapshots of a 21nm (13, 0) SWNT showing similar configurations. (a) At 8ps (b) At 200ps.

Next, we evaluate the position of *O* points along the tube axis by averaging (x, y) of all the atoms in the C-atom rings. Each unit cell has 4 *O* points as shown in Fig. 5.3 (c). For pristine and substitutional doped (n, 0) SWNT, the atom number in one ring (n_R) equals to n; for pyridine-like doped SWNT, the atom number has to be counted individually for each ring based on the original configuration. Normally, the ring surface does not locate exactly in the x-y plane, but instead has a small titling angle ϕ which is caused by displacement in the *z* direction as shown in Fig. 5.5. Under small-angle approximation, we estimate (Eq. (5.3.4)), the calculation error of $\rho\theta$ from surface tilting), and find that it is less than 2% in all cases.

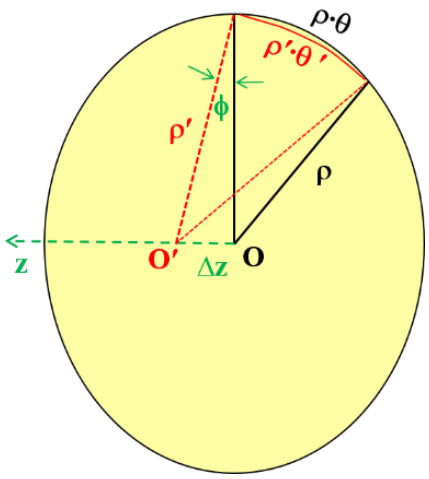

Figure 5.5 C-atom ring locates in $O'\rho'\theta'$ surface; its projection on x-y plane $O\rho\theta$ is used in calculation.

$$\Delta(\rho\theta)=\sqrt{x_{\mathrm{R}}^2+y_{\mathrm{R}}^2+\Delta z^2}\left(\tan^{-1}\frac{x_{\mathrm{R}}}{y_{\mathrm{R}}\sqrt{1+\cos^{-2}\phi}}+\varphi\right)-\sqrt{x_{\mathrm{R}}^2+y_{\mathrm{R}}^2}\left(\tan^{-1}\frac{x_{\mathrm{R}}}{y_{\mathrm{R}}}+\varphi\right)$$

$$\phi=\frac{\sqrt{x_{\mathrm{R}}^2+y_{\mathrm{R}}^2}}{x_{\mathrm{R}}^2+y_{\mathrm{R}}^2+\Delta z^2}$$

$$\varphi=\begin{cases}0 & x_{\mathrm{R}},y_{\mathrm{R}}>0\\ \pi & x_{\mathrm{R}}<0\\ 2\pi & x_{\mathrm{R}}>0,y_{\mathrm{R}}<0\end{cases} \qquad (5.3.4)$$

$$x_{\mathrm{R}}=x-\frac{1}{n_{\mathrm{R}}}\sum_i x_i \quad y_{\mathrm{R}}=y-\frac{1}{n_{\mathrm{R}}}\sum_i y_i$$

Therefore, the dot production between the allowed wavevectors in subband β are given by

$$\boldsymbol{q}\cdot\boldsymbol{r}=z\frac{2\pi}{N_{uc}T}l+\frac{2\pi}{C_{\mathrm{h}}}\beta\rho\theta,\quad l=0,1\ldots N_{uc}-1$$

$$\theta=\tan^{-1}\frac{x_{\mathrm{R}}}{y_{\mathrm{R}}}+\varphi \qquad (5.3.5)$$

$$\rho=\sqrt{x_{\mathrm{R}}^2+y_{\mathrm{R}}^2}$$

we also transform the atom velocities into a cylindrical coordinate system in order to predict the projected dynamic structure factor and obtain the phonon branches along the z direction (longitudinal mode), along ρ direction (RBM and part of transverse mode), and along the x′ direction (twisting mode and part of transverse mode)

$$\begin{pmatrix} v_\rho \\ v_{x'} \\ v_z \end{pmatrix} = \begin{bmatrix} \cos\theta & \sin\theta & 0 \\ -\sin\theta & \cos\theta & 0 \\ 0 & 0 & 1 \end{bmatrix} \begin{pmatrix} v_x \\ v_y \\ v_z \end{pmatrix} \tag{5.3.6}$$

combining Eq. (5.2.11), Eq. (5.3.5), and Eq. (5.3.6), yields the projected dynamic structure factor S_α for the different subbands of zigzag SWNT, where α represents $z/\rho/x'$ polarizations. Note that we can extend the same scheme (transform between 2D and 3D global/local coordinate systems) to other nanotube structures (SWNTs or BN nanotubes); the only difference is we need to change the allowed wavevectors according to the tube structures.

$$\begin{aligned} S_{\beta\alpha}\left(l\frac{K_a}{N_{\text{uc}}},\omega\right) &= \frac{q^2}{\pi\omega^2 N}\int_0^\infty \mathrm{d}t \left\langle \Theta_{\beta\alpha}\left(l\frac{K_a}{N_{\text{uc}}},t\right)\Theta_{\beta\alpha}\left(-l\frac{K_a}{N_{\text{uc}}}\right)\right\rangle \exp(i\omega t) \\ \Theta_{\beta\alpha}\left(l\frac{K_a}{N_{\text{uc}}},t\right) &= \sum_{j=1}^{N} v_{\alpha,j}(t)\, w_j \exp\left[i z_j(t) l\frac{K_a}{N_{\text{uc}}} + K_c \beta \rho_j(t)\theta_j(t)\right] \end{aligned} \tag{5.2.11}$$

5.4 Simulation Approach and Results of $S_\alpha(q, \omega)$

We use the LAMMPS package to perform our MD simulations and to output the atomic trajectories and velocities. All simulations use the same temperature, inter-atomic potential, boundary conditions, and time step scheme as the thermal conductivity calculations. The process is as follows.

We use 21nm long (containing 50 unit cells) (13, 0) SWNT/isotope-doped SWNT/N-doped SWNTs to derive dynamic structure factors, and give a resolution of wave-number axis of $0.02K_a$. Similar to the 1D chain where the phonon dispersion curve is symmetric at $q = \pi/a$, the phonon dispersion of CNT is symmetric at $q = K_a/2 = T/\pi$. Therefore, the dispersion curve of CNT are normally restricted to $[0, T/\pi]$. [19] [20] After normalizing it to [0, 1] through qT/π, our simulation gives a resolution of 0.04 along the first Brillouin zone.

The sampling rate needs to be high enough to capture the maximum frequency in the system (larger than the Nyquist frequency). Based on the PDOS calculation described in Chap. 4, the highest phonon frequency of SWNT is around 50THz and so the corresponding Nyquist limit is 100THz. We use an interval of 8fs (125THz) to dump the atomic trajectory file, which is the same interval used in spectral energy density (SED) analysis of CNT on silica substrate. [21] We also test an interval of 2fs for the pristine SWNT and validate that 8fs gives the correct results.

The temperature in all equilibrium MD simulations is 300K. We perform a potential energy minimization routine [22]followed by 20ps of time integration with NVE to get well-equilibrated simulation structures. Then, we bring each structure up to our target temperature by running an NVT ensemble using a minimum of 200ps with a Nose-Hoover style thermostat to maintain the temperature. After that, we run an NVE ensemble using a minimum of 200ps with a velocity Verlet scheme to allow the system to reach equilibrium. We run one last 200ps NVE ensemble and use its data for our final calculation. Note that the record time has to be long enough to cover the longest phonon lifetime, which is approximately 100ps. [21] [23] [24] Chap. 5.5 explains the equivalence between SED analysis and our dynamic structure factor analysis, but for now we note that the record time for SED analysis of similar CNT length varies from 130ps to 1ns. [21] [23] Testing a series of record time (100ps, 200ps, 300ps, and 400ps) for the 0^{th} subband of pristine SWNT case reveals no noticeable change beyond 200ps. Hence, we use a record time of 200ps, which gives the resolution of the frequency axis as~ 0.008THz.

To compare our simulation scheme to other methods, we calculate the 0^{th} subband of a 21nm (16, 0) SWNT and plot it with the literature value using 4 nearest neighbors force-constant (4NN) methods [20] as shown in Fig. 5.6.

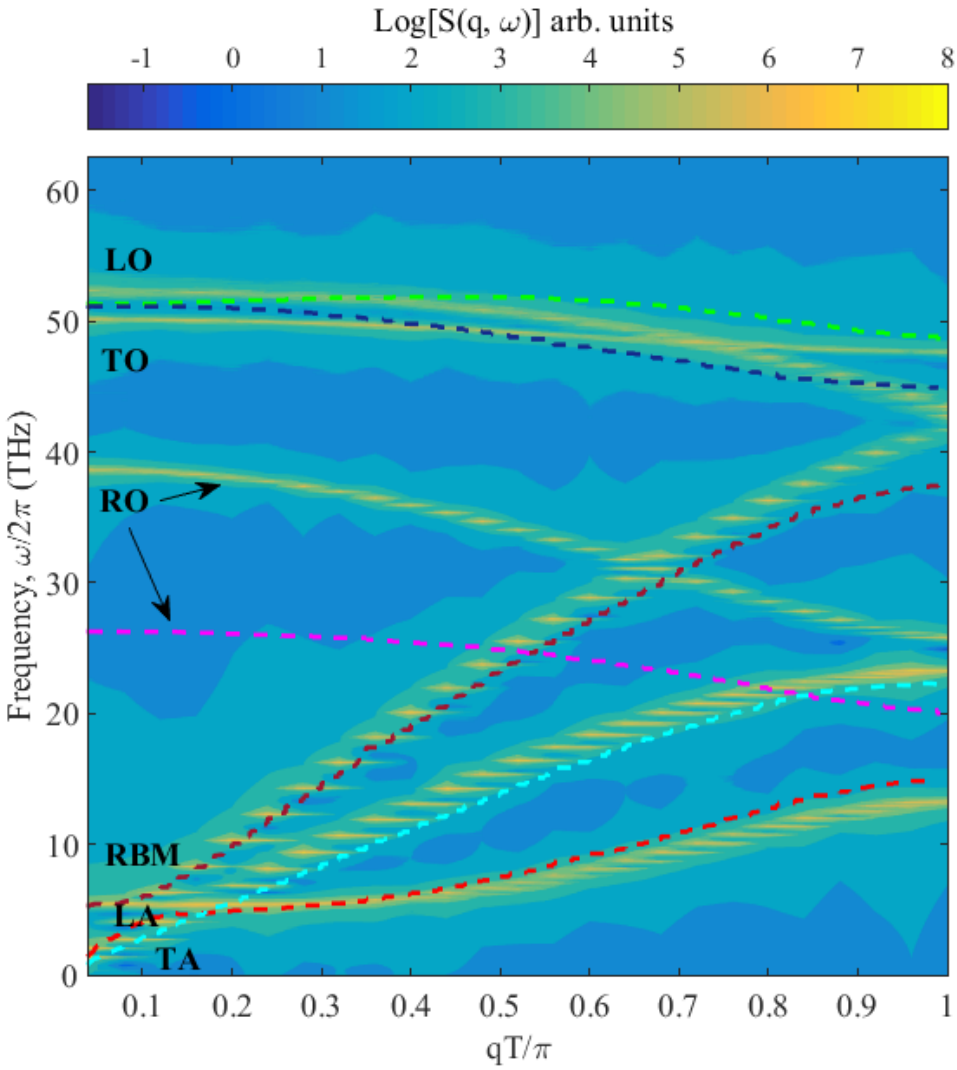

Figure 5.6 Phonon dispersion of (16, 0) CNT calculated from dynamic structure factor (contour map) at 300K and from 4NN model [20] (dashed lines).*Phonon branches in [20] were labeled incorrectly and they are corrected in this plot.

The phonon dispersions of the longitudinal, transverse, and RBM modes from two methods are similar whereas the RO mode shows a major divergence. The 4NN method heavily relies on the empirical force constant inputs which generate the dynamic matrix. The fact that different parametrizations give fairly different dispersions at high frequency region (> 10THz) [19] may explain the inconsistency here.

We plot the projected and total dynamic structure factors of the first two subbands

of pristine (13, 0) SWNT as shown in Fig. 5.7 and obtain the fitted dispersion curves by capturing the peaks of the contour map.

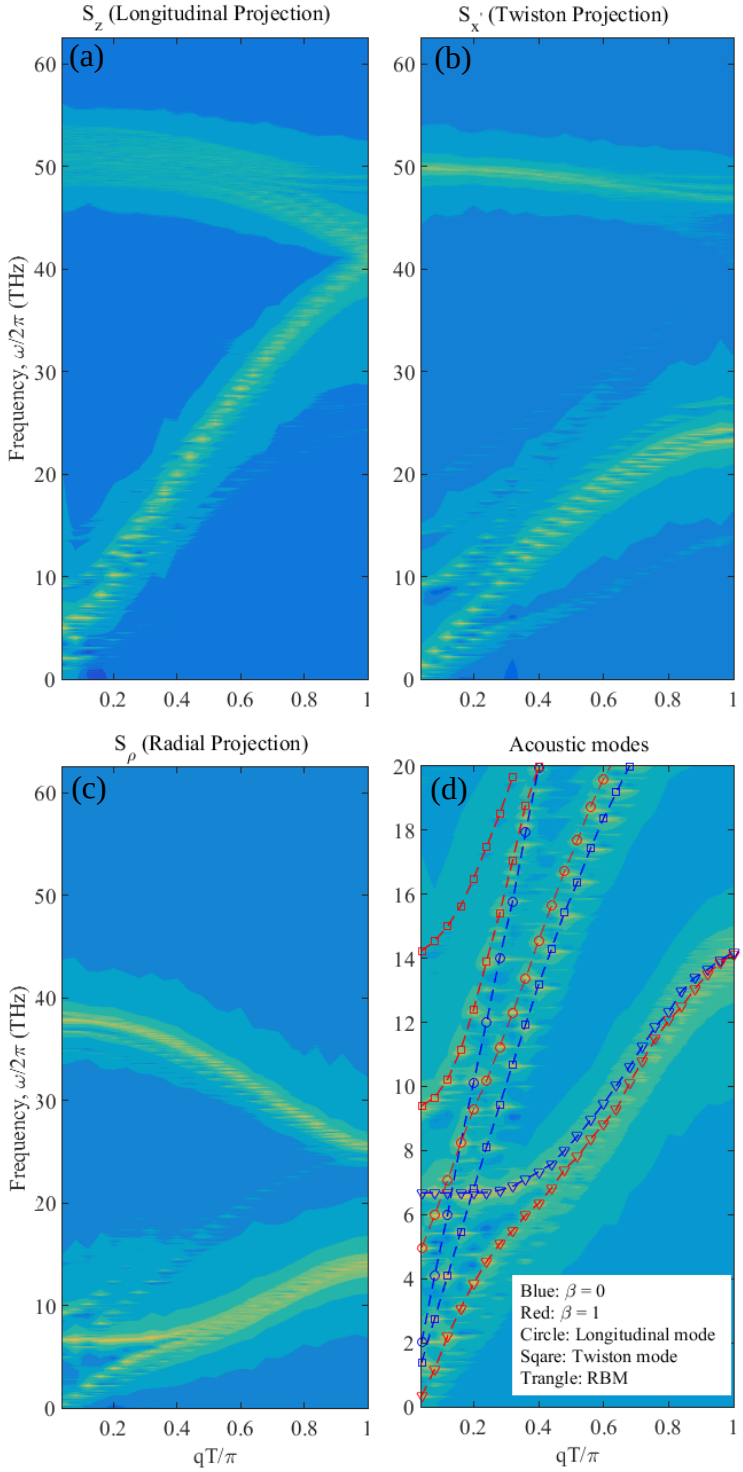

Figure 5.7 Dynamic structure factor of the first two subbands of (13, 0) CNT at 300K. (a-c) projected *S*. (d) total *S* and the dispersion curves of the acoustic modes.

Note that at Γ point (q = 0), all of the phonon branches have pure polarization:

Longitudinal mode – S_z, Twiston mode – $S_{x'}$, and RBM mode – S_ρ. Thus, we conclude that the the branch assignment is meaningful. The eigenvectors of each phonon mode are mixed, however, when we move away from Γ point. For instance, the RBM mode soon has eigenvectors with x′ polarization. The results suggest that we could process the projected dynamic structure factor to get the partial, but crucial, information of phonon eigenvectors, which is needed in order to calculate the electron phonon coupling [25] without the eigenvalue problem of dynamical matrix.

The results of the number-based and mass-based dynamic structure factors are similar as shown in Fig 5.8. The minima value of the number-based dynamic structure factor, however, is smaller, yet the shape and linewidth of the phonon branches show no significant difference, probably because the mass ratio between the C and N atoms is close to 1 and the maximum doping concentration is still fairly small. Therefore, we use the mass-based dynamic structure factors in our analysis.

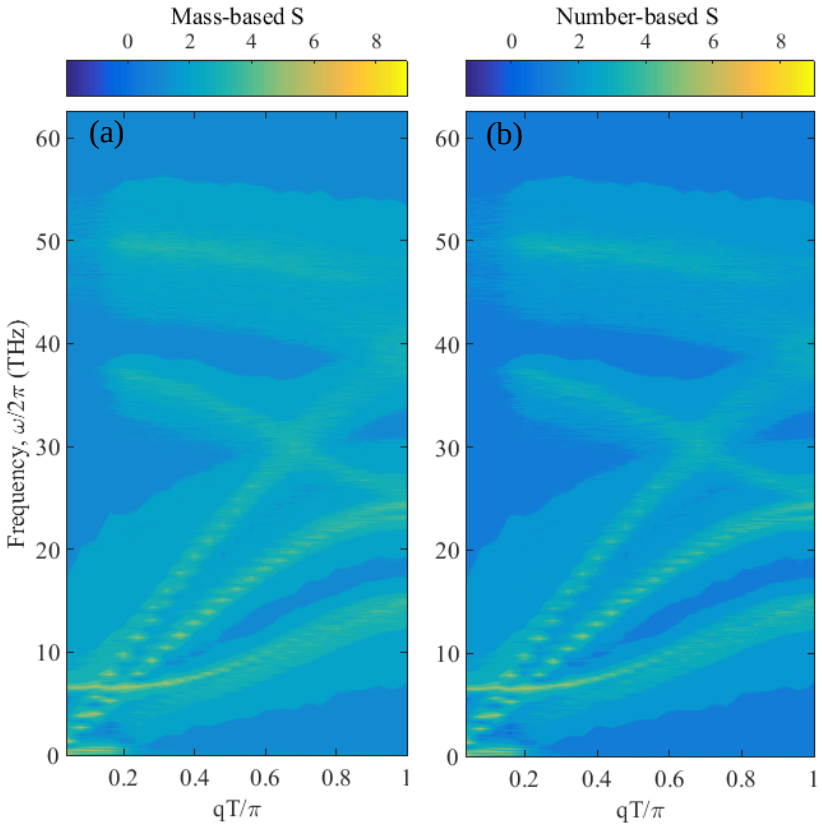

Figure 5.8 Dynamic structure factor of 5% substitutional N-doped (13, 0) CNT for the first subband at 300K. (a) Mass-based. (b) Number-based.

We plot the first two subbands of pristine, 5% substitutional isotope doped, 5% substitutional N-doped, and 5% pyridine-like N-doped (13, 0) SWNT as shown in Fig. 5.9.

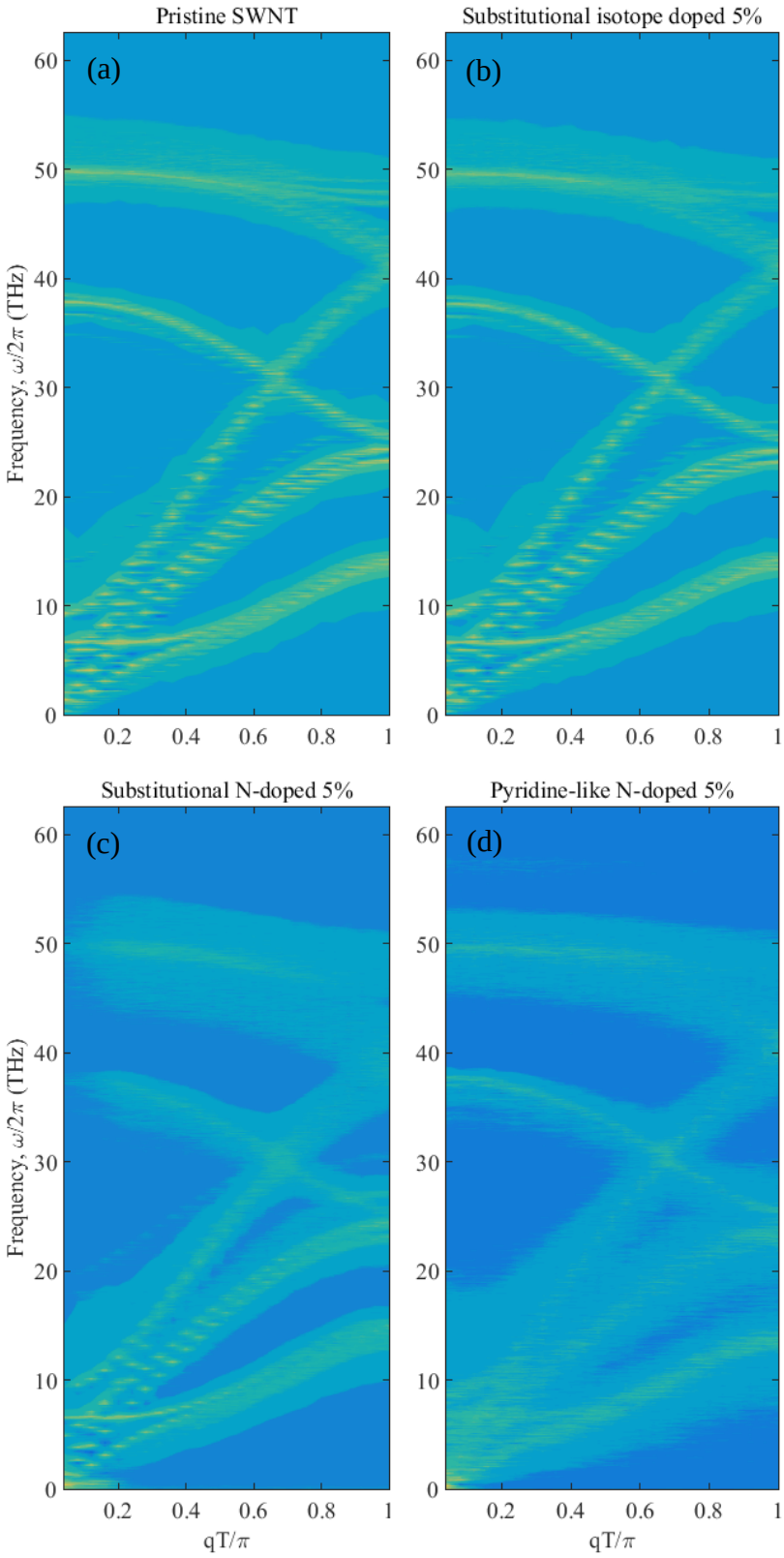

Figure 5.9 Dynamic structure factor of pristine and doped (13, 0) CNTs for the first two subbands at 300K. (a) Pristine. (b) 5% substitutional isotope doped. (c) 5% substitutional N-doped. (d) 5% pyridine-like N doped.

The roughly similar shape of the dispersion curves suggests that doping does not significantly reduce the phonon velocity. With the same doping concentration, the frequency of main peaks and the linewidth are almost preserved in isotope doped SWNT; the linewidth increases in substitutional N-doped SWNT, especially in high frequency ranges; and the dispersion branches are further diffused beyond recognition in pyridine-like N-doped SWNT. Compared to substitutional doped modes, the acoustic modes are greatly broadened. Larger linewidths indicate a shortened phonon lifetime. The results, which are consistent with the thermal conductivity simulations, suggest that the reduced thermal conductivity is mostly due to the shortened phonon lifetime. Comparing the substitutional isotope to N-doped SWNT shows that the mass difference brought by doping does not create strong scattering. Phonon scattering is mostly due to the defect potential caused by different atom types.

5.5 Phonon Lifetime

Although dynamic structure factor can give additional information about phonon lifetimes, [26] spectral energy density (SED) analysis is the most frequently used method to calculate CNT phonon lifetime. [21] [23] [24] Here, we discuss the equivalent between the dynamic structure factor method and SED under the harmonic approximation.

For a wide-sense-stationary random process $x(t)$, the Wiener-Khinchine theorem states that the absolute square of the Fourier transform is equal to the Fourier transform of the autocorrelation $R_x(\tau)$ [27]

$$\begin{aligned} S_x(\omega) &= \int_{-\infty}^{\infty} R_x(\tau)\exp(i\omega\tau)\mathrm{d}\tau = \lim_{T\to\infty}\frac{1}{T}\left|X_T(\omega)\right|^2 \\ X_T(\omega) &= \int_{-T}^{T} x(t)\exp(i\omega\tau)\mathrm{d}t \end{aligned} \quad . \tag{5.5.1}$$

The un-normalized mass-based structure dynamic factor given by Eq. (5.2.11) can be rewritten as

$$\Phi = \frac{\omega^2}{q^2} S(q,\omega) = \frac{1}{\pi NT} \left| \int_0^T \mathrm{d}t \sum_\alpha \sum_{j=1}^N v_{\alpha,k}(t) m_j \exp\left[i\left(\boldsymbol{q} \cdot \boldsymbol{r}_j(t) - \omega t \right) \right] \right|^2 . \tag{5.5.2}$$

note that Eq. (5.5.2) is similar to the definition of spectral energy density in [9] [10], where C is some constant

$$\Phi = \frac{C}{T} \left| \int_0^T \mathrm{d}t \sum_{j=1}^N v_k(t) \sqrt{m_j} \exp\left[i\left(\boldsymbol{q} \cdot \boldsymbol{r}_j(t) - \omega t \right) \right] \right|^2 , \tag{5.5.3}$$

and similar to the definition in [21], where *B* is the atom number inside unit cell

$$\Phi(q,\omega) = \frac{1}{4\pi NT} \sum_\alpha \sum_b^B m_b \left| \int_0^T \mathrm{d}t v_{\alpha,k}(t) \exp\left[i\left(\boldsymbol{q} \cdot \boldsymbol{r}_j(t) - \omega t \right) \right] \right|^2 . \tag{5.5.4}$$

the difference between Eq. (5.5.2) and Eq. (5.5.3) is that the exponent power of mass is one in Eq. (5.5.3). Since number-based and mass-based dynamic structure factors are similar in our cases, Eq. (5.5.2) and Eq. (5.5.3) should render similar results. In addition to the power of mass, the summation over α and *j* occurs outside the square modulus for Eq. (5.5.4) whereas the summation over α can be moved inside the square modulus since polarizations are orthonormal to each other. Therefore, we use the un-normalized square root of the mass-based dynamic structure (equals to Eq. (5.5.3)) in our phonon lifetime analysis. The steps are as follows.

In the phonon lifetime approximation, Φ is a sum of damped harmonic oscillators. For a harmonic oscillator which is damped by a stochastic friction, the dynamic structure factor can be shown to be [28]

$$S(\omega) = \frac{\hbar}{\pi M_0} \frac{1}{1 - \exp\left(-\hbar\omega / k_\mathrm{B} T\right)} \frac{\Gamma}{\left(\omega^2 - \omega\omega_0\right)^2 + \left(\gamma\omega\right)^2} , \tag{5.5.5}$$

where M_0 is the particle mass, ω_0 is the frequency of the undamped oscillator, Γ is the friction constant, and $1/2\gamma$ is the lifetime. In the classical limit $\hbar \rightarrow 0$, this result reduces to

$$S(\omega) = \frac{1}{\pi M_0 k_B T} \frac{\Gamma}{\left(\omega^2 - \omega\omega_0\right)^2 + \left(\gamma\omega\right)^2}. \tag{5.5.6}$$

Therefore, we fit the shape of Φ at the available wavevectors using the Lorentzian function, where I is the peak magnitude and γ is the half-width at half-maximum

$$\Phi(q,\omega) = \frac{I}{\left(\omega - \omega_0\right)^2 + \gamma^2}. \tag{5.5.7}$$

The acoustic branches are mostly below 15THz as shown in Fig. 5.8 (d). Φ of the first three subbands and the fitting parameter to the damped harmonic oscillator model along qT/π = 0.04, 0.4, 0.8 for frequencies below 15 THz are shown in Fig. 5.10−5.12. Similar peak-and-valley profiles exit along the entire frequency axis at each allowed wavevector.

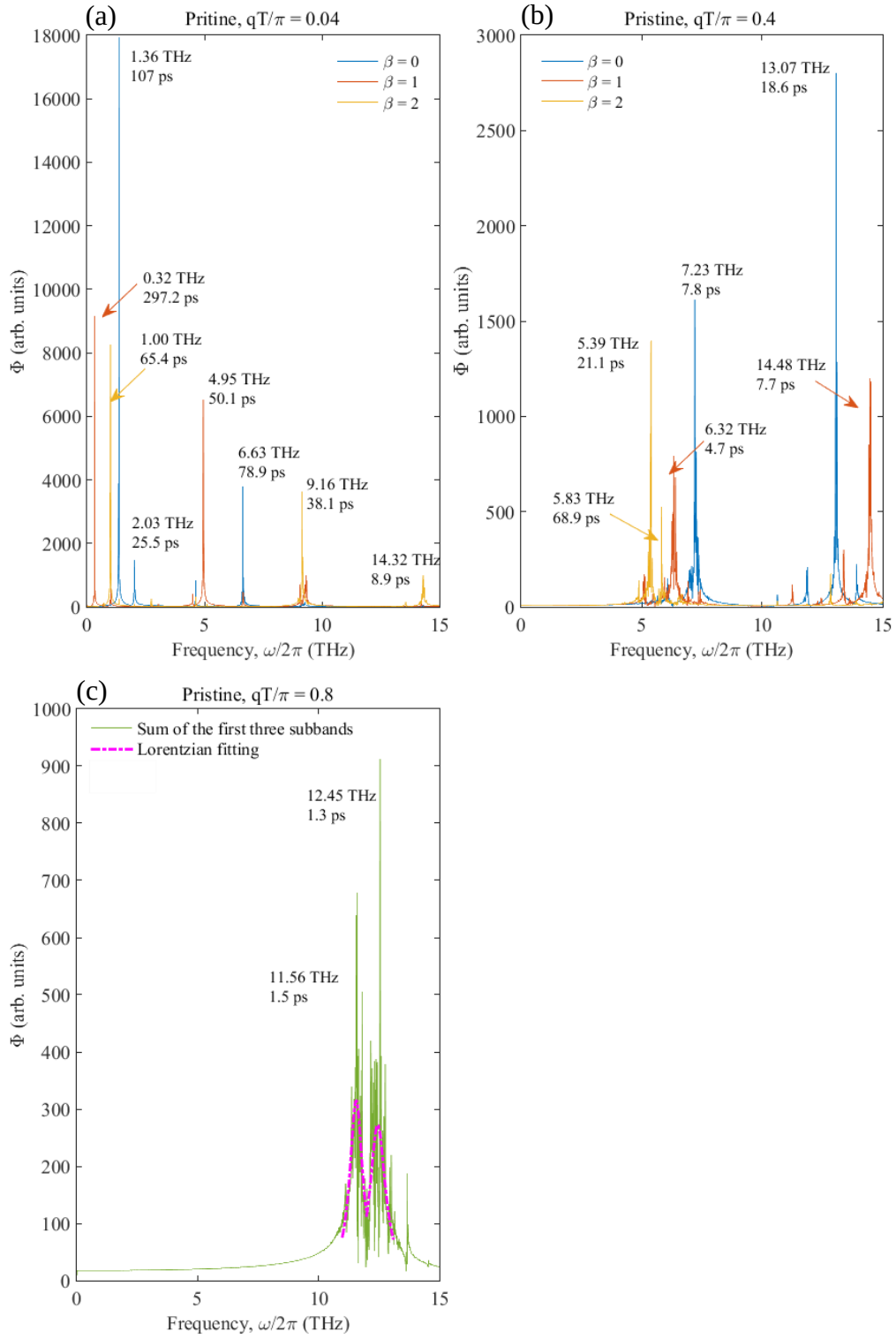

Figure 5.10 Un-normalized $\sqrt{m}$ based dynamic structure factor of pristine (13, 0) CNT for frequencies below 15 THz at 300K. The lifetime of each mode is determined by fitting each peak to Eq. (5.5.7). (a) Along qT/π = 0.04. (b) Along qT/π = 0.4. (c) Along qT/π = 0.8.

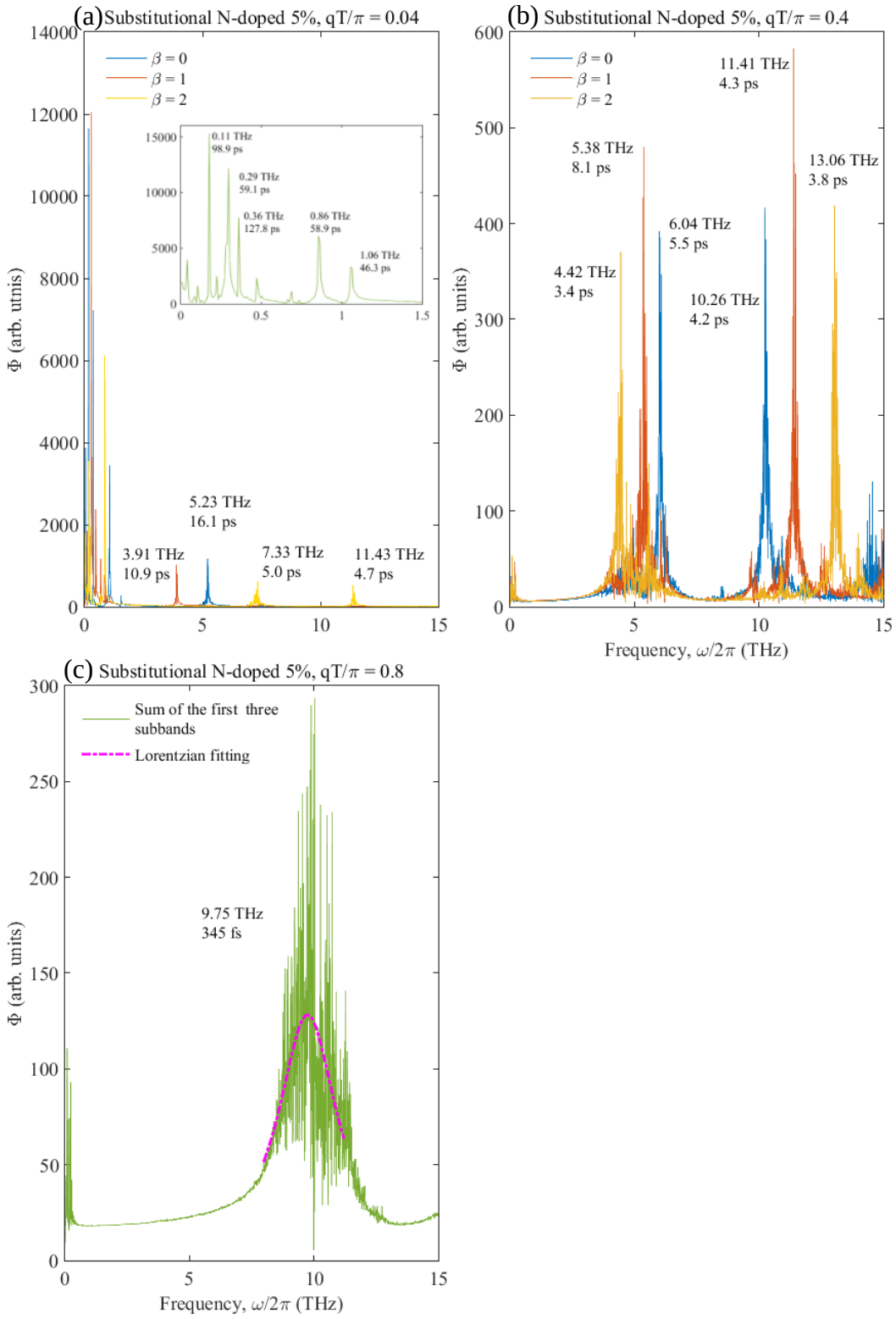

Figure 5.11 Un-normalized $\sqrt{m}$ based dynamic structure factor of 5% substitutional N-doped (13, 0) CNT for frequencies below 15 THz at 300K. The lifetime of each mode is determined by fitting each peak to Eq. (5.5.7). (a) Along qT/π = 0.04. Low frequency region is enlarged in the inset. (b) Along qT/π = 0.4. (c) Along qT/π = 0.8.

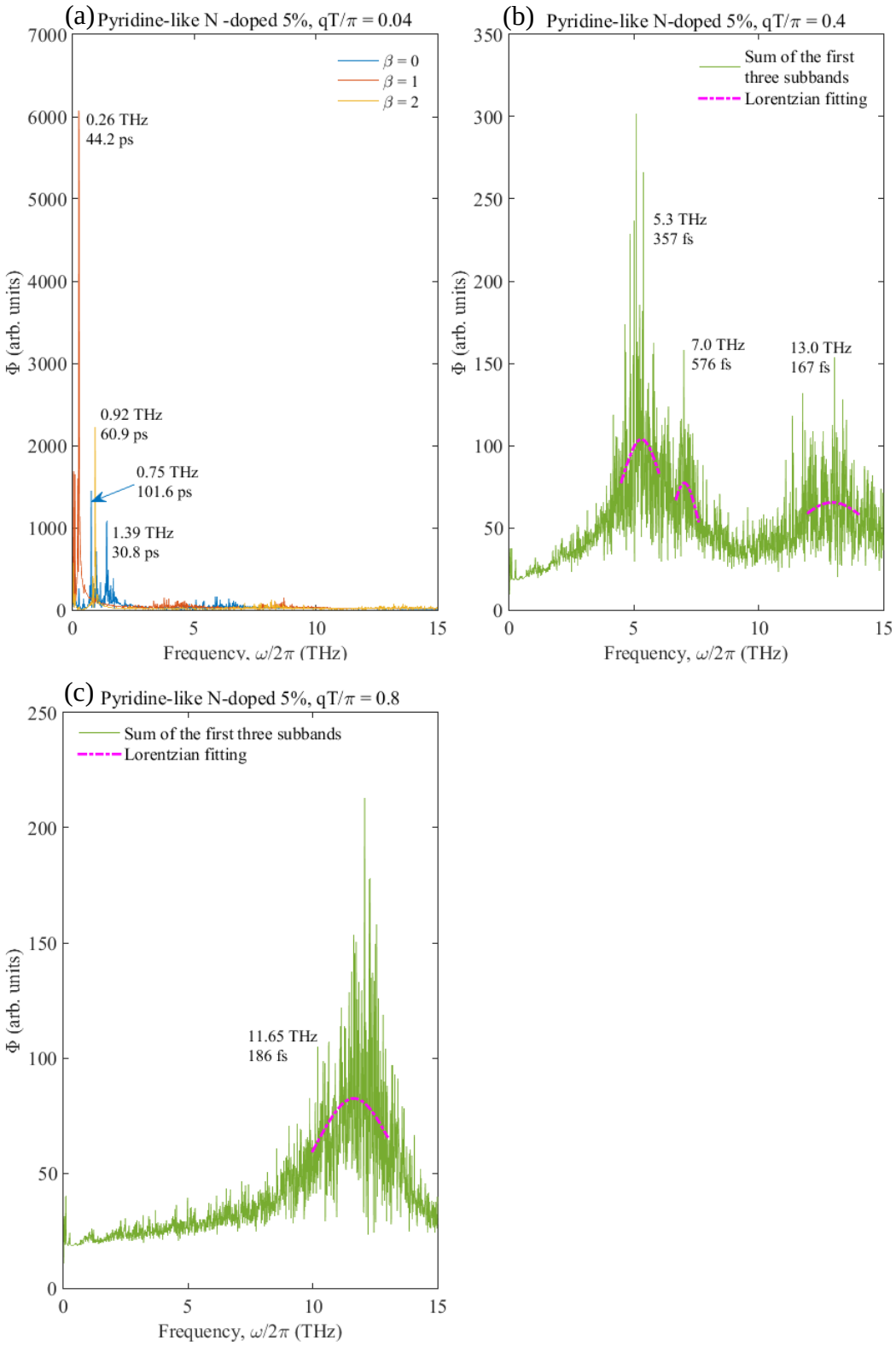

Figure 5.12 Un-normalized $\sqrt{m}$ based dynamic structure factor of 5% pyridine-like N-doped (13, 0) CNT for frequencies below 15 THz at 300K. The lifetime of each mode is determined by fitting each peak to Eq. (5.5.7). (a) Along qT/π = 0.04. (b) Along qT/π = 0.4. (c) Along qT/π = 0.8.

While insignificant in contour maps of dynamic structure factors, the spectrum along certain wavevector shows a clear redshift around the Γ point for substitutional N-doped CNT. The frequency of LA mode in the first subband near point (qT/π = 0.04) decreases from 1.36 THz in pristine CNT to 0.29 THz in substitutional N-doped CNT, but stays almost the same as 1.39 THz in pyridine-like N-doped CNT. Moreover, even a low level of substitutional N dopants has been shown to significantly reduce the local mechanical strength (along the tube axis). [29] [30] Based on the redshift at qT/π = 0.4, the longitudinal phonon velocity reduces about 16% from the pristine value results of 5% substitutional N-doping. Compared to a 4.1% reduction for 0.5% substitutional N-doping concentration [29] and a 30% reduction for C_3N_4 tubes, [31] we conclude that our reduction is reasonable. To explain the lack of redshift in pyridine-like N-doped CNTs, we note that the fracturing of pristine CNTs starts with creating pentagons and Sone-Wales defects to release strain whereas the substitutional N-doped CNTs starts with a C-N bond breaking process. [30] In pyridine-like N-doped CNT, the pentagon defects accompany the N- doping site intrinsically, so it is possible that these pentagon defects react as a strain releaser to maintain the tube strength.

Note that the lifetime magnitude is 10~100ps for the phonon modes near the Γ point, 1~10ps for modes around the zone center, and 0.1~1ps for modes near the zone edge. Compared to the average phonon-phonon scattering time of 21.2ps (20nm long pristine SWNT) obtained in Chap. 4, we conclude that phonon modes all across the Brillion zone involve in heat transfer with the low frequency modes contributing the most. Indeed, the lifetime of most modes decreases 2- 4 times from that of pristine CNT for substitutional N-doped CNT. The lifetime of most modes near the Γ point decrease 3-6 times for pyridine-like N-doped CNT, 10-50 times for modes near the zone center, and 8 times for modes near the zone edge, together with greatly reduced

available phonon modes. The results are consistent with the thermal conductivity and PDOS calculation discussed in Chap. 4.

5.6 Summary

A computationally efficient procedure for extracting phonon dispersion relations and the lifetimes of pristine and doped SWNTs directly from atomic trajectories and velocities was proposed. The calculation time scaled with atom number N the NMD scaled with N^2, and the ALD scaled with N^4. The polarization of each mode was obtained from projecting the dynamic structure factors. The predicted phonon dispersion relations agreed with those obtained using ALD. The predicted lifetimes explained the thermal conductivities in the equilibrium MD simulations that the greatly shortened phonon lifetimes were the chief cause of the reduced thermal conductivity in N-doped CNTs. The introduced N-C interaction breaking the structure symmetry of CNT caused much stronger scattering than that of isotope defects.

[1] A. Debernardi, S. Baroni and E. Molinari, "Anharmonic phonon lifetimes in semiconductors from density-functional perturbation theory," *Phys. Rev. Lett*, vol. 75, p. 1819, 1995.

[2] J. E. Turney, E. S. Landry, A. J. H. McGaughey and C. H. Amon, "Predicting phonon properties and thermal conductivity from anharmonic lattice dynamics calculations and molecular dynamics simulations," *Phy. Rev. B*, vol. 79, p. 064301, 2009.

[3] J. R. Lukes and H. Zhong, "Thermal conductivity of individual single-wall carbon nanotubes," *J. Heat. Trans.*, vol. 129, p. 705, 2007.

[4] J. Hone, "Phonons and thermal properties of carbon nanotubes," in *Carbon nanotubes, Topics in applied physics*, Berlin, Germany, Springer, 2001, pp. 273-286.

[5] G. P. Srivastava, "Lattice thermal conduction mechanisms in solids," in *High thermal conductivity materials*, Boca Raton, Springer, 2006, pp. 1-33.

[6] A. J. H. McGaughey and M. Kaviany, "Quantitative validation of the Boltzmann

transport equation phonon thermal conductivity model under the single-mode relaxation time approximation," *Phys. Rev. B,* vol. 69, p. 094303, 2004.

[7] M. Schoen, R. Vogelsang and C. Hoheisel, "Computation and analysis of the dynamic structure factor $S(k, \omega)$ for samll wave vectors: A molecular dynamic study for a Lennard-Jones liquid," *Mol. Phys.,* vol. 57, p. 445, 1986.

[8] H. Shintani and H. Tanaka, "Universal link between the boson peak and transverse phonons in glass," *Nat. mater. ,* vol. 7, p. 870, 2008.

[9] N. D. Koker, "Thermal conductivity of MgO periclase from equilibrium first principles melecular dynamics," *Phys. Rev. Lett.,* vol. 103, p. 125902, 2009.

[10] C. Z. Wang, C. T. Chan and K. M. Ho, "Tight-binding molecular-dynamics study of phonon anharmonic effects in silicon and diamond," *Phys. Rev. B,* vol. 42, p. 11276, 1990.

[11] R. A. Jishi, L. Venkataraman, M. S. Dresselhaus and G. Dresselhaus, "Phonon modes in carbon nanotubes," *Chem. Phys. Lett.,* vol. 209, p. 77, 1993.

[12] T. Belin and F. Epron, "Characterization methods of carbon nanotube: a review," *Mater. Sci. Eng. B,* vol. 119, p. 105, 2005.

[13] M. Cardona and R. Merlin, Light scattering in solids IX, (Topics in applied physics vol.108), Springer, 2007.

[14] N. W. Ashcroft and N. D. Mermin, Solid State Physics, Sauders College Publishing, 1976.

[15] A. B. Bhatia and R. N. Singh, "Phonon dispersion in metallic galsses: a smiple model," *Phys. Rev. B,* vol. 31, p. 4751, 1984.

[16] D. Park, Introduction to the quantum theory, McGraw-Hill, 1964.

[17] K. Helbig, W. Just, G. Radons and H. Yang, "Dynamic strucure factors and Lyapunov modes in disordered chains," *Phys. Rev. B,* vol. 82, p. 026206, 2010.

[18] X. Zhang, M. Hu and D. Poulikakos, "A low-freqency wave motion mechanism enables efficient energy transport in carbon nanotubes at high heat fluxes," *Nano Lett.,* vol. 12, p. 3410, 2012.

[19] J. Zimmermann, P. Pavone and G. Cuniberti, "Vibrational modes and low-temperature thermal properties of graphene and carbon nanotubes: Minimal force-constant model," *Phys. Rev. B,* vol. 78, p. 045410, 2008.

[20] S. O. Koswatta, S. Hasan, M. S. Lundstrom, M. P. Anantram and D. E. Nikonov, "Nonequilibrium Geen's function treatment of phonon scattering in carbon-nanotube transistors," *{IEEE} Trans. Electron Devices ,* vol. 54, p. 2339, 2007.

[21] Z. Y. Ong, E. Pop and J. Shiomi, "Reduction of phonon lifetimes and thermal

conductivity of a carbon nanotube on amorphous silica," *Phys. Rev. B,* vol. 84, p. 165418, 2011.

[22] S. Plimpton, "Fast Parallel Algorithms for Short-Range Molecular Dynamics," vol. 117, p. 1, 1995.

[23] J. A. Thomas, J. E. Turney, R. M. Iutzi, C. H. Amon and J. H. McGaughey, "Predicting phonon dispersion relations and lifetimes from spectral energy density," *Phys. Rev. B,* vol. 81, p. 081411, 2010.

[24] L. Zhu and B. Li, "Low thermal conductivity in ultrathin carbon nanotube (2, 1)," *Sci. Rep,* vol. 4, p. 4917, 2014.

[25] S. Hasan, Electron phonon interaction in carbon nanotube devices, PhD thesis, Purdue University, 2007.

[26] R. Meyer and P. Entel, "Martensite-austenite transition and phonon dispersion curves of Fe1-xNix studied by molecular-dynamics simulations," *Phys. Rev. B,* vol. 57, p. 5140, 1998.

[27] D. Chelidze, "The power spectral density and the autocorrelation," 2011. [Online]. Available: http://personal.egr.uri.edu/chelidz/courses/mce567/handouts/psdtheory.pdf.

[28] B. L. Lovesey, Theory of neutron scattering from condensed matter, Clarendon Press, 1984.

[29] E. Cruz-Silva, F. Lopez-Urias, E. Munoz-sandoval, B. G. Sumpter, H. Terrones, J. C. Charlier, V. Meunier and M. Terrones, "Electronic Transport and Mechanical properties of phosphorus- and phosphorus-nitrogen-doped carbon nanotubes," *ACS. Nano.,* vol. 3, p. 1913, 2009.

[30] B. G. Sumpter, J. Huang, V. Meunier, J. M. Romo-Herrera, E. Cruz-Silva, H. Terrones and M. Terrones, "A theoretical and experimental study on manipulating the structure and properties of carbon nanotubes using substitutional dopants," *Int. J. Quant. Chem.,* vol. 109, p. 97, 2009.

[31] E. Hernandez, C. Goze, P. Bernier and A. Rubio, "Elasitic properties of single-wall nanotubes," *Appl. Phys. A. Mater Sci. Process.,* vol. 68, p. 287, 1999.

Chapter 6

Conclusion and Future work

6.0 Conclusion

In this work the following has been done:

The full thermoelectric properties (thermal conductivity, electrical conductivity and Seebeck coefficient) of long-period HgCdTe (MCT) superlattices (SLs) are measured from 100K to 300K. Phonon dispersion curves of MCT SL are calculated using Rytov's elastic continuum model. It has been shown that phonon group velocity in long-period MCT SLs is greatly reduced due to Brillouin zone folding effect. This explains measured thermal conductivity which is lower than the alloy limit even the impedance from layer interfaces is small due to a low interface density. Diffusive phonons become important to thermal transport since the contribution from propagating phonon is reduced as phonon group velocity decreased. The specific heat of MCT SLs is almost temperature independent, therefore the diffusive thermal conductance is also temperature independent. This explains the measured thermal conductivity is nearly constant in a wide temperature range.

The full thermoelectric properties are measured for ultralow density SWNT networks that are either pristine or coated by graphene (Gr), BN, or PEDOT:PSS. The large mesh size of these networks eliminates the collective effects (e.g., phonon interference) found in dense SWNT networks, thus allowed the transport properties of

junctions to be distinguished from those of the nanotubes for the first time. Gr-/BN-coatings, which improves network's mechanical properties, degrades its thermal and electrical performances, as the junction impedances become outweighed by the increased impedances of the coated SWCNTs themselves. The Gr-coating further leads to a plateau in the network thermal conductivity over a range of temperatures, and is explained with a temperature-dependent phonon mean free path model.

The effects of nitrogen dopants on SWNT thermal properties are investigated in detail. Tube thermal conductivity and phonon density of states are simulated with various doping type, concentration, and tube length by molecular dynamics. A dyanmic structure factor based method is further developed to calculate the phonon dispersion and lifetime of doped SWNTs. Even a small amounts of substitional/pyridine-like-N dpoant can effectively reduce the thermal conductivity by shorten the phonon life time. In the other hand, substitutional-N-doping could increase the electrical conductivity of SWNTs. Therefore substitutional-N-doping provides an interesting way in improving *ZT* in CNT systems.

6.1 Future work

The thermal conductivity value reported for long-period MCT SLs, which is comparable to that of short-period MCT SLs at room temperature, suggests possible improvement of *ZT* in MCT SLs through optimization of doping concentration and electron energy filtering in long-period (wide-barrier) SLs. In such SLs, the lowest subband lies mainly below the barrier potential while the higher subbands lie above it, and up to four subbands contribute to Seebeck voltage. [1] In short-barrier MCT SL, however, the lowest conduction subband extends well above the barrier, and influence

from higher subbands is negligible, indicating that the effect of energy filtering is small. [1] Therefore it may be possible to reach higher Seebeck coefficients in long-period MCT SLs than short-period ones with optimal doping, without elevating thermal conductivity. Investigating the effect of doping and well width on *ZT* of MCT SL could be one avenue for extending the current work.

BN-coated SWNT aerogels exhibiting much better TE properties (reduced thermal conductivity, enhanced electrical conductivity and Seebeck coefficient) than pristine/Gr-coated aerogels with similar network mesh-size, suggest a new way to improve *ZT* of CNT networks through carefully designed coating/doping modifications. In contrast to other methods which only improve one or two parameters of *ZT*, coating/doping modifications could improve all three parameters simultaneously by tuning both the coating properties and the CNT backbone properties. Coatings with high Seebeck coefficient as well as both *n*- and *p*- type dopants could be explored. The greatly reduced thermal conductivity of N-doped SWNTs indicated by our simulations suggests there is plenty of room for doped CNTs in TE applications; also, this brings attention to a potential heat dissipation problem in FETs and other electronic devices fabricated using N-doped CNTs. The calculation method developed for CNTs using a projected phonon dispersion curve and phonon lifetime could be easily extended to CNTs with defects. In the long term it should be possible to integrate them with BTE (Boltzmann transport equation) based simulation of electron transport in order to predict and optimize the performance of doped-CNT based nano-electronic devices.

[1] R. J. Radtke, H. Ehrenreich and C. H. Grein, "Multilayer thermoelectric referigeration in $Hg_{1-x}Cd_xTe$ superlattices," *J. Appl. Phys.*, vol. 86, p. 3195, 1999.